TRACKING AND QUANTIFYING NANOPARTICLE CONTRAST AGENTS USING MAGNETIC RESONANCE IMAGING

A Dissertation

Presented to the Faculty of the Graduate School

of Cornell University

in Partial Fulfillment of the Requirements for the Degree of

Doctor of Philosophy

by

Richard Wong

August 2012

ABSTRACT

TRACKING AND QUANTIFYING NANOPARTICLE

CONTRAST AGENTS USING MAGNETIC RESONANCE IMAGING

Richard Wong, Ph.D.

Cornell University 2012

MRI is a powerful technique that is commonly used in clinical settings. It is non-invasive, does not employ ionizing radiation, and is capable of high spatial and temporal resolution, making it ideal for a wide variety of imaging applications, both for active diagnostic applications and preventative medicine. The strategies described in this thesis further increase the diagnostic ability of MRI by selectively delivering contrast enhancing nanoparticles to areas of interest, either through changes in cellular, organ, and systemic behavior as a result of disease states, or through biospecificity conferred by surface-bound targeting ligands. In doing so, this allows MRI to accurately probe systemic processes or cellular targets previously not available as diagnostic indicators, and has the potential to dramatically expand the spectrum of biological characteristics that can be visualized and quantified using MRI. The work in this study represents a step towards the creation of specialized, use-specific diagnostic agents that have the potential to improve the accuracy and speed of clinical diagnoses.

BIOGRAPHICAL SKETCH

Richard Wong was born in Tacoma, Washington in 1983. He received the Bachelor of Science degree in Electrical Engineering from the University of Florida in 2006. He joined the graduate program in Biomedical Engineering at Cornell University in 2006, and in 2010 he received the Masters of Science degree in Biomedical Engineering.

[T]he end of the line. All trains finish there. They don't go on anywhere.

-*The Sun Also Rises,* Ernest Hemmingway

ACKNOWLEDGEMENTS

Though only my name is listed on the cover, the work described in this dissertation represents the collaborative efforts of many individuals, and I am deeply thankful for their contributions.

I would like to thank my advisor Yi Wang for his insight and immeasurable patience. This dissertation would not be possible without his support.

I am equally grateful to my advisor Moonsoo Jin for his unmatched enthusiasm and dedication. His tireless support has made this dissertation possible, and his efforts have helped me develop into a more dedicated researcher and a more disciplined individual.

I would also like to acknowledge several scientists from Altor Bioscience, in particular Jack Egan, Bai Lui, Xiaoyun Zhu, Lijing You, Ling Kong, Kai-Ping Han, Hyung-il Lee, Pierre-Andrew Chavaillaz, and Peter Rhode, for their very significant contributions to my work.

I would like to thank Jennifer Weiser, whose dedication to puns in the face of adversity is admirable. I would be lost without her.

Many thanks go to Tian Liu, a great colleague and an even greater friend. My gratitude for his immerse support in and out of the lab cannot be properly expressed in words.

Special thanks also go to Xiaoyue Chen for her tireless work during our research collaborations. Research is a cooperative endeavor and her contributions have greatly supported and improved the work of my own.

I would be remiss if I did not acknowledge my colleagues in the Wang Lab at the Weill Medical College, the Jin Lab at Cornell University, and Altor Bioscience, of which my work represents only a small fraction of a larger group effort.

I would also like to recognize the members of my special committee, Moonsoo Jin, Yi Wang, and Peter Doerschuk for their careful consideration during the examination of this dissertation.

Finally, I would like to thank my parents for their infinite patience, unconditional love, and unending wisdom.

TABLE OF CONTENTS

LIST OF FIGURES

LIST OF TABLES

INTRODUCTION

MR imaging uses powerful magnetic and radio frequency fields to align, alter, and observe the nuclear magnetization of hydrogen atoms in the water of the body. Due to the varying nature of these magnetic properties across the spectrum of tissue and other material found in the body, it becomes possible to generate images by exploiting this differential. Contrast in the resulting images reflects this difference and provide a relative measure by which tissue types can be distinguished.

To further increase the contrast between tissue types, various types of contrast agents may be used to alter the magnetism in a localized area. Materials such as paramagnetic gadolinium-containing (Gd) liposomes (1, 2) or micelles (3-5), and superparamagnetic iron oxide (SPIO) nanoparticles (6, 7) can be used to alter the magnetic properties of the surrounding water. Used in conjunction with strategies to localize these contrast agents in specific areas of interest and imaging sequences designed to fully maximize the differences induced by these contrast agents, contrast agents can be used as probes to selectively highlight structures and phenomena indicative of a variety of biological conditions. In particular, SPIO nanoparticles have become established for use in liver imaging (8), lymph node characterization (9), diagnosis of tissue inflammation (10, 11), and stem cell labeling (12-16).

This dissertation explores two distinct strategies with respect to the delivery of contrast agents: untargeted and targeted nanoparticles for use in MR imaging. First, untargeted SPIO-based nanoparticles were evaluated for use as an indicator for the onset and progression of sepsis. With no conferred specificity towards any antigen or receptor within the body, these nanoparticles are typically uptaken by immune system-related cells and are eliminated from the body. (17) As upregulation of this uptake behavior is often correlated with specific systemic conditions such as sepsis and systemic acute inflammation, correlating nanoparticle biodistribution and organic-specific update with the progression of sepsis offers insight into the onset and progression of these conditions.

Second, the delivery of contrast agents was enhanced with the use of surface-bound targeting proteins to produce contrast agents specific to cellular targets closely associated with acute inflammation, sepsis, and cancer. The first approach began with the development of a human interleukin-based ligand scaffold that produces homodimeric targeting ligands, aimed at augmenting effective binding efficiency through an increase in avidity, or heterodimeric protein complexes, aimed at broadening the targeting spectrum through multiple-site specificity. This scaffold was then utilized to construct high affinity SPIO-based nanoparticles specific against a specific mutated form of p53 found in a broad range of cancer cell lines, resulting in a generalized cancer detection contrast agent suitable for detection of various cancer cell lines *in vitro.*

The second approach to targeting contrast agent delivery consists of the design and implementation of a leukocyte mimetic nano-micelle encapsulating SPIO. Designed with a goal of high specificity against ICAM-1, an surface-expressed intercellular adhesion molecule often overexpressed in tumor cells, tumor vascular microenvironment, and acute inflammation, this contrast agent was successfully use in visualizing acute inflammation *in vitro* and *in vivo* using MRI.

In all approaches, nanoparticle distribution was tracked and quantitatively measured using magnetic resonance imaging and by employing recently developed techniques in quantitative susceptibility mapping.

CHAPTER 1 - BACKGROUND

1.1 MAGNETIC RESONANCE IMAGING

Magnetic resonance imaging (MRI) is a widely used non-invasive imaging modality that allows for visualization of cross-sectional slices or three-dimensional volumes of an object through the use of powerful magnetic fields and radio frequency (RF) energy to align, alter, and observe the nuclear magnetization of hydrogen atoms that make up the subject of interest.

1.1.1 Precession

A nucleus that contains an odd number of protons and/or of neutrons have an intrinsic magnetic moment and angular momentum about their axes, typically referred to as a "spin." Under typical conditions, the magnetic moments of the nuclei of a bulk volume are randomly oriented, resulting in no net magnetic moment for the volume. However, when an external magnetic field is applied, the spins align relative to the applied field in one of two orientations: parallel to the applied field, or antiparallel to the applied field. As the parallel state has a slightly lower energy state, this results in slightly more spins aligned parallel to the applied field, and results in a net magnetic moment in the volume.

The bulk magnetization when exposed to an applied magnetic field can be expressed using the Bloch equation

$$\frac{d\mathbf{M}}{dt} = (\gamma \mathbf{M} \times \mathbf{B}) - \frac{(M_z - \mathrm{M}_z^0)\hat{\mathbf{z}}}{T_1} - \frac{M_x\hat{\boldsymbol{x}} + M_y\hat{\boldsymbol{y}}}{T_2}, \qquad [1.1]$$

where $\mathbf{M}$ is the bulk magnetization, $\mathbf{B}$ is the applied external magnetic field , M_x is the x component of $\mathbf{M}$, M_y is the y component of $\mathbf{M}$, M_z is the z component of $\mathbf{M}$, M_z^0 is the equilibrium magnetization that results when the volume is placed in the applied field, and vectors $\hat{\boldsymbol{x}}$, $\hat{\boldsymbol{y}}$, and $\hat{\boldsymbol{z}}$ represent the unit vectors along the *x, y*, and *z* axes, respectively. Constants T_1 and T_2 represent the rates of longitudinal and

transverse relaxation, respectively. Constant γ is the nucleus-specific gyromagnetic ratio, expressed in MHz/T.

Typically, the vectors of the x-y transverse plane are represented using complex notation, where the *x* component is represented by the real component and the *y* component is represented by the imaginary component. Thus, the transverse magnetization can be represented as

$$\boldsymbol{M}_{xy} = M_x + jM_y = \left|\mathbf{M}_{xy}\right| e^{-j\phi} , \tag{1.2}$$

where $j = \sqrt{-1}$.

If $\boldsymbol{B}_0$ is assumed to be purely in the longitudinal direction, the first term of Bloch's equation (Eq. 1.1) can be expressed as

$$\begin{aligned} \frac{dM_x}{dt} &= \gamma M_y B_z \\ \frac{dM_y}{dt} &= \gamma M_x B_z . \end{aligned} \tag{1.3}$$

Defining

$$\omega_0 = \gamma B_z , \tag{1.4}$$

where ω_0 is the frequency of procession of the nucleus in the precense of applied $\mathbf{B_0}$, we obtain

$$\begin{aligned} M_x(t) &= M_x(0)\cos\omega_0 t + M_y(0)\sin\omega_0 t \\ M_{y(t)} &= -M_x(0)\sin\omega_0 t + M_y(0)\cos\omega_0 t , \end{aligned} \tag{1.5}$$

for initial conditions $M_x(0)$ and $M_y(0)$. Expressed in complex notation, this becomes

$$\boldsymbol{M}_{xy} = \boldsymbol{M}_{xy}(0) e^{-j\omega t} , \tag{1.6}$$

for initial condition $\boldsymbol{M}_{xy}(0)$. Intuitively, this describes the precession of the magnetization vector about the applied magnetic field at a resonant frequency ω_0.

The second term of Bloch's equation (Eq. 1.1) can be likewise expressed as

$$M_z(t) = M_0 + (M_z(0) - M_z^0)e^{-t/T1}\,, \qquad [1.7]$$

for initial condition $M_z(0)$, where $M_z(t)$ is the longitudinal magnetization at the time of interest. Intuitively, this describes longitudinal relaxation, and describes the regrowth of longitudinal magnetization from $M_z(0)$ at $t = 0$ to M_z^0 as t approaches ∞.

The third term of Bloch's equation (Eq. 1.1) can be expressed as

$$\boldsymbol{M_{xy}}(t) = \boldsymbol{M}_{xy}(0)e^{-t/T_2} \qquad [1.8]$$

for initial condition $\boldsymbol{M}_{xy}(0)$, where $\boldsymbol{M}_{xy}(t)$ is the transverse magnetization at the time of interest. Intuitively, this describes the decay of transverse magnetization from $\boldsymbol{M}_{xy}(0)$ at $t = 0$ to 0 as t approaches ∞.

1.1.2 Excitation

If a second magnetic field $\boldsymbol{B}_1$ is applied, the magnetization will precess about the vector sum of $\boldsymbol{B}_0$ and $\boldsymbol{B}_1$. If $\boldsymbol{B}_1$ is applied in the orientation of the transverse plane, the magnetization vector will begin rotating away from the longitudinal axis and towards the transverse plane. However in the context of MRI, $\boldsymbol{B}_0$ is typically much larger than $\boldsymbol{B}_1$. Thus, $\boldsymbol{B}_1$ contributes only a small effect on the angle of precession, as the magnetization vector will quickly rotate out of orthogonality with $\boldsymbol{B}_1$. If instead $\boldsymbol{B}_1$ is applied such that it rotates in the transverse plane at the same frequency as the longitudinal procession frequency ω_0, $\boldsymbol{B}_1$ will remain orthogonal to the magnetization vector at all times, causing the magnetization vector to rotate or "tip" towards the transverse plane. The angle by which the magnetization vector is tipped towards the transverse plane is known as the "flip angle," and can be calculated as the integral of $\boldsymbol{B}_1$ over time.

Intuitively, $\boldsymbol{B}_1$, applied in the form of a radio frequency (RF) pulse, can be used to selectively excite nuclei only of a particular resonant frequency. This notion can be exploited to allow for the

selective excite nuclei in a spatially selective manner through the use of a spatially linear field gradient. If, for instance, a spatially linear field gradient $\boldsymbol{G}_z$ is produced along the z-axis, the precession of spins will vary linearly along the z-axis in according to

$$\omega(z) = \gamma(B_0 + G_z)\,, \qquad [1.9]$$

producing an "envelope" by which nuclei can be selectively excited based on spatial location. Gradient fields can be similarly applied along all three cardinal axes, allowing for spatial selection in three-dimensional space.

1.1.3 Signal Detection

After excitation by $\boldsymbol{B}_1$, the magnetization vector precesses about both $\boldsymbol{B}_0$ and $\boldsymbol{B}_1$, and as a result produces a temporally varying magnetic field. This in turn induces a temporally varying current in nearby conductors according to Faraday's law of induction. The observable signal can be written as:

$$S(t) = \int_{-\infty}^{\infty} \boldsymbol{C}(\boldsymbol{x})\boldsymbol{\rho}(\boldsymbol{x})e^{-j\omega_0 t}e^{-t/T_2}d\boldsymbol{x} \qquad [1.10]$$

where $\mathbf{S}(t)$ is the observed signal at time t after excitation by $\boldsymbol{B}_1$, $\boldsymbol{x}$ is a vector describing spatial position, $\boldsymbol{C}(\boldsymbol{x})$ is the coil sensitivity at position $\boldsymbol{x}$, and $\boldsymbol{\rho}(\boldsymbol{x})$ is the transverse magnetization at position $\boldsymbol{x}$ immediately after excitation by $\boldsymbol{B}_1$. Intuitively, this describes the growth of observable signal upon excitation by $\boldsymbol{B}_1$, followed by subsequent decay as the transverse magnetization decays and longitudinal magnetization regrows.

1.1.4 Spatial Encoding

If a spatially varying magnetic field $\Delta B(\boldsymbol{x})$ is applied across the subject, the frequency of procession will vary as

$$\omega(\boldsymbol{x}) = \gamma\big(B_0 + \Delta B(\boldsymbol{x})\big)\,, \tag{1.11}$$

allowing for the encoding of spatial information in the frequency of the emitted radio waves. In the presence of $\Delta B(\boldsymbol{x})$, the observable signal can be rewritten as:

$$S(t) = \int_{-\infty}^{\infty} \boldsymbol{C}(\boldsymbol{x})\boldsymbol{\rho}(\boldsymbol{x}) e^{-j\gamma\left(B_0+\Delta B(\boldsymbol{x})\right)t} e^{-t/T_2} d\boldsymbol{x}\,. \tag{1.12}$$

If the signal is demodulated by center frequency ω_0, the observable signal can be expressed as:

$$S(t) = \int_{-\infty}^{\infty} \boldsymbol{C}(\boldsymbol{x})\boldsymbol{\rho}(\boldsymbol{x}) e^{-j\gamma\Delta B(x)t} e^{-t/T_2} d\boldsymbol{x}\,. \tag{1.13}$$

In practical application, the magnetic field variation is a linear field gradient that can vary over time, and can be expressed as:

$$\boldsymbol{x}\boldsymbol{G}(t) = \Delta B(\boldsymbol{x}, t), \tag{1.14}$$

where $\boldsymbol{G}(t)$ is a vector representing the spatial magnetic field gradient at time t. The observable signal can then be expressed as:

$$S(t) = \int_{-\infty}^{\infty} \boldsymbol{C}(\boldsymbol{x})\boldsymbol{\rho}(\boldsymbol{x}) e^{-j\gamma \int_0^t G(\tau)d\tau \boldsymbol{x}} e^{-t/T_2} d\boldsymbol{x}\,. \tag{1.15}$$

If the effects T_2 decay e^{-t/T_2} are neglected and the observable signal is reparametized by:

$$\boldsymbol{k}(t) = \gamma \int_0^t G(\tau)d\tau\,, \tag{1.16}$$

the observable signal can be represented by:

$$S(k) = \int_{-\infty}^{\infty} \boldsymbol{C}(\boldsymbol{x})\boldsymbol{\rho}(\boldsymbol{x}) e^{-jk\boldsymbol{x}} d\boldsymbol{x}\,. \tag{1.17}$$

Intuitively, the observed signal can be interpreted as a Fourier transform of $\boldsymbol{C}(\boldsymbol{x})\boldsymbol{\rho}(\boldsymbol{x})$, where the Fourier transform is defined as

$$F(k) = \int_{-\infty}^{\infty} f(x) e^{-jkx} dx \,. \qquad [1.18]$$

Thus, the observed signal represents coefficients of the spatial Fourier transformer of the object being imaged, with the spatial frequency of each coefficient corresponding to the integral of the gradient waveform up to that point.

1.1.5 Image Reconstruction

The image can be reconstructed through an inverse Fourier transform of the observed signal. In application, it is not feasible to sample all Fourier coefficients necessary to perfectly reconstruct the object, and thus the reconstruction can be approximated by a continuous inverse Fourier transform:

$$\widehat{\boldsymbol{\rho}}(\boldsymbol{x}) = \frac{1}{(2\pi)^n} \int_{-\infty}^{\infty} S(\boldsymbol{k}) e^{j\boldsymbol{kx}} d\boldsymbol{k} \,, \qquad [1.19]$$

where $\widehat{\boldsymbol{\rho}}(\boldsymbol{x})$ is an estimation of the magnetization distribution weighted by the coil sensitivity function and n is the number of dimensions over which the Fourier transform is taken. As the image reconstruction is performed on discrete samples, the reconstruction can be approximated by

$$\widehat{\boldsymbol{\rho}}(\boldsymbol{x}) = \sum_i \frac{\boldsymbol{S}(\boldsymbol{k_i}) e^{j\boldsymbol{k_i x}}}{D(\boldsymbol{k}_i)} \,, \qquad [1.20]$$

where i is an index of the acquired Fourier coefficients, $D(\boldsymbol{k_i})$ is the local sampling density around the point $\boldsymbol{k}_i$. In practical application, sampling is performed on a regular Cartesian grid for a three-dimensional data set, and the estimation can be approximated by

$$\widehat{\boldsymbol{\rho}}(x,y,z) = \frac{1}{N_x N_y N_z} \sum_{m=0}^{N_x-1} \sum_{n=0}^{N_y-1} \sum_{p=0}^{N_z-1} S(m,n,p) e^{2\pi x m/N_x} e^{j2\pi y n/N_y} e^{j2\pi z p/N_z} \,. \qquad [1.21]$$

1.2 CONTRAST AGENTS

Due to the varying nature of physical properties across the spectrum of heterogeneous tissue and other materials found in the body, it becomes possible to exploit this differential to generate images. In MRI, contrast can be derived from material differences such as longitudinal, or spin-lattice, relaxation rate T_1, transverse, or spin-spin, relaxation rate T_2, and proton density PD. Through strategic pulse sequence design and parameter selection, images can be acquired that more strongly accentuate the differences in one or more of these material properties, providing a relative measure by which heterogeneous tissue types can be distinguished. For example, T_1-weighted sequences will produce images that derived contrast based on a greater sensitivity towards differences in T_1, intuitively described as the rate by which the nuclei of a material can dissipate the energy gained by an excitation pulse. As described previously, T_1 can be represented by the second term of the Bloch equation (Eq. 1.1):

$$M_z(t) = M_0 + (M_z(0) - M_z^0)e^{-t/T1}\,, \qquad [1.22]$$

for initial condition $M_z(0)$, where $M_z(t)$ is the longitudinal magnetization at the time of interest. Water in bulk phase has a long T_1 relaxation time, and will typically appear dark in images produced by a T_1-weighted sequence, whereas fat-based tissue have comparatively short T_1 relaxation times, and will typically appear bright, while water-based tissues will appear gray. Clinically, T_1-weighted images are commonly used to distinguish between gray matter and white matter of the brain by exploiting differences in fat deposition between the two tissue types. Sequences such as spin echo (SE) and gradient echo (GRE) are commonly used to acquire T_1-weighted images.

On the other hand, T_2-weighted sequences will produce images that derive contrast based on a greater sensitivity towards differences in T_2, intuitively described as the rate by which the nuclei of a material

lose phase coherence following excitation. As described previously, T_2 can be represented by the third term of the Bloch equation:

$$\boldsymbol{M_{xy}}(t) = \boldsymbol{M}_{xy}(0)e^{-t/T_2} \quad [1.23]$$

for initial condition $\boldsymbol{M}_{xy}(0)$, where $\boldsymbol{M}_{xy}(t)$ is the transverse magnetization at the time of interest. Fluids have slow T_2 relaxation rates and will typically appear bright in images produced by a T_2-weighted sequence, whereas water and fat-based tissue will appear gray. Clinically, T_2-weighted images are commonly used to imaging edemas, by which abnormal collections of fluid can be readily identified against normal tissue. Sequences such as spin echo (SE) and gradient echo (GRE) are commonly used to acquire T_2-weighted images.

However, images acquired in this manner using GRE sequences are in reality weighted by T_2^*, the apparent time constant of the non-equilibrium nuclear spin magnetization decay due to loss of phase coherent among spins. Due to physical limitations in MR scanner design and the presence of magnetic susceptibility effects, the generation of a perfect magnetic field is not possible, causing magnetic field inhomogeneities that cause nuclei to process at slightly different frequencies. This results in a rapid loss of phase coherence and, as a result, a loss of transverse magnetization. T_2^* can be approximately related to T_2 by

$$\frac{1}{T_2^*} \cong \frac{1}{T_2} + \frac{\Delta\omega}{2}, \quad [1.24]$$

where $\Delta\omega = \gamma\Delta B$. As a result, T_2^* is always less than T_2.

Numerous strategies in pulse sequence design and pulse sequence parameter selection can be employed to fully exploit differences in signal production based on T_1, T_2, T_2^*, and PD, details of which can be found in various external references.

The differences in material properties relevant to generating imaging contrast can be further enhanced through the use of contrast agents. Paramagnetic and superparamagnetic materials have the effect of decreasing T_1, T_2, and T_2^* relaxation times of protons in the immediate vicinity of the molecule, and if delivered in a specific and selective manner, can have the effect of increasing imaging contrast for structures of interest.

Paramagnetic contrast agents, such as those based on gadolinium, contain species with unpaired electrons, with paramagnetic metal ions showing increasingly suitable effect as the number of unpaired electrons in the ion increases. In addition, the electron spin-relaxation time must also match the Larmor frequency of the protons. These criteria make paramagnetic heavy metal ions such as Fe^{3+}, Mn^{2+}, and Gd^{3+} ideal for use as T_1 contrast agents. While paramagnetic heavy metal ions are toxic in their native form, it is possible to generate thermodynamically and kinetically stable ion-ligand compounds. The most common T_1 contrast agent in clinical use today is Gd-DTPA, marketed in the US market as gadopentetic acid or Magnevist. Gd-DPTA is the complex of gadolinium (as Gd^{3+}) and *d*iethylene*t*riamine*p*entacetate (as $DTPA^{5-}$) in which the gadolinium ion is surrounded by three nitrogen atoms and five oxygen atoms from carboxylate groups, with a water molecule occupying a ninth coordinate site. As the gadolinium ion has seven unpaired electrons with parallel spins, Gd-DTPA is strongly paramagnetic, which DTPA chelation significantly reduces the toxicity otherwise found in unchelated Gd^{3+}. Gd-DTPA is commonly used to image blood vessels and of inflamed or diseased edemic tissue. Gd-DTPA has also demonstrated use in imaging intracranial lesions with abnormal vascularity in the blood-brain barrier.

A second class of contrast agents based on superparamagnetic iron oxide (SPIO), which consist of nonstoichiometric microcrystalline magnetite cores that are coated with dextranes or siloxanes. The magnetite cores are typically constructed from a mixture of FeO or Fe_2O_3, and Fe_2O_3, and formed

through partial oxidation of Fe^{2+}, resulting in a cation-deficient, inverse-spinel phased core. SPIO-based contrast agents are typically significantly more effective at reducing relaxation times of neighboring nuclei than paramagnetic contrast agents. While, like paramagnetic contrast agents, these class of contrast agents have both a T_1, T_2, and T_2^*-shortening effect, clinically SPIO-based contrast agents are predominantly used in T_2*-weighted imaging. SPIO compounds are also non-toxic and quickly cleared from the patient, making them ideal for clinical application.

1.3 QUANTITATIVE SUSCEPTIBILITY MAPPING

Magnetic resonance imaging quantitative susceptibility mapping (MRI-QSM) is a technique by which arbitrary magnetic susceptibility distributions can be discerned using magnetic resonance signal phase information, typically discarded in a typical image reconstruction. As the net volume magnetic susceptibility relates linearly with the concentration of a diamagnetic or paramagnetic material contained within it, quantitatively mapping magnetic susceptibility across a volume of interest can provide valuable information about the location and susceptibilities of differing materials, and would prove particularly useful in the quantification of paramagnetic contrast agents, such as those constructed from gadolinium and super paramagnetic iron oxide (SPIO).

Volume magnetic susceptibility X_v is a dimensionless proportionality constant that indicates the degree of magnetization of a material in response to an applied magnetic field, and can be defined by the relationship

$$\mathbf{M} = X_v \mathbf{H}\,, \qquad [1.25]$$

where **M** is the magnetization of the material, measured in amperes per meter, and **H** is the magnetic field strength, measured in amperes per meter. Further, magnetic induction **B** is related to **H** by the relationship

$$\mathbf{B} = \mu_0(\mathbf{H} + \mathbf{M}) = \mu_0(1 + X_v)\mathbf{H} = \mu\mathbf{H}\,, \quad [1.26]$$

where μ_0 is the magnetic constant, $and\ (1 + X_v)$ is the relative permeability of the material. Thus, it can be shown from Maxwell magnetostatic equations and the Lorentz correction for media effects that the susceptibility distribution affects the field component along the main magnetic field according to

$$\delta_B(\vec{\mathrm{r}}) = \frac{1}{4\pi}\int \chi(\vec{r}')\frac{3\cos^2\alpha - 1}{|\vec{r}' - \vec{r}|^3}d^3\vec{r}', \quad [1.27]$$

where $\vec{r}$ is the spatial coordinate vector, α is the angle between $\vec{r}' - \vec{r}$ and the applied field, and δ_B is the relative difference field given by

$$\delta_B(\vec{r}) = \frac{B_z(\vec{r}) - B_0}{B_0}\,, \quad [1.28]$$

where B_z is the local magnetic field component along the main magnetic field. The induced field can be expressed as a convolution of the susceptibility distribution with the unit dipole response

$$\frac{3\cos^2\alpha - 1}{4\pi|\vec{r}|^3}\,, \quad [1.29]$$

and in the Fourier domain becomes a pointwise multiplication with a kernel

$$\Delta_{\mathrm{B}}(\vec{k}) = \left(\frac{1}{3} - \frac{k_z^2}{k^2}\right)\cdot \mathrm{X}(\vec{k}), \quad [1.30]$$

where Δ_B is the Fourier transform of the normalized field shift δ_B, X is the Fourier transform of χ, $(1/3 - (k_z^2)/k^2)$ is the dipole response to an external magnetic field in the Fourier domain, k is the magnitude of a Fourier domain coordinate vector $\vec{k}$, and k_z is the projection of $\vec{k}$ onto the direction of the main magnetic field. (18)

While this relation provides a straightforward method of predicting the normalized field shift $\delta_B(\vec{r})$ that result from a known susceptibility distribution $\chi(\vec{r})$, it is more practically relevant to solve for the inverse, to determine the susceptibility distribution given a known induced magnetic field. Solving

for this field-to-source "inverse problem" is complicated by the characteristic dipole response function $(1/3 - (k_z^2)/k^2)$, which has zeroes on two conic surfaces of k-space. Solving for $\mathrm{X}(\vec{k})$ via direct inversion requires the evaluation of $(1/3 - (k_z^2)/k^2)^{-1}$, which is undefined at these zeroes, resulting in an ill-posed inversion problem. While this problem can be sidestepped in practical application through careful discretization in order to avoid undefined regions, the dipole response in Fourier space may still be arbitrarily close to zero in space arbitrary close to the conic surface, resulting in severe noise propagation. (19)

The field-to-source inverse problem can be solved by various methods. Two such methods are the Calculation of Susceptibility Through Multiple Orientation Sampling (COSMOS), a multi-orientation sampling approach, and Morphology Enabled Dipole Inversion (MEDI), a method by which magnitude information is used to regularize the corresponding susceptibility map.

1.3.1 Calculation of Susceptibility Through Multiple Orientation Sampling

MRI-QSM Calculation of Susceptibility Through Multiple Orientation Sampling (COSMOS) solves the field-to-source inverse problem by oversampling the subject from multiple orientations. (18) Because the zero cone surface in the Fourier domain is fixed with regard to the main magnetic field, it is possible to resample data by first rotating the subject with respect to the main magnetic field, exposing data previously obscured by the zero cone surface while also reducing the effect of noise amplification in space near to the cone surface. Thus, the relation between the susceptibility distribution and the induced field can be rewritten as

$$\Delta_B(\vec{k}) = \left(\frac{1}{3} - \frac{k_{zp}^2}{k^2}\right) \cdot \mathrm{X}(\vec{k}), \qquad [1.31]$$

where k_{zp} is the projection of the object coordinate vector $\vec{k}$ onto the direction of the main magnetic field. Assuming that the object is rotated by θ about the x-axis orthogonal to the main magnetic field,

$$k_{zp} = k_z \cos\theta + k_y \cos\theta \ . \qquad [1.32]$$

Thus, if the object is sampled from N different angles,

$$\begin{bmatrix} \left(\frac{1}{3} - \frac{\left(k_z \cos\theta_1 + k_y \sin\theta_1\right)^2}{k^2}\right) \\ \left(\frac{1}{3} - \frac{\left(k_z \cos\theta_2 + k_y \sin\theta_2\right)^2}{k^2}\right) \\ \cdots \\ \left(\frac{1}{3} - \frac{\left(k_z \cos\theta_N + k_y \sin\theta_N\right)^2}{k^2}\right) \end{bmatrix} \cdot \mathrm{X}(\vec{k}) = \begin{bmatrix} \Delta_{B1} \\ \Delta_{B2} \\ \cdots \\ \Delta_{BN} \end{bmatrix}. \qquad [1.33]$$

A Fourier domain pointwise direct inversion is applicable as long as there exists a nonzero element among $(1/3 - k_{axisn}/k^2)$, $n = 1, 2 \ldots N$. A set of angles $\theta_1, \ldots, \theta_N$ exist to fulfill this criterion for every point in the Fourier domain when $N \geq 3$. (18) In practical implementation, this can be achieved through three samples with 120° rotation about the x-axis.

Further information pertaining to the theory and implementation of COSMOS can be found in Liu 2009.

1.3.2 Morphology Enabled Dipole Inversion

While COSMOS is easily adaptable in determining the quantitative susceptibility map of relatively small samples, physical limitations of the bore of the MR scanner makes COSMOS impractical for sampling larger subjects. Alternatively, solution to the field-to-source inverse problem can be derived through regularization that encodes *a priori* information, using a single sample. Morphology Enabled Dipole Inversion (MEDI) makes use of the observation that the locations of interfaces, or "edges," in the

susceptibility of distribution are nearly the same as those in magnitude images obtained in the same acquisition, and their discordance is assumed to be sparse.(20) This can be achieved through a weighted l_1 minimization that penalizes susceptibility at voxels that do not have a corresponding interface in the magnitude image. Expressed as a minimization

$$\min_x \left\| M\nabla_\chi \right\|_1 \quad s.t. \left\| W(\delta - F_{D\chi} \right\|_2 = \varepsilon \,, \tag{1.34}$$

where ∇ is a three-dimensional gradient operator on the vectorized susceptibility distribution χ; M is a binary gradient weighting diagonal matrix, where the non-negligible gradients in the magnitude image (define as five times greater than the background noise standard deviation in the magnitude image) and are equal to 1 otherwise; F_D is a matrix encoding the convolution with the unit dipole field $F_D = F^{-1}DF$, where D is the dipole kernel expressed in the Fourier domain; δ is the measured local field map, and W is the data weighting matrix to account for non-uniform phase noise. W and expected noise level ε are derived from the magnitude images across all echoes by calculating the error propagation from the phase noise to the field noise. The solution to the minimization problem coincidences with the unconstrained Lagrangian problem with a properly chosen parameter λ:

$$\chi^* = \mathrm{argmin}_\chi \left\| M\nabla_\chi \right\|_1 + \lambda \left\| W(\delta - F_{D\chi}) \right\|_2^2 , \tag{1.35}$$

where χ^* is the solution of the susceptibility distribution to the minimization problem. The value of λ is chosen such that $\left\| W\left(\delta - F_{D\chi}\right) \right\|_2 = \varepsilon$.

Further information pertaining to the theory and implementation of MEDI can be found in Liu 2012.

CHAPTER 2 – UNTARGETED NANOPARTICLES

Includes material previously published in: Wong R, Shou J, Wang Y. Probing sepsis and sepsis-like conditions using untargeted SPIO nanoparticles. Conf Proc IEEE Eng Med Biol Soc. 2010;2010:3053-6.(21)

2.1 INTRODUCTION

Severe sepsis is the leading cause of death in critically ill patients admitted to the medical Intensive care unit (ICU) in the United States (22). Substantial efforts have been devoted to finding effective pharmacologic therapies and improving clinical outcomes. However, to date, there has been limited, if any, success (23-25). A recent study on ALI/ARDS patients (26) showed that patients with sepsis-related lung injury continue to experience the highest fatality rates. The 28-day all-cause mortality is in excess of 30% (26). In many cases, ALI/ARDS progresses to severe sepsis and multi-organ dysfunction/failure. Despite an improved ability to monitor, support, and manage these critically ill patients, the survival rate of severe sepsis remains only 50% to 70%. The average cost of severe sepsis is more than $22,000 per case, with an average length of hospitalization of 19.6 days. Severe sepsis is a major cause of morbidity and mortality worldwide and is the 13th leading cause of death among hospitalized patients overall in the U.S. The incidence of sepsis-related ALI/ARDS and severe sepsis is expected to rise during the next decade due to the aging population, a growing population of those who are immunosuppressed due to treatments or diseases, the increased use of invasive catheters and prosthetic materials, and the growing problem of antimicrobial resistance. In the year 2010, it is estimated that there will be 934,000 new severe sepsis cases in the United States and 1,000,000 in the year 2020 (27). The annual costs associated with the treatment of patients with ALI/ARDS and severe sepsis in the U.S. alone have been estimated in excess of $5 billion and at $16.7 billion respectively (27).

Current diagnosis of sepsis-induced ALI/ARDS relies heavily on bacteria culturing of patients' blood and the patient's manifestation of clinical symptoms. Bacterial culturing of patients' blood is an unreliable diagnostic method for sepsis that also takes days for confirmation. It has been shown that only approximately 30% of clinically confirmed sepsis cases give positive identification of bacterial and viral infections (28). However, as the underlying biological changes of sepsis-induced ALI/ARDS and

severe sepsis occur hours to days before the clinical presentation of symptoms, early detection of the biological changes will provide crucial opportunities for early diagnosis and medical intervention of sepsis-induced ALI/ARDS and severe sepsis. For instance, early goal-oriented intervention is proven to lower the mortality rate of severe sepsis. This underscores importance of a better, rapid diagnostic method for sepsis-induced ALI/ARDS and severe sepsis. As an alternative to existing techniques to detection, we propose using MRI quantitative susceptibility mapping as a method of quantifiably measuring the activity of patients' immune system as a biomarker of sepsis progression.

It has been observed that Kupffer cells, comprising 80% of the liver's macrophages, exhibit immune responses during early phases of systematic infection (17). Macrophages utilize their pattern recognition receptors known as Toll-like receptors (TLRs) to sense infection by binding to certain microbial components (29). The activations of certain TLRs on the surface of macrophages will drastically increase their phagocytic activities for particle uptakes. Further, it has been observed that phagocytosis by Kupffer cells is a major mechanism by which nanoparticle-based contrast agents, such as Feridex, are cleared from the body (17). Therefore, we can utilize these commonly used, the FDA-approved contrast agents as markers in diagnosing and monitoring progression of sepsis by quantifying the amount of superparamagnetic iron-oxide nanoparticles uptaken by the host macrophages after exposure to infectious agents or their TCR-recognized components.

2.2 MATERIALS AND METHODS

2.2.1 *In Vitro* Observation of SPIO Uptake Using MRI

Murine macrophages, RAW264.7 (ATCC, Manassas, VA), cultured for no more than 15 passages, were grown to 80% confluency in Dulbecco's Modified Eagle Medium (DMEM) with 10% Fetal Bovine Serum (FBS). 1 x 10^6 cells were seeded, were allowed to incubate overnight at 37°C, 5% CO2 and were

subsequently activated by a treatment of E. coli-derived lipopolysaccharide (LPS) at a concentration of 100ng/mL in fresh media and allowed to incubate for 24 hours; untreated cells were used as negative controls. Feridex IV (Bayer AG, Leverkusen, Germany), a ferumoxide solution, was then added to the media at a concentration of 112ug of Fe/mL and allowed to incubate for 3, 6, 9, 18, and 24 hours. The media was removed by aspiration, and the cell monolayer was washed 3 times with Dulbecco's Phosphate Buffered Saline (DPBS) to remove free Feridex. Cells were trypsinized, collected and counted, and centrifuged into a pellet at the bottom of a 15mL centrifuge tube containing DPBS. The centrifuge tube was positioned in the center, lengthwise, of a 50mL centrifuge filled with DPBS, creating a cell pellet suspended in the middle of a uniform DPBS solution. The cell apparatus was scanned using a 3T Signa GE scanner (General Electric, Milwaukee, WI) with a custom birdcage coil and using an EFGRE 3D sequence, 4 TEs 3.0/3.8/5.4/10.2ms, TR 30ms, Flip Angle 30°, bandwidth 31.25 kHz, at an isotropic resolution of 500um3. Images were reconstructed and iron content was determined using the COSMOS QSM (18) and calibrated against a phantom with known iron content. Samples were additionally treated with Prussian Blue for qualitative colorimetric staining. Representative regions of Feridex incubated cell cultures were photographed at 40X on an optical microscope.

2.2.2 *Ex* Vivo Observation of SPIO Uptake Using MRI

C57BL/6 mice were divided into 4 groups of 2 mice each. Each group of mice were administered with LPS at the sub-lethal doses, as determined by previous IP injection (0, 1.25 mg/kg, 2.5 mg/kg, 5 mg/kg) and injected with Feridex IV intravenously at 10 mg/kg 24 hours later. Three hours after Feridex injection, mice were sacrificed. Livers were harvested, fixed in paraformaldehyde, and stored for MRI analysis. The livers were scanned using a 3T Signa GE scanner (General Electric, Milwaukee, WI) with a homemade birdcage coil and using an EFGRE 3D sequence, 4 TEs 3.0/3.8/5.4/10.2ms, TR 30ms, Flip

Angle 30°, bandwidth 31.25 kHz, at an isotropic resolution of 500um3. Images were reconstructed and iron content was determined using the COSMOS methodology, as described in Liu, *et al*. (18) Samples were additionally treated with Prussian Blue for qualitative colorimetric staining. Representative regions of Feridex incubated cell cultures were photographed at 40X on an optical microscope.

2.3 RESULTS AND DISCUSSION

2.3.1 *In Vitro* Observation of SPIO Uptake Using MRI

The work conducted is offered an *in vitro* proof of concept for the non-invasive quantitative measurement of SPIO uptake using QSM MRI. RAW264.7 murine monocytes were treated with lipopolysaccharide (LPS) to induce a sepsis-like cell condition. Macrophages recognize LPS through their TLR4, resulting in an increase in phagocytosis. The LPS-induced murine monocytes were subsequently incubated with the FDA-approved contrast agent Feridex IV, and were imaged using the MRI-QSM (Quantitative Susceptibility Mapping) COSMOS (Calculation of Susceptibility through Multiple Orientation Sampling) technique for the quantification of iron (18). The total detected iron was obtained for each sample after 0, 3, 6, 9, 18 and 24 hours of Feridex incubation over a total of four independent trials; the results were scaled by the number of cells counted in each sample, and averaged over all trials (Figure 2.1A). An estimation of the error of the mean was calculated with a confidence level of 95%. Representative images of the intensity field, the relative difference in the intensity field, scaled against a reference scan and the COSMOS-QSM reconstruction are shown for select samples (Figure 2.1B). Results of colorimetric staining (not shown), indicate blue-stain across all cell samples treated with Feridex, with color intensity roughly proportional to measurements obtained using COSMOS-QSM.

Results from COSMOS reconstruction indicate a statistically significant difference (CI = 95%) in the average amount of Feridex uptaken per cell after 18 and 24 hours of incubation with Feridex; LPS-activated cells uptook, on average, 4.75 times more Feridex than non-LPS-activated control cells after an 18 hour period, and 4.81 times more after the full 24 hour period. Non-LPS-activated cells demonstrated a roughly linear rate of Feridex uptake throughout the 24 hour trial (R2 = 0.977), while LPS-activated cells exhibited a roughly linear rate of uptake in two distinct regimes, separated at a point shortly after 9 hours (R2 = 0.933 for first regime, R2 = 0.999 for the second regime). These results agree with previous literature concerning LPS-activated RAW264.7 cells, where it was observed that the presence of LPS, at a concentration of 100ng/mL, maximally activate the macrophages after a comparable delay, accelerating the production of NO products and increasing phagocytic activity of similarly sized SPIO nanoparticles, when compared to that of their inactivated counterparts. (30-32) These results are qualitatively supported by the colorimetric staining. LPS-treated cell colonies show a greater concentration of internalized iron when compared to untreated cells, reflecting the greater degree of iron internalization as a result of the sepsis-like condition.

These observations demonstrate that differences in the phagocytic activity of two macrophage populations under differing conditions can be readily quantified using MR techniques. Moreover, it demonstrates that this rate of uptake can be differentiated on a statistically significant level using MRI-QSM technique. As phagocytic SPIO uptake by macrophages can be stimulated by the presence of pro--inflammatory agents, such as LPS, this strongly suggests that this technique can be expanded to the *in vivo* measurement of macrophage activity, whereby the administration of an SPIO nanoparticle, such as Feridex, can be used as a marker to directly measure macrophage activity. Tracking the biodistribution of these contrast agents using MRI-QSM may provide an indicator of overall immune system function as

a non-invasive tool to identify and diagnose systemic immune responses, such as those that occur under sepsis.

2.3.2 *Ex* Vivo Observation of SPIO Uptake Using MRI

With the demonstration of observable differences between LPS-treated RAW264.7 cells and untreated control cells, we have progressed to a LPS-based *in vivo* mouse sepsis model to determine if the same differential in Feridex uptake could be observed in an animal model and to judge the effectiveness of iron-quantification in providing an indicator for sepsis. Iron aggregation in each liver was determined using COSMOS-QSM and normalized by liver mass (Figure 2.2A). An estimation of the error of the mean was calculated with a confidence level of 95%. Representative images of the intensity field, the relative difference in the intensity field, scaled against a reference scan, and the COSMOS-QSM reconstruction are shown for select samples (Figure 2.2B). Histograms of susceptibility concentration per voxel, normalized by the number of overall voxels, were generated for LPS-treated mouse livers and those from negative controls; voxels in the 99^{th} or greater percentile of susceptibility concentration were averaged for each treatment regimen (Figure 2.2C).

Independent of analysis methodology, MRI-QSM reconstructions under all treatment regimens indicate a very high amount of Feridex uptaken for all samples far above the background, indicating that the effects of the Feridex injection can be readily observed and quantified using COSMOS.

A statistically significant difference does not exist in total measured Feridex uptake between livers of mice treated with differing concentrations of LPS. After normalizing each measurement by the overall mass of each liver, the difference in averages between each group differed by as much as 20%, but failed to be differentiated beyond a 95% confidence interval. However, livers of LPS treated mice had a wider per-voxel susceptibility concentration distribution compared to that of negative controls.

Moreover, when comparing the 99th percentile of liver voxels ordered by increasing susceptibility concentration, LPS treated mice were found to have significantly higher concentrations, averaging an increase of 33% in LPS treated mice compared to negative controls. This indicates that while LPS treatment does not significantly alter the total amount of Feridex uptake, LPS treatment has an observable effect on uptake behavior, leading to quantifiably greater localized concentrations of Feridex compared to negative controls.

While differentiation can be drawn between observable Feridex uptake behavior between LPS treated mice and negative controls, the lack of measurably significant differences in total Feridex uptake by the liver makes this technique less attractive as a tool for clinical sepsis diagnosis. Ordering voxels by increasing susceptibility concentration is highly dependent on the creation of accurate region of interest segmentations of the liver for each subject, as voxels of the liver containing low concentration of susceptibility could dramatically affect the calculation of the highest 99th percentile. While this segmentation is a relatively simple task *ex vivo*, with organs removed and mounted in a uniform agarose environment, delineations between tissue are significantly more vague *in vivo* and could dramatically affect the accuracy of analysis. Ideally, differentiation between treatment regimens should be based on total measured contrast agent uptake, a statistic that is more dependent on voxels of high susceptibility concentration rather than on correctly identifying voxels of low susceptibility and of ambiguous tissue type. While Feridex is a contrast agent with no biospecificity conferred by surface ligands or chemistry, an SPIO nanoparticle could conceivably be constructed to increase contrast agent delivery and retention based on sepsis-specific mechanisms as a means of increasing contrast between treatment regimens. An exploration of development of potential targeting moieties, including the use of Tissue Factor (TF), anti-p53 T-cell receptors (TCRs), and anti-ICAM-1 integrins, and their use in conjunction with SPIO

nanoparticle-based contrast agents in the context of sepsis and acute inflammation detection is described in Chapters 3-5.

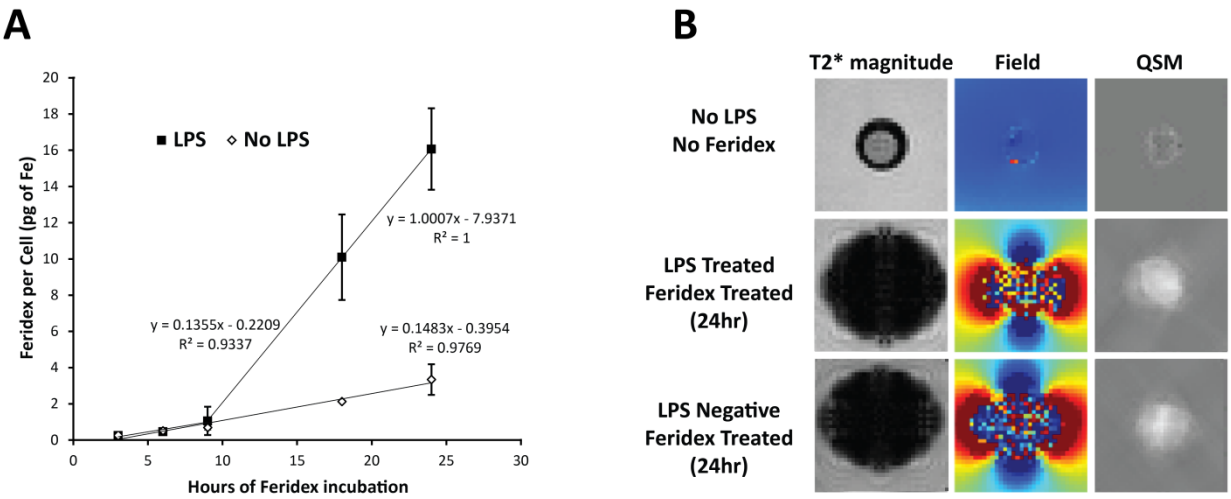

Figure 2.1. Comparison of Feridex uptake by RAW264.7 cells *in vitro*. A) Mass of Feridex uptaken by LPS-treated RAW264.7 cells (100ng/mL) and control cells, measured using COSMOS, normalized by number of cells. LPS-treated cells show a significantly increased amount of Feridex uptaken per cell. B) Traditional T2* weighted magnitude images, field maps, and QSM reconstructions of LPS-treated RAW264.7 cells incubated with Feridex, and control cells. The presence of iron is noted by hypointensity in T2* weighted magnitude images, observable localized distortions in the magnetic field, and both presence and quantity of iron are illustrated by positive values in QSM.

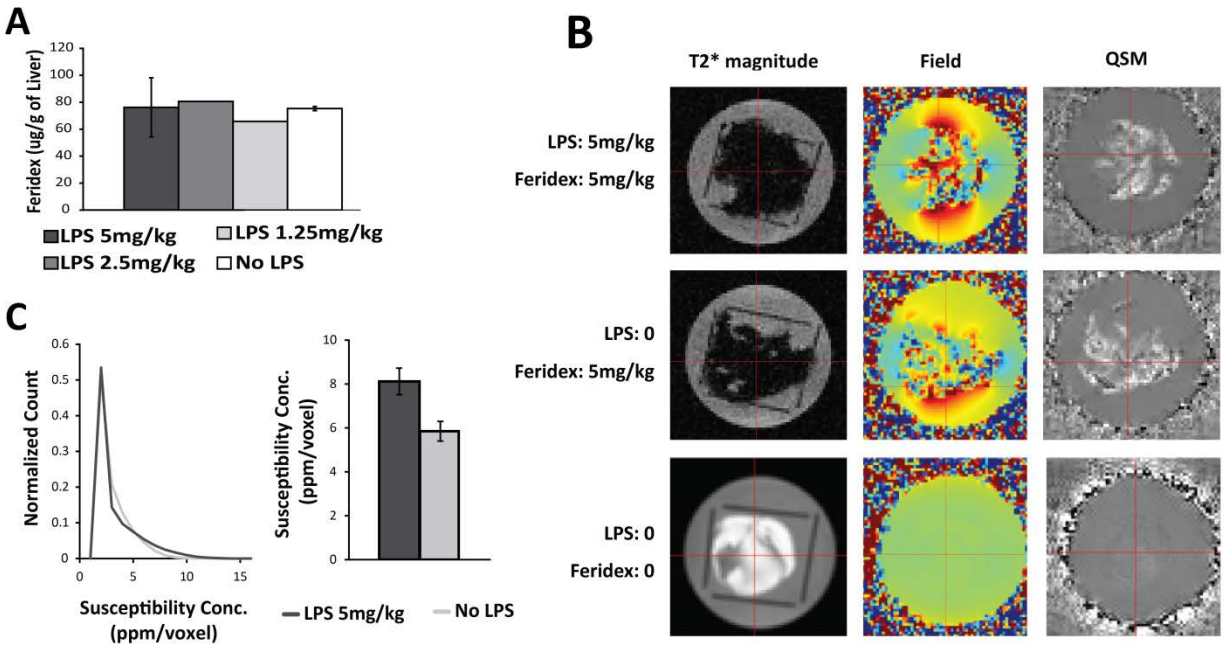
A
Feridex (ug/g of Liver)
120
100
80
60
40
20
0
LPS 5mg/kg
LPS 1.25mg/kg
LPS 2.5mg/kg
No LPS
B
T2* magnitude
Field
QSM
LPS: 5mg/kg
Feridex: 5mg/kg
LPS: 0
Feridex: 5mg/kg
LPS: 0
Feridex: 0
C
Normalized Count
0.6
0.5
0.4
0.3
0.2
0.1
0
0
5
10
15
Susceptibility Conc. (ppm/voxel)
Susceptibility Conc. (ppm/voxel)
10
8
6
4
2
0
LPS 5mg/kg
No LPS

Figure 2.2. Comparison of Feridex uptake in mouse livers *in vivo.* A) Amount of iron detected by COSMOS, normalized for the mass of each liver. Each group was injected with differing concentrations of LPS (LPS 5mg/kg, LPS 2.5mg/kg, LPS 1.25 mg/kg, and No LPS) and injected with 10mg/kg of Feridex after 24 hours of LPS incubation. No statistical difference can be found between each treatment regimen. B) Traditional T2*-weighted magnitude images, field maps, and QSM reconstructions of livers from mice treated with LPS and Feridex and imaged ex vivo. The presence of iron is noted by hypointensity in T2* magnitude images, observable localized distortions in the magnetic field, and both presence and quantity of iron are illustrated by positive values in QSM. C) Histogram of susceptibility concentration per voxel of LPS-treated mouse livers and negative controls, normalized by the number of overall voxels. LPS treated mice had a wider concentration distribution than that of negative controls. B) 99th percentile of the susceptibility concentration values show a statistically significant difference between LPS and control samples ($p > 0.95$).

CHAPTER 3 – DEVELOPMENT OF IMPROVED TARGETING MOEITIES

Includes material previously published in: Wong RL, Liu B, Zhu X, You L, Kong L, Han KP, et al. Interleukin-15:Interleukin-15 receptor alpha scaffold for creation of multivalent targeted immune molecules. Protein Eng Des Sel. 2011;24(4):373-83. (33)

3.1 INTRODUCTION

Previous studies have shown that novel dimeric targeting proteins can be created for the purposes of either augmenting effective affinity through formation of homodimers or broadening the spectrum of recognition through formation of multiple specific heterodimers. A variety of protein interaction domains have been employed to generate such molecules. Initially, leucine zipper domains were used as association partners for dimerization of fusion proteins. In this approach, hydrophobic interaction of leucine zipper domains is mediated by regularly spaced leucines in parallel α-helices, while the dimerization partner is determined primarily by charged residues immediately outside of the hydrophobic core, that form salt bridges (34). This interaction is exemplified by the Fos and Jun family of proteins, which preferentially form heterodimers without significantly affecting the binding activity of fused recognition domain. This approach provides a versatile scaffold to create multimeric complexes (35). However, there are limitations to this approach for development of therapeutic proteins. Most prominently, Fos and Jun are intracellular proteins that accumulate almost exclusively within the nucleus. Thus, soluble and secreted Fos and Jun fusions are usually produced using baculovirus or insect cell expression systems (36, 37), a relatively low yielding and not easily scalable manufacturing process. In an attempt to create functional bispecific molecules, antibody (Ab) domains linked to Fos-Jun were produced in bacterial or mammalian cells, but subunit homodimerization was observed,(38, 39) which complicated the purification process and reduced the overall yield.

In addition to leucine zipper motifs, helix-turn-helix self dimerizing peptides, tri- and tetrameric subdomains of collagen and p53 have been used as scaffolds by which to create multivalent molecules (40-43). These interaction domains primarily serve as molecular scaffolds and lack other functional activities per se. Moreover, fusion proteins containing these domains often require further optimization to promote stable multimer formation and specialized production cell lines and purification methods

that are tedious or impose regulatory hurdles for therapeutic development. Many of these scaffolds are derivatives of either nonhuman protein domains or non-native components of plasma that may exhibit poor pharmacokinetic properties and pose the risk of immunogenic responses that could limit their therapeutic potential.

IgG domains, particularly the Fc fragment, have been used successfully as dimeric scaffolds for a number of therapeutic molecules including approved biologic drugs. For example, dimerization of the soluble human tumor necrosis factor-α (TNF-α) receptor linked to the human IgG1 Fc domain results in up to 1,000 times more potent TNF-α antagonist activity than the monomeric receptor and provides the fusion with a five-fold longer serum half-life than the monomeric form (44). In addition to its dimerization activity, the Fc fragment also provides cytotoxic effector functions through the complement activation and interaction with Fcγ receptors displayed on natural killer (NK) cells, neutrophils, phagocytes and dendritic cells (45). In the context of anti-cancer therapeutic Abs and other Ab domain-Fc fusion proteins, these activities likely play an important role in efficacy observed in animal tumor models and in cancer patients (46). Thus, IgG domains have been used as a scaffold to form bispecific Abs to improve the quality and quantity of products generated by the traditional hybridoma fusion technology (47, 48). Although these methods bypass the shortcomings of leucine zipper and the synthetic scaffolds, there continue to be difficulties in producing bispecific Abs in mammalian cells at levels sufficient to support clinical development and use. Additionally, the Fc-mediated effector functions of such fusions may not be adequate or appropriate in a number of therapeutic applications. There has been considerable interest in improving and expanding on the effector activity of the Fc domain and developing other means of recruiting cytolytic immune responses, including T cell activity, to the disease site via targeted therapeutic molecules (46, 49).

In an effort to develop a new, human-derived immunostimulatory multimeric scaffold, we focused on the use of human IL-15 (hIL-15) and IL-15 receptor domains. Human IL-15 is a member of the small four α-helix bundle family of cytokines that associates with the hIL-15 receptor α-chain (hIL-15Rα) with a high binding affinity (Equilibrium dissociation constant (K_D) ~10^{-11} M) (50). The resulting complex is then trans-presented to the human IL-2/15 receptor β/common γ chain (hIL-15Rβγ_C) complexes displayed on the surface of T cells and NK cells. This cytokine/receptor interaction results in expansion and activation of effector T cells and NK cells, which play an important role in eradicating virally infected and malignant cells (51). Normally, hIL-15 and hIL-15Rα are co-produced in dendritic cells to form complexes intracellularly that are subsequently secreted and displayed as heterodimeric molecules on cell surfaces (52). Thus, the characteristics of hIL-15 and hIL-15Rα interactions suggest that these inter-chain binding domains could serve as a novel, human-derived immunostimulatory scaffold to make soluble dimeric molecules capable of target-specific binding. We have previously reported use of fusion proteins comprising soluble T cell receptor (TCR) proteins as disease antigen-specific recognition domains (53, 54). In this report, we extend these studies to describe the generation and characterization of a number of fusion proteins comprising TCR and CD8 binding domains as building blocks to demonstrate the feasibility of using hIL-15:hIL-15Rα scaffold to create both soluble bivalent dimers with increased functional binding affinity toward target antigens and heterodimers for multiple-site-specific protein complexes. We also show that these fusion proteins retain potent hIL-15 activity capable of stimulating immune effector cell responses.

3.2 MATERIALS AND METHODS

3.2.1 Cell Culture

The HLA-A*0201-restricted, p53 (amino acids (aa) 149-157) peptide specific cytotoxic T lymphocytes (CTLs) were obtained from Dr. L. Sherman (The Scripps Research Institute, La Jolla, CA) (55). The H-2K^b-restricted, ovalbumin (OVA) (aa257-264) peptide specific CTLs, derived from OT1 transgenic mice, were kindly provided by Dr. L. Lefrancois (University of Connecticut, Farmington, CT). The 293GP cell line was provided by Dr. R. Morgan (National Cancer Institute, Bethesda, MD). Chinese hamster ovary (CHO), CTLs, T2, EL4, and 293GP cells were cultured in complete Iscove's modified Dulbecco's medium (IMDM) (IMDM plus 10% fetal bovine serum (HyClone, Logan, UT). 32Dβ cells (56) were cultured in IMDM complete medium plus 10 ng/ml rhIL-15 (kindly provided by Dr. J. Yovandich, NCI-Frederick, MD).

3.2.2 Materials

The p53 (aa149-157: STPPPGTRV), p53 (aa264-272: LLGRNSFEV), OVA (aa257-264: SIINFEKL), vesicular stomatitis virus (VSV) (nucleoprotein aa52-59: RGYVYQGL) peptides were purchased from Peptide 2.0 Inc. (Chantilly, VA). Bacterial expression vectors for producing human β2 microglobulin (β2m) and soluble HLA-A*0201 molecules were provided by Dr. J. Altman (Emory University, Atlanta, GA). All oligonucleotide primers were purchased from Sigma Aldrich Corp. (Woodlands, TX). The anti-human TCR Cβ (BF1) 8A3.31 and W4F.5B monoclonal Abs (mAbs) and anti-mouse TCR H57-597 mAb were purified via protein A sepharose from the supernatants of hybridoma cells purchased from ATCC (Manassas, VA). Assay reagents include anti-mouse CD8α and β mAbs (Biolegend, San Diego, CA), anti-human IL-15 mAb (R&D Systems, Minneapolis, MN), streptavidin-horse radish peroxidase (SA-HRP) and streptavidin-phycoerythrin (SA-PE) (Jackson ImmunoResearch, West Grove, PA). The pNEF38 and pDEF38 vectors used in this study were described previously (57). The pMSGV-1 vector (58) with the puromycin resistant gene (56) was further modified by introducing the CMV promoter to enhance gene expression.

3.2.3 Methods

3.2.3.1 Construction of scTCR fusion expression vectors

Generation of a soluble single-chain (sc) three-domain TCR construct, c264scTCR, has been described previously (59). This protein recognizes the human p53 peptide (aa264-272) presented in the context of HLA-A*0201. Fusions between the c264scTCR domain and human IL-15 (hIL-15), hIL-15 N72D and D8N muteins or the sushi domain of human IL-15Rα (aa 1-66 of hIL-15Rα) (hIL-15RαSu) linked via a mutated human IgG1 hinge region were generated as described previously (56). The hIL-15RαSu gene construct was further modified by the addition of sequence encoding a flexible linker and birA tag (GGLNDIFEAQKIEWHE) at the 3' end of the construct by PCR. The details of the linker sequences between the protein domains of the fusion proteins are provided in Supplemental Table 3-S.

Similar scTCR fusion constructs were generated from TCR α and β chain genes cloned from either H-2K^{b}-restricted, OVA (aa257-264) peptide-specific or HLA-A*0201-restricted, p53 (aa149-157) peptide-specific CTLs using SMART RACE cDNA Amplification Kit (Clonetech, Mountain View, CA). The resulting constructs encode an OVA peptide-specific scTCR, referred to as OT1scTCR, comprising murine TCR Vα linked to murine TCR Vβ–Cβ domains via a flexible peptide linker or a p53 (aa149-157) peptide-specific scTCR, referred to as c149scTCR, comprising a murine TCR Vα–linker– murine TCR Vβ–human TCR Cβ fusion. These scTCR genes were linked to the hIL-15 mutein and hIL-15RαSu/birA genes in a similar approach used for the c264scTCR fusions except the c149scTCR/hIL-15N72D construct did not contain the human IgG1 hinge region, which could be deleted without affecting IL-15 activity. The OT1scTCR gene was also fused to the birA tag sequence for generation of the OT1scTCR/birA fusion. To construct an OT1 TCRα/β heterodimer, the OT1 TCR Vα-Cα and Vβ-Cβ coding regions were linked to the hIL-15 and hIL-15RαSu/birA genes, respectively, to create the OT1TCRα/hIL-15 and OT1TCRβ/hIL-

15RαSu/birA genes. The 264TCRα/hIL-15D8N and 264TCRβ/hIL-15RαSu/birA genes were constructed using a similar approach. For the scCD8 fusions, the murine CD8α and CD8β genes were amplified using the SuperScript One-Step RT-PCR method (Invitrogen, Carlsbad, CA) from total RNA extracted from T cells obtained from C57BL/6 mice. A flexible linker sequence was inserted between the CD8α and CD8β chain genes and the scCD8 construct was fused to the hIL-15RαSu/birA gene. The resulting c264scTCR/hIL-15RαSu/birA, OT1scTCR/hIL-15RαSu/birA, OT1scTCR/hIL-15D8N, OT1TCRβ/hIL-15RαSu/birA and OT1scTCR/birA fusion genes were expressed in the neo^R-based pNEF38 vector whereas the OT1TCRα/hIL-15 fusion was expressed in the DHFR-based pDEF38 vector. The c149scTCR/hIL-15N72D, 264TCRα/hIL-15D8N, 264TCRβ/hIL-15RαSu/birA and scCD8/hIL-15RαSu/birA fusion genes were expressed in the modified pMSGV retroviral vector.

3.2.3.2 Fusion protein production and purification

Expression vectors containing the various fusion constructs were introduced into CHO cells by either transfection (pNEF38 and pDEF38 vectors) or transduction (pMSGV retroviral vectors). The retroviral particles carrying the pMSGV fusion constructs were generated by transfecting 293GP packaging cells as previously described (60). The scTCR fusion proteins were purified from recombinant CHO cell culture supernatants by immunoaffinity chromatography, using the anti-human TCR Cβ mAb (BF1) 8A3.31 for c264scTCR fusion proteins and the anti-mouse TCR Cβ mAb H57-597 for OT1scTCR fusion proteins as described previously (59, 61). The purified fusion proteins with birA tag were biotinylated with biotin ligase (Avidity, Denver, CO) in the presence of excess biotin, according to the manufacturer's instructions. The biotinylated fusion proteins were multimerized with SA-HRP and SA-PE for ELISA and flow cytometry, respectively.

The purified fusion proteins were analyzed by reducing SDS poly acrylamide gel electrophoresis (SDS-PAGE) (12% Bis Tris gel) followed by staining with SimplyBlue Safe Stain (Invitrogen). Formation of hIL-15:hIL-15RαSu dimers was characterized by size-exclusion chromatography (SEC). The purified protein samples (200 µl) were applied to Superdex 200HR 10/30 column (GE Healthcare, Piscataway, NJ) at concentration of 0.33 mg/ml in PBS. The samples were eluted at a flow rate 0.7 ml/min.

3.2.3.3 Preparation of peptide/MHC class I (pMHCI) tetramers

The murine H-2K^b gene was cloned from total RNA extracted from C57BL/6 mouse lymphocytes as described above. The extracellular region was ligated into the HLA-A*0201 heavy chain expression vector replacing the HLA-A*0201 coding sequence (62). The β2m, HLA-A*0201 and H-2K^b expression vectors were individually transformed into *E. coli* and expression of the recombinant proteins were induced as described (62), and were expressed as insoluble inclusion bodies. The active and soluble proteins in complex with the peptides were obtained by the re-folding method described at http://www.microbiology.emory.edu/altman/jdaWebSite_v3/ptetPrepOverview.shtml. The p53 (aa264-272) and (aa149-157) peptide/HLA-A*0201 reagents are referred to as A2/p53.264-272 and A2/p53.149-157, respectively, and the OVA (aa257-264) peptide/H-2K^b is referred to as K^b/OVA.257-264.

3.2.3.4 ELISA

Immunoplates were coated with (BF1) 8A3.31 mAb for capturing c264scTCR fusion proteins or with H57-597 mAb for capturing OT1scTCR fusion proteins. After washing, the proteins were detected using various probes as detailed in the Results section. ABTS (2,2'-azinobis [3-ethylbenzothiazoline-6-sulfonic acid]- diammonium salt) substrate was then added and absorbance was measured at 405 nm using a 96-well plate reader.

3.2.3.5 Flow Cytometry

For characterization of the c264scTCR fusion protein complexes, T2 cells were pulsed with p53 (aa264-272) peptide at 37ºC for 2 h in the presence of peptide loading enhancer (PLE, Altor BioScience Corp., Miramar, FL). For the OT1scTCR fusion protein complexes, murine lymphoma EL4 cells were pulsed with OVA peptide at 100 µg/ml and PLE at 37ºC for 6 h. The various birA fusion proteins (complexed with SA-PE) were added and incubated at 4ºC for 1 h. The samples were washed two times and analyzed on a FACScan flow cytometer using CellQuest software (BD Biosciences, San Jose, CA). To assess IL-15 domain binding activity, 32Dβ cells were incubated with 320 nM of the c264scTCR fusion protein complexes for 30 min at 4°C. The binding of the proteins was in turn detected with biotinylated (BF1) 8A3.31 mAb for 15 min and SA-PE (5 µg/ml each) for 15 min. The stained cells were analyzed by flow cytometry as described above.

3.2.3.6 Cell proliferation assays

Cell proliferation was measured as previously described (56). Briefly, 32Dβ cells (1 x 10^4 cells/well) were incubated with increasing concentrations of scTCR/hIL-15 or scTCR/hIL-15 muteins in the presence or absence of an equal molar concentration of scTCR/hIL-15RαSu for 48 h at 37°C. Cell proliferation reagent WST-1 (Roche Applied Science, Indianapolis, IN) was added during the last 4 h of cell growth according to the manufacturer's procedures. Conversion of WST-1 to the colored formazan dye by metabolically active cells was determined through absorbance measurements at 440 nm. The EC_{50} was determined with the dose-response curve generated from the experimental data by nonlinear regression variable slope curve-fitting with Prizm4 software (GraphPad Software, La Jolla, CA).

3.2.3.7 Surface plasmon resonance

The affinity constants of the OT1scTCR fusion proteins to their cognate pMHCI were determined using surface plasmon resonance (SPR) methodology on a BIAcore 2000 instrument (GE Healthcare). Biotinylated pMHCI complexes were immobilized onto the streptavidin-coated surface of a SA5 sensor chip (GE Healthcare) by injecting protein at 2 µg/ml in HBS buffer (10 mM HEPES, 150 mM NaCl, 3.4 mM EDTA, 0.005% P20 surfactant, pH 7.4) at a flow rate of 10 µl/min. This resulted in 1000-1200 RU of immobilized pMHCI complexes. The purified OT1scTCR fusion proteins were diluted to 1 µM, 0.5 µM and 0.25 µM in HBS. Each concentration was injected once (50 µl) at a flow rate of 10 µl/min over a freshly immobilized pMHCI surface as well as over a control streptavidin surface blocked with biotin (baseline) and the binding curves were registered. The dissociation constant (K_D) and association (k_{on}) and dissociation (k_{off}) rates were calculated from the corrected binding curves (baseline subtracted) using the BIAevaluation 4.1.1 software (GE Healthcare).

3.3 RESULTS

3.3.1 Creation of Biologically Active Bivalent Dimers Using the hIL-15:hIL15Rα Scaffold

We have previously shown that a biologically active, bifunctional fusion protein, designated as c264scTCR/hIL-15, could be created by fusing the N-terminus of hIL-15 to a single-chain TCR (c264scTCR) (56) (Figure 3.1A). In this construct, c264scTCR was used as a functional recognition domain based on its specific binding activity to the p53 (aa264-272) peptide/HLA-A*0201 complex. We constructed a similar fusion protein with c264scTCR and the sushi-binding domain (aa 1-66) of human IL-15Rα (hIL-15RαSu), which has been shown to contain the structural elements responsible for hIL-15 binding (63). This fusion protein was genetically linked at the C-terminus to a birA peptide tag to allow for biotinylation and subsequent multimerization in the presence of streptavidin (64). This fusion protein is designated

c264scTCR/hIL-15RαSu/birA (Figure 3.1B) and its expression and purification from CHO cells were similar to that of c264scTCR/hIL-15. These hIL-15RαSu/birA and hIL-15 fusion proteins (and others described below) could be readily produced and purified from cell-culture supernatants at the 2 to 8 mg/liter level without much efforts of cell line screening for high producers or process optimization. Additionally, analysis by reducing SDS-PAGE indicated that the purified preparations predominantly consisted of a protein band that migrates at a molecular weight 10 to 15 kDa greater than that calculated from the protein sequence, presumably due to glycosylation expected for these mammalian cell produced proteins (Figure 3.1C). Based on the high specific binding activity between the hIL-15 and hIL-15RαSu domains, we anticipated that the fusion proteins could form a heterodimeric complex. In addition, examination of the crystal structure of the human IL-15:IL-15Rα complex indicated that the N-termini of the two proteins are at opposite ends of the complex approximately 50 Å apart (65) (Figure 3.1A). Hence, fusion of the scTCR domains to these regions is not expected to block complex formation. Initial evidence of binding between the c264scTCR/hIL-15 and c264scTCR/hIL-15RαSu/birA fusion proteins was observed in ELISAs using the plate-bound c264scTCR/hIL-15RαSu/birA to capture hIL-15 and c264scTCR/hIL-15 proteins (56).

To further characterize the dimeric c264scTCR fusion protein complexes (referred to as c264scTCR dimer), equal molar amounts of purified c264scTCR/hIL-15 and c264scTCR/hIL-15RαSu/birA fusion proteins were mixed and allowed to associate at room temperature for more than 10 min. The complexes and the individual protein fusions were evaluated by size exclusion chromatography. As shown in Figure 3.1D, the mixture of the two fusion proteins resulted in a major peak with a molecular weight corresponding to dimeric form of the major species found in the individual fusion protein preparations. Thus, the appearance of the larger molecular weight species in the c264scTCR dimer preparations is evidence that the heterodimeric complex has been generated. The c264scTCR dimer

was compared with monomeric c264scTCR/birA protein for their ability to bind the TCR-specific antigen, p53 (aa264-272)/HLA-A*0201. In each case, the proteins were biotinylated with biotin ligase followed by complexing with SA-PE to generate multimeric flow cytometry staining reagents as previously described (64). When used to stain HLA-A*0201-positive T2 cells pulsed with varying concentrations of p53 (aa264-272) peptide, both reagents exhibited antigen-specific binding that increased in a peptide-concentration dependent manner (Figure 3.2A). However, the staining reagents comprising the c264scTCR dimer stained up to three times better than the monomer-derived c264scTCR/birA counterparts (Figure 3.2B). These data suggest that dimerization through IL-15:IL-15Rα interaction preserves the functional activity of the scTCRs and increases the effective affinity of scTCR fusion complex to its cognate HLA/peptide through increased avidity. Similar results were observed when biotinylation via the birA tag was directed to the C-terminus of the scTCR/hIL-15 of the complex (data not shown). This demonstrates that the C termini of both the IL-15 and IL-15Rα domains are accessible to conjugation to molecular probes of significant size (MW of streptavidin is approximately 60 kDa) without interfering with either the dimerization or antigen binding domains of the fusion protein complex.

These studies were extended to examine the possibility of generating bispecific molecules. A second scTCR (c149scTCR) was created which recognizes an HLA-A*0201 restricted epitope of the human p53 protein spanning the amino acid residues of 149 to 157 (55). The sequence encoding this scTCR fused to hIL-15 domain, designated as c149scTCR/hIL-15, was co-expressed in CHO cells with the c264scTCR/hIL-15αSu/birA fusion (Figure 3.1B). The fusion complex generated in the supernatant of the recombinant CHO cell culture was immobilized using an anti-IL-15 Ab and probed either by HRP-labeled p53 (aa264-272) or p53 (aa149-157) peptide/HLA-A*0201 tetramers. As shown in Figure 3.2C, the anti-IL-15 Ab captured fusion protein complex was able to bind both of the peptide-loaded HLA tetramers.

The result demonstrates that the individual scTCR molecules retain functional activity when fused to the hIL-15:hIL-15RαSu scaffold and the spatial arrangement of hIL-15:hIL-15RαSu complex does not significantly interfere with the packing of the scTCR domains, which have individual molecular weights of approximately 40 kDa.

To demonstrate the broad utility of the hIL-15:hIL-15RαSu scaffold for protein dimerization, we created a second dimeric scTCR fusion complex by pairing two single-chain OT1 TCRs, one fused to the N-terminus of hIL-15 and another to the N-terminus of hIL-15RαSu/birA protein (Figure 3.1B). OT1 is a well-characterized TCR recognizing an epitope of OVA protein spanning the amino acid residues 257 to 264 in the context of murine H-2K^b (66). OT1 single-chain TCR (OT1scTCR) gene was generated and fused to either the hIL-15 or hIL-15RαSu/birA domain for recombinant CHO cell expression (Figure 3.1C, lanes 5 and 6). The purified OT1scTCR fusion proteins were then mixed to form the OT1scTCR dimer protein complex. The individual fusions and protein complex were found to have pMHCI binding activity in ELISA using anti-mouse TCR Cβ H57 Ab as a capture reagent and HRP-labeled, OVA (aa257-264) peptide-loaded H-2K^b tetramer as a probe (Supplemental Figure 3.1-S). To distinguish the difference in binding activity between the OT1scTCR dimer and OT1scTCR/birA monomer, we conducted flow cytometry analysis similar to those described above for the c264scTCR dimers but with H-2K^b-positive EL4 cells loaded with OVA (aa257-264) peptide. As shown in Figure 3.3, SA-PE tetramers comprising the OT1scTCR dimer indeed stained significantly better than those comprising monomeric OT1scTCR/birA fusions. We also performed surface plasmon resonance assays to assess the binding affinity of the OT1scTCR monomer and dimer against the biotinylated OVA (aa257-264) peptide-loaded H2-K^b/birA complexes immobilized on a streptavidin sensor chip. The apparent binding affinity (K_D) of the OT1scTCR dimer to OVA peptide/H-2K^b complexes was estimated to be about 30 μM, whereas no binding was observed for the monomeric OT1scTCR/birA fusion protein (Table 3.1). These data confirm

that dimerization through hIL-15:hIL-15Rα interaction preserves the biological activity of the scTCRs and increases the effective affinity of the scTCR molecule to its cognate pMHCI complexes through increased avidity.

3.3.2 Creation of a Biologically Active Heterodimer

Since the CD8 molecule has been previously demonstrated to play a pivotal role in the interaction between OT1 TCR and its cognate OVA peptide/H2-K^b complex (67), the hIL-15:hIL-15RαSu scaffold provides an opportunity to assess whether CD8 molecule enhances OT1 TCR binding affinity to OVA peptide/H-$2K^b$ expressed on the cell surface and under cell-free and adhesion molecule-free conditions. To achieve this, we first created a murine CD8 molecule in single-chain format (scCD8) by fusing the extracellular domains of the α and β chains of the murine CD8 using a flexible linker. This fusion gene was fused to the hIL-15RαSu/birA construct in a retroviral expression vector. Recombinant retrovirus was then used to infect a CHO cell line expressing the OT1scTCR/hIL-15 fusion protein in order to create an scTCR/scCD8 heterodimeric complex (Figure 3.1B). The fusion protein complex was purified from the supernatant of the cultured recombinant CHO cells using the anti-TCR Ab-based affinity chromatography as described above. SDS-PAGE analysis of the purified protein complex revealed protein bands of the appropriate molecular weight for the OT1scTCR/hIL-15D8N (calculated MW 56 kDa) and scCD8/hIL-15RαSu/birA fusions (calculated MW 48 kDa) (Figure 3.1C, lane 7). The protein complex was subjected to ELISA using anti-TCR Ab as the capture reagent and either the biotinylated anti-mCD8α or anti-mCD8β mAbs as probes. As shown in Figure 3.4A, the anti-TCR Ab-immobilized fusion complex contains both the CD8α and CD8β and, thus, indicates formation of an OT1scTCR/scCD8 heterodimer. We used flow cytometry analysis to compare the binding activity of the OT1scTCR/scCD8 heterodimer with the OT1scTCR dimer to varying amounts of OVA peptide/H-$2K^b$ complexes displayed on the cell surface. As

shown in Figure 3.4B, SA-PE staining reagents comprising the OT1scTCR/scCD8 heterodimer could readily detect OVA peptide/H-2K^b complexes on EL4 cells loaded with as little as 10 ng/ml OVA peptide, whereas little or no staining was observed at this peptide concentration when comparable reagents comprising the OT1scTCR dimer were used. Higher background OT1scTCR/scCD8 heterodimer staining was observed on EL4 cells that were not pulsed with peptide, suggesting peptide-independent interactions were occurring between the CD8 domain and MHC molecules on the cell surface. Similar effects have been reported for pMHCI tetramers binding to CD8 molecules expressed on T cells (68).

The results for peptide-specific interactions of the OT1scTCR/scCD8 heterodimer were further confirmed by surface plasmon resonance analysis. The binding affinity (K_D) of the OT1scTCR/scCD8 heterodimer to OVA peptide/H-2K^b complexes was estimated to be 2.6 μM, which is significantly higher than the ~30 μM observed for the OT1scTCR dimer (Table 3.1, Supplemental Figure 3.2-S). Neither fusion protein showed any binding to control VSV peptide/H-2K^b complexes. The difference in specific pMHCI binding activity is surprising given that the bivalent nature of the OT1scTCR dimer is expected to provide increased functional affinity in this assay format. Additionally, similar SPR binding studies conducted with soluble TCR, CD8 α/β and pMHCI proteins as independent components showed only weak interactions (K_D 30-100 μM) between CD8 protein and peptide/H-2K^b complexes and no apparent cooperative effects of CD8 on TCR:peptide/H-2K^b interactions (69, 70). Taken together, these data indicate that the addition of the CD8 α/β domain to the OT1scTCR fusion has a greater impact on pMHCI binding than creation of the bivalent OT1scTCR molecule.

3.3.3 Creation of Functional Two-Chain Heterodimers

As indicated above, the N-termini of the hIL-15 and hIL-15Rα domains are at distal ends of the complex raising questions as to whether this scaffold is suitable for fusions to polypeptides of a multi-chain

protein. To determine whether a soluble, biologically active, heterodimeric TCR α/β could be constructed using the hIL-15 and hIL-15RαSu scaffold, the C-terminal ends of the extracellular OT1 TCR Vα-Cα and Vβ-Cβ domains were linked to the N-termini of hIL-15 and hIL-15RαSu/birA chains, respectively. Based on the published α/β TCR crystal structures, the TCR Cα and Cβ C-terminal amino acids of the properly folded OT1 TCR α/β molecule are expected to be ~18 Å apart (71). The OT1 TCRα/hIL-15 and OT1 TCRβ/hIL-15RαSu/birA fusion genes were cloned into two separate expression vectors and co-transfected into CHO cells to generate a heterodimeric TCR α/β complex (Figure 3.1B). The secreted fusion protein complex was purified using anti-TCR Cβ mAb affinity chromatography as described above. When analyzed by SDS-PAGE under reducing condition, the purified protein bands migrated at 50-60 kDa, consistent with the calculated monomeric MW (40 kDa) of each of the two fusion molecules (Figure 3.1C. lane 8). The purified protein was further characterized in the functional ELISA (anti-TCR Cβ mAb capture: OVA peptide/H2-K^b tetramer probe). As shown in Figure 3.5A, the purified protein was found to have equivalent pMHCI binding activity as OT1 TCR in the single-chain format. Similar results were observed for hIL-15:hIL-15RαSu/birA fusions to the Vα-Cα and Vβ-Cβ chains of the p53-specific 264 TCR (Figure 3.5B). Previous attempts to produce soluble α/β TCR heterodimers in mammalian cells have been largely unsuccessful (72, 73). Thus, our results suggest that the TCR α and β chains were appropriately folded through the association of the hIL-15 and hIL-15RαSu/birA domains within the transfected cells. Intriguingly, the fusion to N-termini of the hIL-15:hIL-15RαSu scaffold is able to provide the spatial arrangement sufficient for functionally independent binding domains as observed with the c264scTCR/c149scTCR heterodimeric complex while retaining flexibility to permit folding of closely paired chains such as the α and β chains of OT1 TCR and 264 TCR.

3.3.4 Biological Activity of the hIL-15 Domain for the hIL-15:hIL-15RαSu Fusion Complexes

The IL-15 receptor (IL-15Rβγ_C) binding capability of the hIL-15:hIL-15Rα domain of the c264scTCR dimer was evaluated by flow cytometry analysis using 32Dβ cells which carry the hIL-15Rβ and the murine γ_C (mγ_C) chains. These studies were carried out using c264scTCR dimers containing the wild-type hIL-15 domain, as well as dimers with hIL-15 mutein domains previously shown to enhance (N72D) or reduce (D8N) binding to the hIL-15Rβ chain without affecting formation of the hIL-15:hIL-15RαSu complex (56). Following incubation with the c264scTCR dimers, the 32Dβ cells were stained with anti-TCR mAb to detect cell-bound fusion protein dimers. As shown in Figure 3.6A, the 32Dβ cells were stained positively by the c264scTCR dimers containing hIL-15 wild-type or hIL-15N72D domains but not with those containing the hIL-15D8N domain, indicating that the IL-15:hIL-15RαSu portion of the complex retains the expected IL-15Rβγ_C binding activity.

The hIL-15 biological activity of the fusion protein dimers were also examined in cell proliferation assays using 32Dβ cells. As shown in Figure 3.6B, the hIL-15 wild-type domain in the scTCR/hIL-15 fusion or scTCR/hIL-15:scTCR/hIL-15RαSu fusion complex was able to support the growth of 32Dβ cells in a concentration-dependent manner, exhibiting half-maximal stimulation (EC_{50}) at ~300 pM. The hIL-15N72D or D8N domains either increased or eliminated the biological activity of the fusion proteins, respectively, regardless whether they were present in the monomeric or dimeric fusions. These results are consistent with the functional activity observed for non-fusion IL-15 cytokine carrying the N72D or D8N mutations (56). Thus, formation of the fusion protein complex containing two independent TCR domains does not significantly change the biological activity of the IL-15 domain. In contrast, there was at least a 3 fold loss of IL-15 activity for the OT1 TCRα/β heterodimer complex (data not shown), suggesting formation of the heterodimeric TCR structure inhibits, to some extent, the ability of the hIL-15 domain to interact with hIL-15Rβmγ_C. Additionally, these results indicate that the hIL-15 domain can be readily manipulated to allow enhanced or reduced receptor binding and functional

activity, thus providing additional flexibility for the use of the hIL-15:hIL-15RαSu scaffold in different applications.

3.4 DISCUSSION

In these studies, we demonstrate the potential uses of a hIL-15:hIL-15RαSu-based scaffold to create novel, dimeric targeting molecules. The dimeric fusion protein complexes retained immunostimulatory effects and binding activity of their hIL-15 domains and target-specific recognition domains, respectively. These results indicate that the addition of hIL-15 and hIL-15Rα did not significantly alter the spatial arrangement of the fusion domains and provided an adequate degree of conformational flexibility without eliminating cytokine activity. Thus, this scaffold could be used to form multivalent fusion complexes, such as the c264scTCR dimer, to increase the overall binding affinity of molecules, or bispecific molecules, such as the c264scTCR/c149scTCR heterodimer. In all cases, the soluble fusion proteins were produced at relatively high levels in recombinant CHO cell culture (up to 8 mgs per liter purified from cell culture supernatant without extensive cell line screening or process optimization) and could be readily purified from the cell culture supernatants. We also demonstrated that the utility of the hIL-15:hIL-15RαSu-based scaffold could be expanded to create soluble, biologically active, two-chain molecules, such as α/β TCR heterodimers, by fusing the extracellular domains of the two polypeptide chains to the N-termini of hIL-15 and hIL-15RαSu. This format resulted in a moderate decrease in hIL-15 activity, possibly due to steric hindrance between the interfolded TCR α/β chains (fused at distal ends of the hIL-15:hIL-15RαSu complex) and the hIL-15Rβγ_C binding site located in the middle of the complex. We are currently assessing the activity of additional heterodimeric complexes and different linker formats to further optimize the biological activity of these fusions.

We have previously shown in xenograft tumor models that tumor antigen specific scTCR-IgG dimers exhibit potent antitumor activity via IgG effector activity (53). The results presented here indicate that the hIL-15:hIL-15RαSu scaffold could be exploited much like the IgG scaffold to generate multivalent or multispecific targeted therapeutics. With its potent activity for stimulating proliferation and activation of effector NK and $CD8^+$ memory T cells, the hIL-15 domain expands the scope of immunotherapeutic mechanisms beyond antibody-dependent cellular cytotoxicity and complement activation associated with IgG-based approaches. Based on its immunostimulatory activity, IL-15 has been recently viewed as the most promising anti-cancer candidate among twelve immunotherapy drugs (74). Moreover, disease-targeting approaches, such as those using Ab or TCR recognition domains, could further enhance IL-15's therapeutic potential while limiting systemic toxicities. Indeed, it has been shown that a fusion protein composed of IL-15 linked to an anti-fibronectin single-chain Ab exhibits targeted, CD8 T cell-mediated antitumor activity against both subcutaneous and metastatic tumors in immunocompetent murine models (75).

Employing approaches similar to those previously used to manipulate the IgG Fc domain activity, we have also found that the IL-15 domain can be mutated to increase or decrease its functional activity. We have shown that hIL-15:hIL-15RαSu fusion molecule containing an N72D mutation in the IL-15 domain exhibit a 3-4 fold increase in biological activity, whereas IL-15 D8N mutation exhibit little or no activity (56). While IL-15 superagonist-based fusion proteins could serve as targeted immunotherapeutics for cancer and infectious diseases, an IL-15 antagonist capable of inhibiting IL-15 responsive cells at the disease site may have therapeutic potential in treating allograft rejection and inflammatory autoimmune diseases, particularly if memory CD8 T cells play a role in disease pathology (51). A non-targeted IL-15 mutant/Fcγ2a antagonist protein has already been shown to be effective at inhibiting islet and cardiac allograft rejection and preventing development and progression of arthritis in

experimental animal models (76, 77). We are investigating similar approaches with IL-15 antagonist domains in the context of the hIL-15:hIL-15RαSu fusion proteins. In addition, under certain circumstances, it may desirable to have a functionally inert scaffold for generation of multimeric molecules. For example, we have found that scTCR/hIL-15:scTCR/hIL-15RαSu fusions containing an IL-15 D8N mutation, which eliminates interactions with IL-15Rβγ, provide better TCR antigen-specific staining of cells displaying IL-15 receptor complex.

Additionally, we demonstrate that the hIL-15:hIL-15RαSu scaffold could be used to create heterodimer comprising CD8 α/β and TCR domains capable of binding the same pMHCI complex but at a spatially distinct sites. Previous studies using soluble pMHCI reagents have determined that CD8 stabilizes and enhances TCR:pMHCI interactions at the cell surface through effects on both the off-rate and the on-rate (70, 78, 79). However, several binding studies using soluble purified CD8 α/β, TCR and pMHCI proteins have shown that TCR:pMHCI interactions are not affected by the presence or absence of CD8, suggesting no cooperative binding effects (70, 80). The results of our cell-based and SPR binding studies with the OT1scTCR/scCD8 heterodimer are in contrast with these earlier reports in showing that TCR and CD8 domains displayed on the same soluble molecule exhibited much better peptide/MHC binding activity than was observed with molecules carrying monovalent or divalent TCR domains. This effect is reflected in a faster on-rate of the pMHCI:OT1scTCR/scCD8 heterodimer complex, consistent with the observations for pMHCI binding to CD8 and TCR molecules on T cells (79). Thus, the OT1scTCR/scCD8 heterodimer mimics binding of the OT1 TCR on T cells, which exhibits a strong dependence of CD8 coreceptor activity for pMHC interactions. These results indicate that the scTCR/scCD8 heterodimer and variants of this molecule could serve as very useful tools for further dissecting molecular interactions between the tertiary TCR:pMHCI:CD8 complex in a cell-free system.

The results of our SPR experiments on the OT1scTCR fusions differ from those reported by Alam et al. where the binding affinity of monovalent OT1 TCRα/β heterodimer to immobilized OVA peptide/H-2K^b complex was shown to be approximately 6 μM (81). In our studies, we were unable to detect OVA peptide/H-2K^b-binding of the OT1scTCR/birA monomer and the OT1scTCR dimer exhibited an apparent KD of 30 μM. It is possible that the OT1 TCR exhibited decreased binding activity when formatted as a single-chain Vα-linker-Vβ-Cβ molecule. However, we observed equivalent activity when comparing OT1scTCR/birA and a two-chain construct. Moreover, previous studies have shown that OVA peptide/H-2K^b tetramers with K^b mutations that abrogate CD8 binding exhibit little or no specific binding activity to OT1 TCR-bearing cells whereas tetramers without these mutations brightly stain OT1 TCR cells. These results are consistent with the very low binding affinity between OT1 TCR and its cognate pMHCI and the CD8 dependence effects on these interactions observed in our studies.

Although we have focused on TCRs and CD8 molecules as target recognition domains for demonstration purposes in this study, it is conceivable that the hIL-15:hIL-15RαSu scaffold could be used to construct other novel binding molecules with protein domains derived from Abs, adhesion molecules, or other receptors. It may also be possible to create protein domain fusions to the C-termini of the hIL-15 and hIL-15RαSu which, based on the crystal structure, are accessible for modification. The resulting molecules could contain up to four different target-recognition capabilities. With the appropriate fusion partners, these types of molecules could promote the conjugation of immune effectors cells and target cells and achieve effective killing of target cells. As noted above, the IL-15 domain of the complex could further augment these processes by providing immunostimulatory activity to support effector cell proliferation and cytotoxicity. Currently, we have constructed a variety of multi-functional molecules based on this concept and are in the process of characterizing them as anti-cancer and anti-viral immunotherapeutic agents.

Previously, the poor expression level in standard mammalian cell system limited the development of recombinant hIL-15 as a therapeutic (82). In this study, we found that expression of scTCR/hIL-15:scTCR/hIL-15RαSu complexes is at levels capable of supporting clinical development and potentially product commercialization. In addition, it has been shown that the IL-15Rα chain enhances the *in vivo* activity of hIL-15, possibly by improving the pharmacokinetics of the cytokine (83-86). These two characteristics of hIL-15:hIL-15RαSu complexes, in combination with its multivalent nature and/or multispecific targeting design, may provide an opportunity to capture the full potential of hIL-15 as an immunotherapeutic agent against cancer and viral infections.

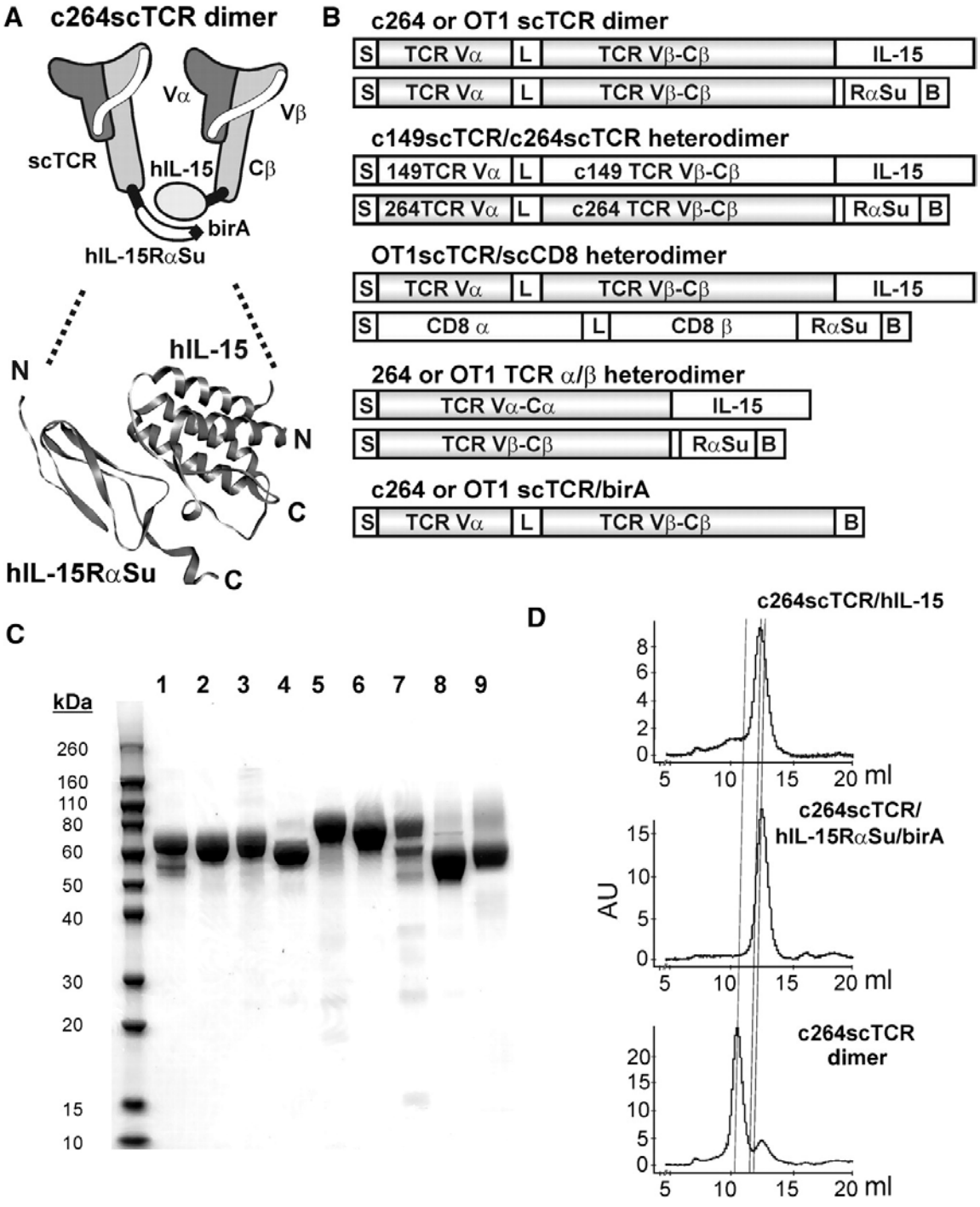
A
c264scTCR dimer
Vα
Vβ
scTCR
hIL-15
Cβ
birA
hIL-15RαSu
N
hIL-15
N
C
hIL-15RαSu
C
B
c264 or OT1 scTCR dimer
S
TCR Vα
L
TCR Vβ-Cβ
IL-15
S
TCR Vα
L
TCR Vβ-Cβ
RαSu
B
c149scTCR/c264scTCR heterodimer
S
149TCR Vα
L
c149 TCR Vβ-Cβ
IL-15
S
264TCR Vα
L
c264 TCR Vβ-Cβ
RαSu
B
OT1scTCR/scCD8 heterodimer
S
TCR Vα
L
TCR Vβ-Cβ
IL-15
S
CD8 α
L
CD8 β
RαSu
B
264 or OT1 TCR α/β heterodimer
S
TCR Vα-Cα
IL-15
S
TCR Vβ-Cβ
RαSu
B
c264 or OT1 scTCR/birA
S
TCR Vα
L
TCR Vβ-Cβ
B
C
kDa
1 2 3 4 5 6 7 8 9
260
160
110
80
60
50
40
30
20
15
10
D
c264scTCR/hIL-15
8
6
4
2
0
5 10 15 20 ml
c264scTCR/
hIL-15RαSu/birA
AU
15
10
5
0
5 10 15 20 ml
c264scTCR
dimer
20
15
10
5
0
5 10 15 20 ml

Figure 3.1. Schematic diagrams and characterization of dimer constructs. A) Schematic diagram of the c264scTCR/hIL-15:c264scTCR/hIL-15RαSu/birA complex (c264scTCR dimer). The model of the dimeric hIL-15:hIL-15RαSu domains is based on the published crystal structure of the human IL-15:IL-15Rα complex (65) (PDB 2Z3Q). B) Schematic diagram of the hIL-15:hIL-15Rα fusion protein constructs described in this study: S, signal peptide; L, peptide linker; B, linker-birA tag sequence. Linker sequences between the protein domains of the fusion proteins are provided in Supplemental Table 3-S. C) SDS-PAGE analysis of purified hIL-15 and hIL-15Rα fusion proteins under reducing conditions. Lanes: 1) c264scTCR/hIL-15, 2) c264scTCR/hIL-15N72D, 3) c264scTCR/hIL-15D8N, 4) c264scTCR/hIL-15RαSu/birA, 5) OT1scTCR/hIL-15D8N, 6) OT1scTCR/hIL-15RαSu/birA, 7) OT1scTCR/hIL-15D8N:scCD8αβ/hIL-15RαSu/birA complex, 8) OT1 TCRα/hIL-15:OT1TCRβ/hIL-15RαSu/birA complex, and 9) OT1scTCR/birA. D) SEC analysis of c264scTCR fusion proteins. Panels show comparative analysis of c264scTCR/hIL-15 (top), c264scTCR/hIL-5RαSu/birA (middle) and c264scTCR/hIL-15:c264scTCR/hIL-15RαSu/birA complex (c264scTCR dimer) (bottom) with dashed lines indicating relative protein peaks.

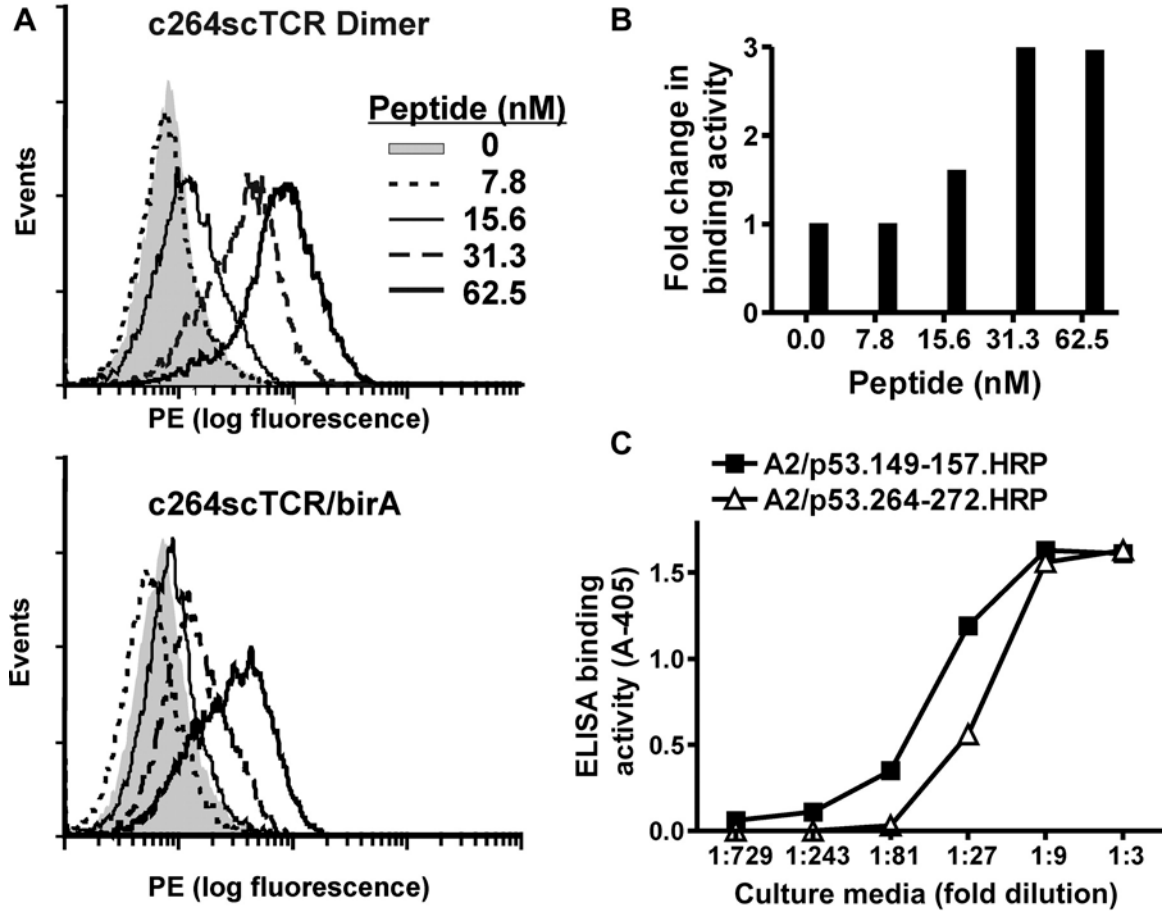
A
c264scTCR Dimer
Peptide (nM)
0
7.8
15.6
31.3
62.5
Events
PE (log fluorescence)
c264scTCR/birA
Events
PE (log fluorescence)
B
Fold change in binding activity
0
1
2
3
0.0
7.8
15.6
31.3
62.5
Peptide (nM)
C
A2/p53.149-157.HRP
A2/p53.264-272.HRP
ELISA binding activity (A-405)
0.0
0.5
1.0
1.5
1:729
1:243
1:81
1:27
1:9
1:3
Culture media (fold dilution)

Figure 3.2. Characterization of c264scTCR dimer and c264scTCR/c149scTCR heterodimer binding activity. A) T2 cells were pulsed with 0-62.5 nM of p53 (aa264-272) peptide as described in the Material and methods. The cells were stained with equivalent amounts (80 nM) of PE-conjugated multimers of the c264scTCR dimer or c264scTCR/birA. B) The relative increase in cell staining comparing c264scTCR dimer with c264scTCR/birA reagents was determined at different peptide concentrations. Fold increase = (Geo mean of T2 cells stained by c264scTCR dimer) / (Geo Mean of T2 cells stained by c264scTCR/birA). C) The p53 peptide/HLA-A*0201 binding activity of c264scTCR/c149scTCR heterodimer was determined by ELISA. Anti-hIL-15 mAb was used as a capturing reagent. A2/p53.264-272.HRP (open triangles) or A2/p53.149-157.HRP (closed squares) tetramers were used as the probes. The data represent the means ± SD of triplicate determinations. The results are representative of at least two independent assays.

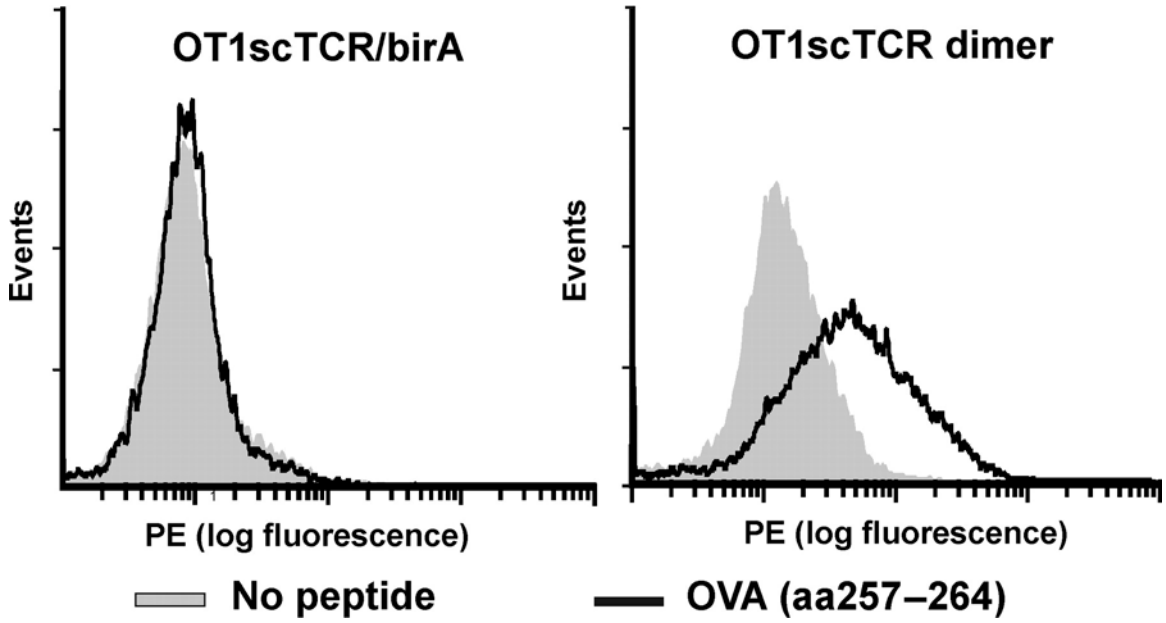

Figure 3.3. Characterization of OT1scTCR dimer binding activity. EL4 cells were loaded with OVA (aa257-264) peptide and stained with OT1scTCR/birA-SA-PE (left) and OT1scTCR dimer-SA-PE (right) at 200 nM.

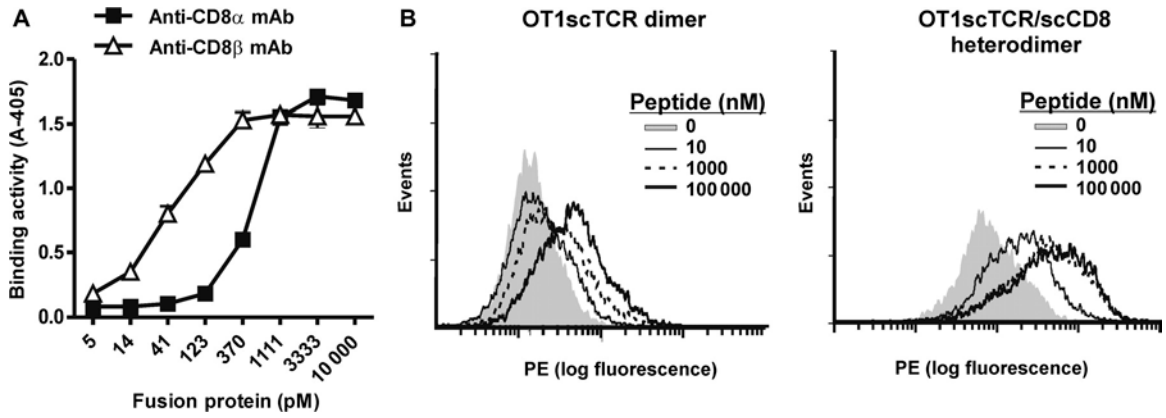

Figure 3.4. OTscTCR/scCD8 heterodimer exhibits enhanced pMHCI binding activity. A) Murine CD8 expression of OT1scTCR/scCD8 heterodimer was determined by ELISA. Anti-mTCR H57-597 mAb was used as a capturing reagent. The biotinylated anti-murine CD8α (closed squares) or CD8β (open triangles) mAb was used as a probe followed by SA-HRP. The data represent the means ± SD of triplicate determinations. The results are representative of at least two independent assays. B) EL4 cells were loaded with OVA (aa257-264) peptide at the indicated concentration and stained with OT1scTCR dimer-SA-PE (left) and OT1scTCR/scCD8 heterodimer-SA-PE (right) at 200 nM.

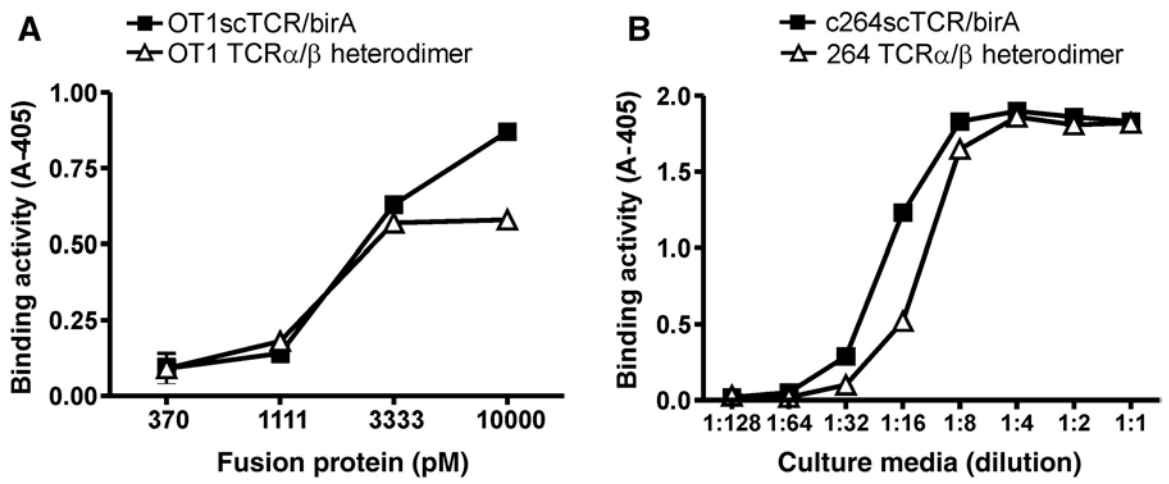

Figure 3.5. Fusion proteins containing TCR α/β heterodimers retain pMHCI binding activity. A) Binding activity of OT1scTCR/birA (closed squares) and OT1 TCRα/β heterodimer (open triangles) to OVA (aa257-264)/H-2K^b complex was determined by ELISA. Anti-mTCR H57-597 mAb was used as a capturing reagent. K^b/OVA.257-264.HRP tetramer was used as a probe. B) Binding activity of 264scTCR/birA (closed squares) and 264 TCRα/β heterodimer (open triangles) to p53 (aa264-272)/HLA-A*0201 complex was determined by ELISA. Anti-TCR mAb was used as a capturing reagent. A2/p53.264-272.HRP tetramer was used as a probe. The data represent the means ± SD of triplicate determinations. The results are representative of at least two independent assays.

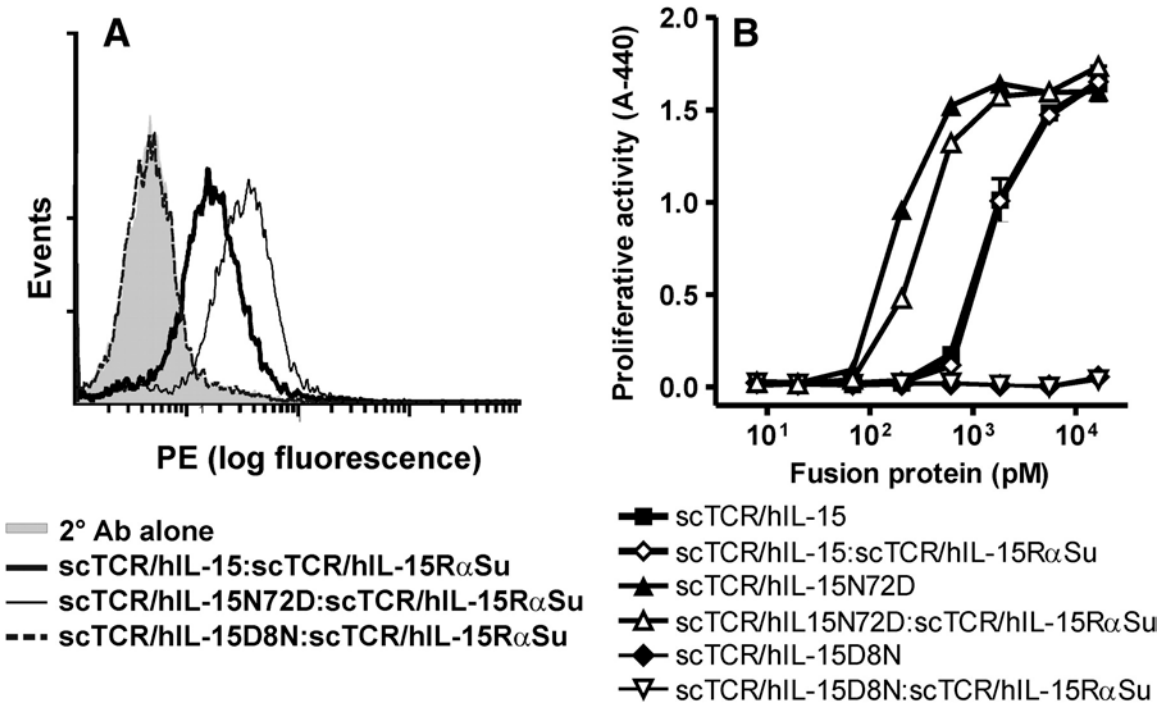

Figure 3.6. IL-15 binding and functional activity of fusion proteins. A) 32Dβ cells were incubated with 320 nM of the c264scTCR dimers comprising IL-15 wild type or IL-15N72D or IL-15D8N mutein domains. The binding of the fusion proteins was in turn detected with anti-human TCR Cβ Ab. B) The ability of the c264scTCR dimers comprising IL-15 wild type or mutein domains to support proliferation of 32Dβ cells was determined as described in the Material and methods. The data represent the means ± range of duplicate determinations.

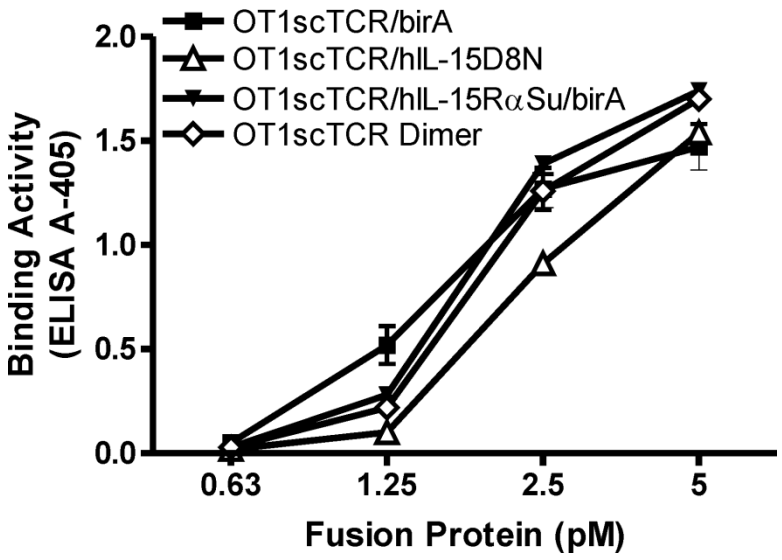

Supplemental Figure 3.1. OVA (aa257-264)/H-2Kb binding activity of OT1scTCR/hIL-15D8N, OT1scTCR/hIL-15RαSu/birA and OT1scTCR dimer determined by ELISA. Anti-mTCR H57-597 mAb was used as capturing antibody. Kb/OVA.257-264.HRP tetramer was used as a probe. The data represent the means ± SD of triplicate determinations.

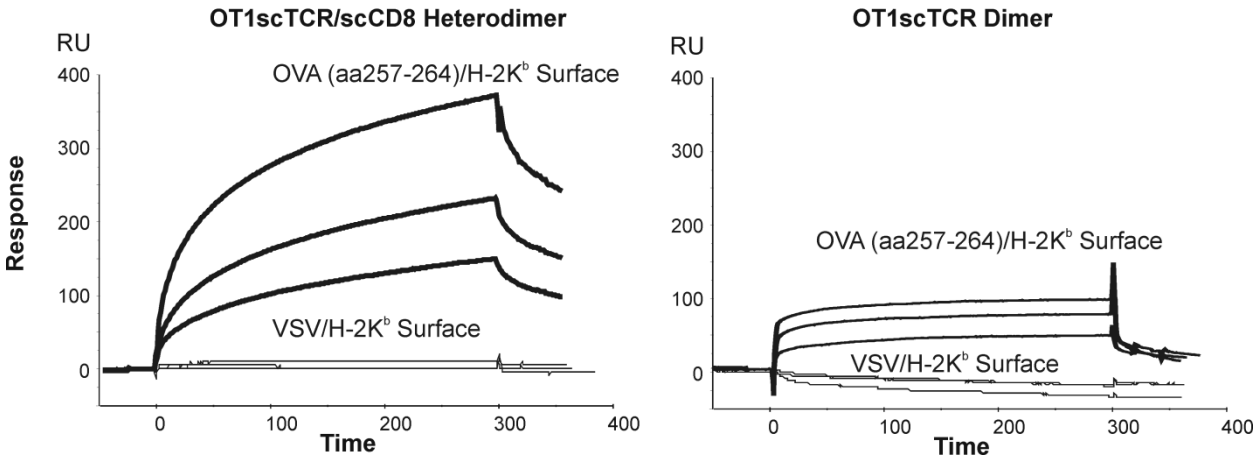

Supplemental Figure 3.2. OT1scTCR fusion protein binding curves determined by SPR.

Table 3.1. OT1scTCR fusion protein binding kinetic and affinity values determined by SPR.

Analyte	Immobilized Ligand	k_{on} ($M^{-1}s^{-1}$)	k_{off} (s^{-1})	K_D (μM)
OT1scTCR/birA (monomer)	OVA-(257-264)/H-2K[b]	No binding		
OT1scTCR dimer	OVA-(257-264)/H-2K[b]	8.9×10^{2}	0.029	32
OT1scTCR dimer	VSV/H-2K[b]	No binding		
OT1scTCR/scCD8 heterodimer	OVA-(257-264)/H-2K[b]	1.0×10^{4}	0.027	2.6
OT1scTCR/scCD8 heterodimer	VSV/H-2K[b]	No binding		

Supplemental Table 3.1. Protein domain linker sequences.

Linker	Linker Sequences	Fusion Protein
Single-chain TCR linker	TCR Vα - DTSGGGGSGGGGSGGGGSGGGGSSS - TCR Vβ	c264scTCR/hIL-15N72D c264scTCR/hIL-15RαSu/birA
	TCR Vα- TSGGGGSGGGGSPGGGGSGGGGSSS - TCR Vβ	c149scTCR/hIL15N72D
	TCR Vα- DTSGGGGSGGGASGGGGSGGGGSSS - TCR Vβ	OT1scTCR/birA
	TCR Vα- SGGGGSGGGASGGGGSGGGGS - TCR Vβ	OT1scTCR/hIL-15D8N OT1scTCR/hIL-15RαSu/birA
Mutated human IgG1 hinge	TCR domain - VNEPKSSDKTHTSPPSPTR - hIL-15RαSu	c264scTCR/hIL-15RαSu/birA OT1scTCR/hIL-15RαSu/birA OT1TCRβ/hIL-15RαSu/birA 264TCRβ/hIL-15RαSu/birA
	TCR domain - VNEPKSSDKTHTSPPSPTR - hIL-15	264TCRα/hIL-15D8N OT1TCRα/hIL-15 OT1scTCR/hIL-15D8N
BirA linker	hIL-15RαSu - SGGGSGGGGSID - birA tag	c264scTCR/hIL-15RαSu/birA OT1TCRβ/hIL-15RαSu/birA scCD8αβ/hIL-15RαSu/birA
Single-chain CD8 linker	CD8α - SGGGGSGGGGSGGGGSGGGGS - CD8β	scCD8 αβ /hIL-15RαSu/birA

CHAPTER 4 – TARGETED NANOPARTICLES FOR CANCER DIAGNOSTICS

Includes material previously presented in: Wong R, Wang Y. International Society of Magnetic Resonance in Medicine 2010 – Stockholm, SE - Creation of a Multimeric Anti-P53 ScTCR-SPIO Conjugate for the Detection of Cancer in MR, Poster Presentation

4.1 INTRODUCTION

The concept of targeted contrast agents can be readily adapted for use in other applications, such as for the specific and selective detection of cancer using MRI. Common implementations of this targeted approach have used targeting proteins specific to biomarkers overexpressed on the surface of certain cancer cells, including the antibody trastuzumab for the detection of ErbB2 expressing breast cancers (87) (88) (89), the antibody rituximab for the detection of CD20 expressing lymphomas(90) (91), and Anti-Epideral Growth Factor Receptors (EGFR) for the detection of high-grade astrocytic gliomas (92) (93). These targeting proteins are then conjugated to common contrast agents, such as superparamagnetic iron oxide (SPIOs) nanoparticles or Gd-based constructions for use as MR contrast agents.

A key aspect in creating such a molecule is selecting an ideal biomarker target for detection. As with targeting proteins such as trastuzumab, rituximab, and EGFRs, most commonly used ligands are specific only to a very limited subset of cancers. In many circumstances where generalized detection is more desirable, a biomarker such as tumor suppressor protein p53 would be ideal. p53 is an intracellular tumor suppressor protein acts to arrest abnormal cells in the G1/S phase of the cell cycle. When p53 is mutated, it loses its function as a tumor suppressor, thus allowing abnormal cells to continue to proliferate. The p53 protein is one of the most important factors that protects humans from developing cancer and is also one of the most frequently mutated genes in most major forms of human cancers (94, 95). Moreover, for any given cancer type, p53 dysfunction generally correlates with poor treatment and poor prognosis. For instance, overexpression of p53 in breast cancer cells has been correlated with aggressiveness of the tumor such that individuals bearing p53-overexpressing tumors have shorter disease-free time and lower overall survival rates (96, 97). In some tumors, p53 mutation/overexpression also is associated with resistance to chemotherapeutic intervention (98).

Recently, it has been shown that p53 also modulates the balance between the utilization of respiratory and glycolytic pathways in cells and that the inactivation of p53 in cancer cells leads to preferential use of glycolysis for energy generation (99). This metabolic change is one of the alterations in cancer cells believed to provide these cells with a survival advantage. Mutated p53 has been shown to have a longer half-life than the wild type protein, and this longer half-life allows for accumulation and thus, overexpression. However, p53 cannot be used as a target for antibody-based approaches because it is not displayed independently on the cell surface. Instead the p53 gene product is processed and certain peptide epitopes are displayed on the cell surface in the context of HLA molecules, which are recognized by the T-Cell Receptors TCRs) of T-cells. As a result, we are investigating the use of soluble TCRs rather than antibodies in targeting p53 for this application.

Previously, we isolated a T-cell receptor from a p53 (aa 264-272)-specific high avidity CTL clone derived from HLA-A*0201 transgenic mice (sc264TCR). The epitope is within a region that is rarely mutated, making it a broad-based target for HLA-A*0201^{+} tumors. From this TCR, a three-domain single-chain format of the TCR (scTCR) was constructed and designated c264scTCR. This molecule can be produced by mammalian cell fermentation and purified by immunoaffinity chromatography as a soluble, single-chain, biologically-active protein which retains the ability to specifically recognize the p53 antigen (aa 264-272)/HLA-A*0201 complex (53, 61, 64). We further increased the affinity of c264scTCR by producing a dimeric variant of c264scTCR based on a novel IL-15/IL-15Rα scaffold to create soluble homodimers with increased functional binding affinity toward target antigens.(33) IL-15 is a member of the small four α-helix bundle family of cytokines that associates with the IL-15 receptor α-chain and is then trans-presented to IL-15Rβ γC complexes displayed on the surface of T cells and NK cells. This cytokine/receptor interaction results in expansion and activation of effector T cells and NK cells, which play an important role in eradicating virally infected and malignant cells. Importantly, IL-15 binds to the

IL-15Rα chain with exceptional binding affinity (Ka value of ~$10^{-11}M^{-1}$). Moreover, IL-15 and IL-15Rα are co-produced in dendritic cells to form complexes intracellularly that are subsequently secreted and displayed as heterodimeric molecules on cell surfaces. These two characteristics of IL-15 and IL-15Ra interactions suggest that these inter-chain binding domains could serve as a novel, human-derived immunostimulatory scaffold to make soluble dimeric molecules capable of target-specific binding. This increase of affinity through an increase in avidity is similarly attractive in the construction of MR contrast agents, whereby contrast agents with high affinity to tumorous cells could translate to greatly improved imaging sensitivity and vastly improved clinical diagnostic accuracy.

In this study, we created a high affinity dimeric c264scTCR-coated super paramagnetic iron oxide (SPIO) conjugate capable of specific contrast agent delivery to p53-expressing cells. By selectively delivering SPIO nanoparticles to p53-expressing cells and probing their presence using quantitative MRI quantitative susceptibility mapping (QSM) techniques, were able to measure specific scTCR-SPIO conjugate adhesion in *in vitro* conditions to various cancer cell lines known to express cell-surface p53 in the context of HLA. The results of this study suggest future applicability for p53-specific SPIO nanoparticles for use as targeted generalized cancer contrast agents.

4.2 METHODS AND MATERIALS

4.2.1 Creating Multimeric scTCRs

Generation of a soluble monomeric single-chain (sc) three-domain TCR construct, c264scTCR, has been described previously.(59) This protein recognizes the human p53 peptide (aa264-272) presented in the context of HLA-A*0201. Fusions between the c26t4scTCR domain and human IL-15 (hIL15) or the sushi domain of human IL-15Ra (aa1-66 of hIL-15Ra; hIL-15RaSU) linked via a mutated human IgG1 hinge region were generated as described previously.(56) Dimeric c264scTCR fusion protein complexes

(referred to as c264scTCR dimer) were constructed by mixing equal moral amounts of purified c264scTCR/hIL-15 and c264scTCR/hIL-15Rasu/birA fusion proteins and were allowed to associate at room temperature for 1 hour. Proteins were biotinylated with biotin ligase followed by complexing with streptavidin-phycoerythrin (SA-PE) to generate multimeric flow cytometry staining reagents, or with streptavidin-coated super paramagnetic iron oxide (SA-SPIO) nanoparticles (50nm diameter, Ocean Nanotech) to generate multimeric contrast agents suitable for use in MRI.

4.2.2 scTCR Specificity Assay (Flow Cytometry)

scTCR specificity against p53-expressing cells was characterized using flow cytometry. Subconfluent A37545N human melanoma tumor cells (ATCC, Manassas, VA), and T2 human lymphoblast cells (ATCC, Manassas, VA) pulsed with 50µM p53 (aa264-272) peptide at 37°C for 2 h in the presence of peptide loading enhancer (PLE, Altor BioScience Corp., Miramar, FL), were stained with 80nM monomeric or dimeric scTCRs or with non-specific Mart1TCR labeled with Phycoerythrin, and incubated at 4°C for 1 h. The samples were washed two times with 0.5% BSA-PBS and analyzed on a FACScan flow cytometer using CellQuest software (BD Biosciences, San Jose, CA). Staining curves were obtained at FL-2, 575nm.

4.2.3 scTCR-Conjugate Formation and Validation

scTCR-SPIO conjugates were constructed through interaction between streptavidin-coated SPIO nanoparticles and biotinylated monomeric or dimeric scTCRs. 20ug of 0.3 µM iron oxide nanoparticles, 50 nm in diameter with a streptavidin surface (Ocean Nanotech, Fayetteville, AR), were incubated with 3 uM biotinylated monomeric 264scTCR or dimeric 264scTCR at a 1:20 nanoparticle:TCR molar ratio at 4°C for 1 hour. Conjugates were purified using a MiniMACS magnetic cell separation column (Mitenyi) and washed twice with PBS. Conjugate formation was validated through ELISA. scTCR-SPIO conjugates were

captured using BF1 mAb coated plates, specific to the β1 constant region of the scTCR. Streptavidin-HRP dye was linked using WF1-biotin mAb linker, specific to the β1 constant region of the scTCR, and developed with ABTS. Absorbance was read at 405nm using a 96-well plate reader.

4.2.4 Quantitative MR Imaging

A37545N cells, T2 cells pulsed with p53 peptide, and unpulsed T2 cells were incubated with 20ug 0.3 μM scTCR-SPIO conjugates constructed from monomeric or dimeric c264scTCRs. After two hours of incubation, cells were washed and centrifuged into a pellet in a standard centrifuge tube. The cell apparatus was scanned using a 3T Signa GE scanner (General Electric, Milwaukee, WI) with a custom birdcage coil and using a 3D multi-echo gradient echo sequence. Imaging parameters were as follows: 5 total TEs; TEs 3.696ms, 4.196ms, 5.696ms, 11.696ms, 35.696ms; TR 40ms; flip angle 30°; matrix size 256x64x64; 500μm^3 isotropic resolution. A 3D Fourier transform was applied to the raw k-space data to reconstruct T2* weighted images. Qualitative Susceptibility Maps (QSMs) were reconstructed using the Calculation of Susceptibility through Multiple Orientation Sampling (COSMOS) technique, as described in Liu 2009. (18) In brief, each sample was scanned at three different orientations by rotating the sample about the B0 axis. Phase information was extracted from the complex MRI data to obtain a background-corrected field map. The resulting field map served as the input for a field-to-source susceptibility inverse problem. Total susceptibility was calculated for each region of interest (ROI), segmented around cell pellet identified using T2* weighted images, and was used to quantitatively determine total SPIO nanoparticle presence in each ROI. Results were calibrated against a standard developed through analysis of an image phantom with known amounts of SPIO.

4.3 RESULTS AND DISCUSSION

4.3.1 scTCR Specificity Assay

To confirm the specificity of c264scTCR monomers and dimers against cell surface p53 in the context of HLA, c2664scTCR-SAPE conjugates were created and stained against p53-expressing cells and measured using flow cytometry. Staining curves of 80nM c264scTCR/hIL15Su/birA (monomeric c264scTCR)-SAPE, 80nM c264scTCR/hIL15-c264TCRhIL15-15RaSu/birA (dimeric c264scTCR)-SAPE, and 80nM Mart1scTCR-SAPE (non-p53-specific isotype control) stained against T2 cells pulsed with 50nM p53 peptide, unpulsed T2 cells, and A37545N cells are shown in Figure 4.1A. Staining profiles for p53-pulsed T2 cells exhibited positive fluorescent staining with monomeric c264scTCR-SAPE and was further enhanced with dimeric c264scTCR-SAPE, compared to that observed from non-specific Mart1scTCR-SAPE. Unpulsed T2 controls did not demonstrate positive staining with monomeric and dimeric 264scTCR-SAPE over isotype controls. A37545N human melanoma tumor cells, a cell line known to have a low to moderate degree of p53 expression, demonstrated moderate staining with monomeric c264scTCR-SAPE conjugates, and is further enhanced with dimeric c264scTCR-SAPE.

These results confirm the specificity and selectivity of c264scTCRs against cells expressing p53. In the case of p53-pulsed T2 cells, cells artificially induced to express high levels of p53 on the cell surface in the context of HLA, dimeric c264scTCR-based conjugates exhibited a significant degree of staining, readily surpassing that of monomeric c264scTCR-based conjugates and non-specific controls. While c264scTCR-SAPE stained p53-pulsed T2 cells demonstrated by far the greatest degree of staining, c264scTCR-SAPE stained A37545N also exhibited observable amounts of positive staining. As the A37445N cell line is known to have a relatively low degree of surface-expressed p53, these results support the viability of using c264scTCR-based conjugates to specifically target tumors cell with relatively low, but still physiologically-relevant amounts of p53 surface expression. Furthermore, the increase in observable staining between the use of monomeric and dimeric c264scTCR against p53-

expressing cells demonstrates that the increased avidity of the dimeric forms contributes to quantifiably increased affinity against p53 peptide.

4.3.2 scTCR-Conjugate Formation and Validation

To validate that dimeric c264scCR-SPIO conjugates were correctly formed and subsequently isolated from unbound scTCRs through magnetic separation, we captured c264scTCR-SPIO conjugates and measured its activity through an ELISA-like assay. Dimeric c264scTCR-SPIO conjugates were created by combining c264scTCR/hIL15, c264scTCR/hIL15RaSu/birA, and SA-SPIO at a molar ratio of 1:1:10 and passed through a magnetic separation to collect magnetically susceptible SPIO-conjugated scTCRs. Collected particles were captured on BF1 antibody-coated plates, linked to biotinylated WF4 antibodies, linked to streptavidin-HRP. The relative concentration of each dimeric c264scTCR-SPIO conjugate was plotted against the optical density at 405nM after serial dilution and subsequent HRP development with ABTS (Figure 4.1B). A nonlinear concentration-dependent response was observed at optical density 405nm only with complete forms of c264scTCR/hIL15-c264TCRhIL15-15RaSu/birA-SPIO. Incomplete forms of the conjugate (SPIO only or c264scTCR/hIL15-c264TCRhIL15-15RaSu/birA only) show a no observable response, indicating an effective formation of dimeric c264scTCR-SPIO conjugates. As BF1 and WF4 antibodies bind only to each of two distinct regions of the β1-constant region of c264scTCRs, and the magnetic filtration process captures magnetic SPIOs while eliminating all unbound scTCRs, only scTCR-SPIO conjugates should be detected by this assay. The concentration-dependent nature of the results indicates that the magnetic purification process effectively removes unbound scTCRs from the preparation while preserving the scTCR-SPIO conjugates.

4.3.3 Quantitative MR Imaging

To demonstrate that monomeric and dimeric c264scTCR-SPIO conjugates can be used as a contrast agent for use in selectively delivering contrast for MRI applications, we incubated cell surface p53-expressing cells with c264scTCR-SPIO conjugates and quantified the amount of observable SPIO accumulation using MRI-based quantitative susceptibility mapping (MRI-QSM). The amount of accumulated SPIO in 1 x 10^7 A37545N cells, p53-pulsed T2 cells, or unpulsed T2 cells, each incubated with 20µg monomeric or dimeric 0.3 uM scTCR-SPIO conjugates for two hours, was measured using MRI-COSMOS (Figure 4.1C). Representative T2* weighted imagines, relative field maps, and results of the MRI-QSM COSMOS reconstruction for select samples are shown (Figure 4.2). C264scTCR-SPIO conjugates incubated with T2 cells pulsed with p53 exhibited the greatest degree of SPIO accumulation, up to 5.23 times more when dimeric c264scTCR-SPIOs were used, compared to unpulsed T2 cells incubated similarly with dimeric c264scTCR-SPIO. Moderate amounts of measureable SPIO accumulation was seen with conjugates incubated with A37545N, up to 3.27 times more when dimeric c264scTCR-SPIOs were used, compared to similarly treated unpulsed T2 cells. Minimal SPIO accumulation was observed with unpulsed T2 cells. Overall, dimeric c264scTCR-SPIO contributed to the greatest degree of SPIO, increasing SPIO accumulation by 21% and 38% over monomeric c264scTCR-SPIO for p53-pulsed T2 cells and A37545N cells, respectively. Nonspecific Mart1scTCR-SPIO binding was minimal across all cell types. Qualitatively, T2* weighted images depict negative contrast enhancement consistent with the presence of SPIO. MRI-QSM reconstructions show positive contrast. Larger, more intense voxels can be seen in p53-expressing cells treated with c264scTCR-SPIO conjugates, indicating greater and more concentrated SPIO accumulation. Field maps for each condition exhibit an increasingly large “dipole” pattern of magnetic field perturbations with p53-expressing cells treated with c264scTCR-SPIO conjugates, likewise consistent with the presence of increasingly greater amounts of SPIO accumulation.

Overall, the resulting SPIO accumulation is readily observable using both traditional T2* weighted imaging techniques and MR-QSM based techniques, allowing for a qualitative and quantitative measure of overall contrast agent delivery. The effectiveness of the dimeric form over the monomeric form of c264scTCR-SAPE conjugates for p53-specific staining under flow cytometry, and the effectiveness of the dimeric form over the monomeric form of the c264scTCR-SPIO conjugates for MR labeling under MRI-QSM, demonstrates that an increase in avidity corresponds to an increase in affinity, resulting in a greater degree of staining and a greater degree of contrast agent accumulation among p53-expressing cells in both fluorescent and MR applications. Further, MR imaging demonstrates that positive labeling can be observed even against cell lines with relatively low levels of p53 expression, and can be readily imaged and quantified using MRI-QSM techniques.

The results suggest a use for dimeric c264scTCR-SPIO contrast agents for *in vivo* applications to selectively deliver contrast agents to tumor sites to assist in cancer diagnosis. In addition, when combined with MRI-QSM analysis, c264scTCR-SPIO contrast agents can be quickly and non-invasively tracked, and accumulation can be quantifiably measured, giving direct observation of spatiotemporal information about the biodistribution of contrast agents, a task not easily obtainable with current clinical techniques. Likewise, the ability to quantitatively track contrast agents can be extended to drug delivery applications, whereby precise amounts of a specifically delivered agent can be non-invasively tracked to better monitor and refine diagnostic and therapeutic agents.

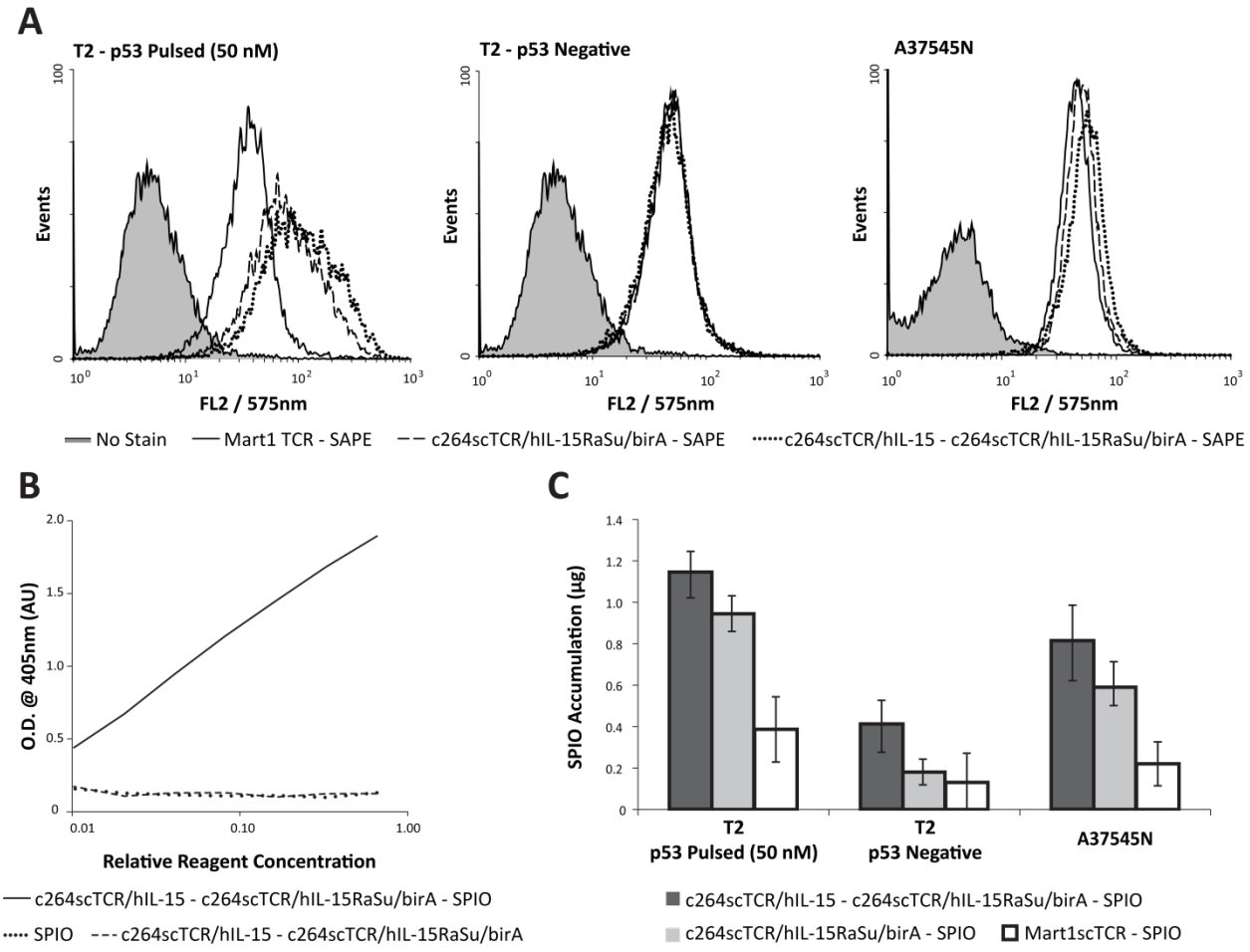
A
T2 - p53 Pulsed (50 nM)
T2 - p53 Negative
A37545N
Events
FL2 / 575nm
No Stain
Mart1 TCR - SAPE
c264scTCR/hIL-15RaSu/birA - SAPE
c264scTCR/hIL-15 - c264scTCR/hIL-15RaSu/birA - SAPE
B
O.D. @ 405nm (AU)
Relative Reagent Concentration
c264scTCR/hIL-15 - c264scTCR/hIL-15RaSu/birA - SPIO
SPIO
c264scTCR/hIL-15 - c264scTCR/hIL-15RaSu/birA
C
SPIO Accumulation (µg)
T2
p53 Pulsed (50 nM)
T2
p53 Negative
A37545N
c264scTCR/hIL-15 - c264scTCR/hIL-15RaSu/birA - SPIO
c264scTCR/hIL-15RaSu/birA - SPIO
Mart1scTCR - SPIO

Figure 4.1. Characterization of scTCR binding and scTCR-SPIO conjugate binding *in vitro.* A) *Flow Cytometry* – Staining profiles for T2 cells pulsed with p53 peptide (50nM) exhibit positive fluorescent staining with 80nM c264scTCR/hIL15Su/birA (monomeric c264scTCR)-SAPE and further enhanced staining with 80nM c264scTCR/hIL15-c264TCRhIL15-15RaSu/birA (dimeric c264scTCR)-SAPE, compared to isotype control 80nM Mart1scTCR-SAPE. Unpulsed T2 controls do not demonstrate positive staining with monomeric and dimeric 264scTCR-SAPE over isotype controls. A37545N demonstrates moderate staining with monomeric c264scTCR-SAPE, and is moderately enhanced with dimeric c264scTCR-SAPE. B) *ELISA* – scTCR-SPIO conjugates were isolated using magnetic separation and captured by BF1 antibody-coated plates, linked to biotinylated WF4 antibodies, linked to streptavidin-HRP, and developed with ABTS. Concentration-dependent response was observed at optical density 405nm only with complete forms of c264scTCR/hIL15-c264TCRhIL15-15RaSu/birA-SPIO. Incomplete forms of the conjugate (SPIO only or c264scTCR/hIL15-c264TCRhIL15-15RaSu/birA only) show a minimal response, indicating effective conjugation of scTCRs and SPIOs. C) *Quantitative MRI* – c264scTCR-SPIO conjugates incubated with T2 cells pulsed with p53 exhibited the greatest degree of SPIO accumulation, as measured by MRI-QSM. Moderate amounts of measureable SPIO accumulation was seen with conjugates incubated with A37545N, and minimal SPIO accumulation was observed with unpulsed T2 cells. Overall, dimeric c264scTCR-SPIO contributed to the greatest degree of SPIO, regardless of cell type and condition. Nonspecific Mart1scTCR-SPIO binding was minimal across all cell types. Error bars indicate a 95% confidence interval across three repeated samples.

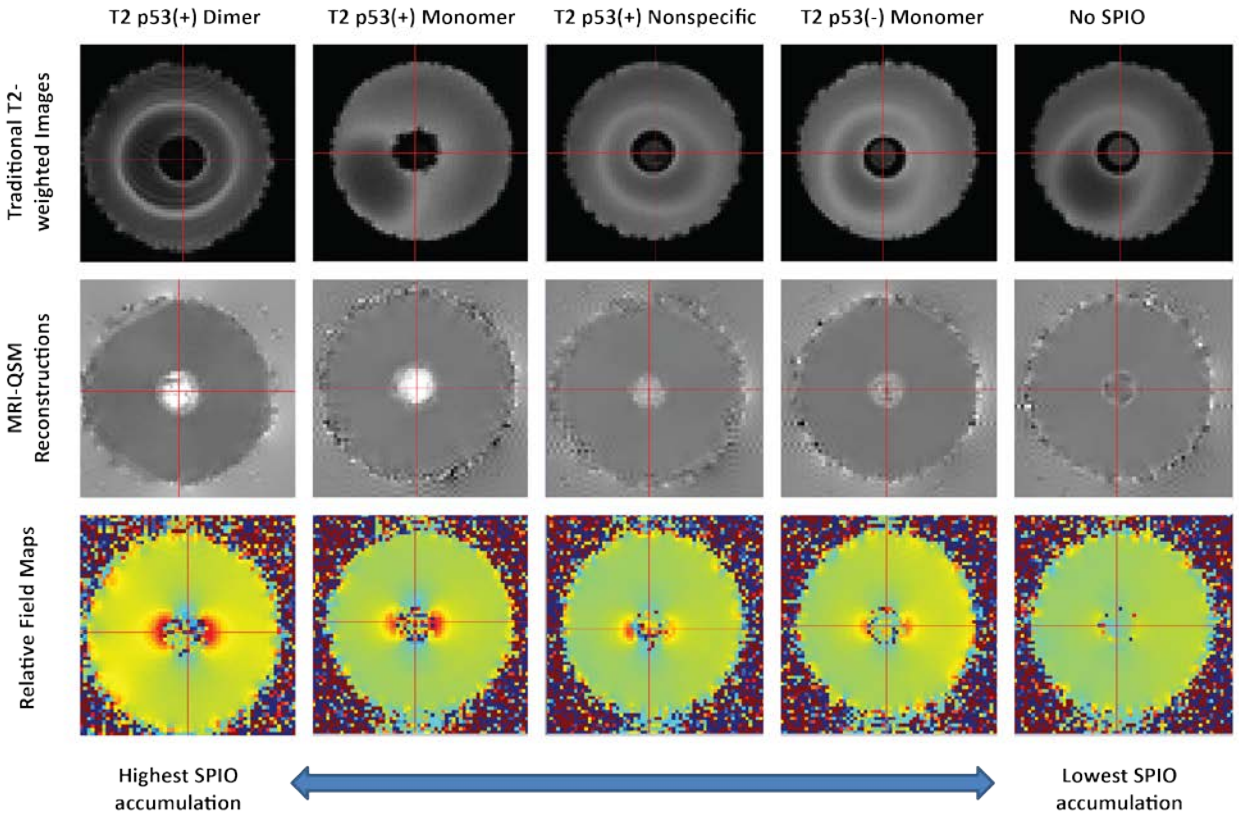

Figure 4.2. Representative MRI images from varying cell and scTCR-SPIO conditions. Traditional T2 weighted images (top) depict negative contrast with increasing SPIO accumulation. MRI-QSM reconstructions (middle) show positive contrast; larger, more intense pixels represent more concentrated SPIO accumulation. Relative field maps (bottom) exhibit an increasingly large "dipole" pattern with increasing SPIO accumulation.

CHAPTER 5 – TARGETED NANOPARTICLES TO VISUALIZE ACTIVE INFLAMMATION: PART 1

Includes material previously published in: Chen X, Wong R, Wang YA, Wang Y, Jin MM. Inflamed leukocyte-mimetic nanoparticles for molecular imaging of inflammation. *Biomaterials*. 2011 Oct;32(30):7651-7661. Epub 2011 Jul 23. (100)

5.1 INTRODUCTION

Dysregulated inflammatory responses of the host are implicated in the pathogenesis of many human diseases (101). Acute inflammation from infection can cause sepsis (102), while chronic inflammation, and continual coexistence between acute and chronic inflammation are associated with various neurodegenerative (103) and cardiovascular diseases (104), metabolic disorders (105), and cancer (106, 107). Accordingly, sensitive and early detection of inflammation and site-specific delivery of anti-inflammatory agents will have a wide-ranging impact on the treatment of various inflammation-related diseases. Upon induction of inflammation, a set of adhesion molecules are upregulated in endothelium, with which immune cells interact using counter adhesion molecules such as integrins to adhere to endothelium and to initiate diapedesis. Many existing studies have investigated targeted nanoparticles for the detection and treatment of inflammation employing antibodies or peptides specific to adhesion molecules such as intercellular adhesion molecule (ICAM)-1 (108-110), vascular cell adhesion molecule (VCAM)-1 (111-113), selectins (114), and collagen (115), all of which display distinct spatiotemporal responses to inflammation. Among these molecules, ICAM-1 has caught a particular interest because of its highly inducible and localized expression upon inflammatory signals, serving as a marker for inflammation despite its constitutive low level expression (116, 117).

In this study, we developed nanomicelle encapsulating superparamagnetic iron oxide (SPIO) nanoparticles, designed for facile and robust conjugation with targeting moieties and *in vivo* detection by optical imaging and magnetic resonance imaging (MRI). In order to design nanoparticles to mimic the behavior of inflamed leukocytes in their ability to locate to the inflamed site, SPIO nanoparticle was coated with an optimum number of high affinity inserted (I) domain of integrin called lymphocyte function-associated antigen (LFA)-1 (118), a physiological receptor for ICAM-1. Leukocyte-mimetic nanoparticles were examined for detection of ICAM-1 overexpression in tumor cells, tumor vascular

microenvironment, and acute inflammation *in vivo*. With our recently developed MRI technique for quantitative mapping of contrast agent (18, 119), we explored the possibility of quantitative spatiotemporal mapping of iron oxide distribution *in vivo* using a mouse model of acute inflammation.

5.2 MATERIALS AND METHODS

5.2.1 Preparation and characterization of protein coated SPIO nanomicelles

Oleic acid-capped super paramagnetic iron oxide (SPIO) nanocrystals (Ocean Nanotech, LLC) in 5 mg were suspended in 1 ml chloroform with 12 mg 1,2-dipalmitoyl-sn-glycero-3-phosphoethanolamine-N-[methoxy(polyethylene glycol)-2000] (DPPE-PEG) and 3 mg 1,2-dioleoyl-sn-glycero-3-[(N-(5-amino-1-carboxypentyl)iminodiacetic acid)succinyl] nickel salt (DOGS-NTA) (Avanti Polar Lipids, Inc.). For radiolabeled nanoparticles, 60 μCi of L-α-Dipalmitoyl-Phosphatidylcholine, [Choline-Methyl-3H] (Perkin Elmer) was also added at this step. After 10 min sonication and overnight desiccation, 1 ml of water was added to the residue to form a micelle layer on SPIO. After another 10 min sonication and filtration through 0.22 μm filters (Millipore), optically clear suspension containing SPIO micelles were obtained. Empty micelles without SPIO in the core were removed by ultracentrifugation. SPIO nanoparticles were purified and resuspended in pH 7.4 phosphate-buffered saline (PBS) by size exclusion S200 column (GE Healthcare). The wild-type (wt), D137A, and F265S/F292G mutants of LFA-1 I domains fused to His tag (6 histidine residues) at the N-terminal were produced as previously described (117). Conjugation of SPIO with His-tagged I domains was obtained by incubation at 4 °C overnight. Free proteins were removed by size exclusion. All fluorescently labeled SPIO nanoparticles were prepared by covalently conjugating Alexa Fluor (AF) succinimidyl esters (Invitrogen) to the I domains. Conjugation of fluorescence dyes to the proteins rather than to phospholipid was chosen due to significant fluorescence quenching between iron oxide and AF-phospholipids. The coating density of proteins on SPIO was determined from the ratio

of SPIO amount (OD_{600nm} 1 = 0.42 mg/ml) and the concentration of the proteins bound to SPIO (by Lowry's method). Specific activities of radiolabeled SPIO were measured by scintillation counter (Beckman Coulter LS6500). Dynamic light scattering (DLS, Malvern Instruments) was used to measure the average hydrodynamic size of SPIO after assembly and protein conjugation. Transmission electron microscopy (TEM; FEI Tecnai) images of SPIO were also taken before and after protein conjugation. 1% uranyl acetate was used for protein staining.

5.2.2 Cell culture

All mammalian cells used in this study were cultured in Advanced Dulbecco's modified Eagle's medium containing 10% (v/v) fetal bovine serum and 2 mM L-glutamine (Invitrogen) at 37 °C in a 5% CO_2 humidified incubator. For induction of inflammation, bEnd.3 (ATCC) cells were treated with 1 μg/ml of LPS (*E. coli.* 026:B6, Sigma) for 12 hr. HeLa and 293T cells stably expressing GFP were established using pSMPUW-miR-GFP/Puro Lentiviral Expression Vector system (Cell Biolabs).

5.2.3 Immunofluorescence flow cytometry

Cells were trypsinized and washed once with the ice-chilled labeling buffer (pH 7.4 PBS, 1% (w/v) BSA, 1 mM $MgCl_2$). 100,000 cells were incubated in 100 μl of the labeling buffer for 30 min on ice with 10 μg/ml of Alexa Fluor labeled proteins or SPIO conjugated with the same amount of proteins. For competition assay, 50 μg/ml of unlabeled proteins were included in the labeling buffer during incubation. Cells were washed twice and resuspended in 300 μl of the labeling buffer and subjected to flow cytometer (Beckman Coulter EPICS XL-MC).

5.2.4 Microscopy visualization of cell labeling in vitro

For immunofluorescence microscopy detection of protein labeling, cells were plated, washed in pH 7.4 PBS, and fixed with 4% paraformaldehyde for 15 min. After washing three times, cells were incubated with 10 μg/ml of Alexa Fluor labeled proteins in PBS/Triton (pH 7.4 PBS, 0.3% (v/v) Triton X-100, 1 mM $MgCl_2$) at room temperature for 1 hr. Cells were rinsed once with pH 7.4 PBS and twice with high salt PBS (pH 7.4 PBS, 0.4 M NaCl, 1 mM $MgCl_2$). 300 nM DAPI (4',6-diamidino-2-phenylindole, Invitrogen) in PBS was then added and incubated for 10 min for nucleus staining. Stained cells were washed and imaged with a confocal microscope (Zeiss LSM 710). For detection of SPIO labeling, HeLa cells were plated and incubated with 50 μg/ml of SPIO coated with Alexa fluor 488 conjugated proteins in culture media for 2 hr at 37 °C. Cells were washed in pH 7.4 PBS, incubated for 1 hr in serum-free medium for chasing, and imaged using confocal microscopy (Leica TCS SP2). After fluorescence imaging, cells were then prepared for Perl's Prussian blue staining for iron detection. Labeled cells were fixed with 4% paraformaldehyde, followed by incubation in a freshly prepared solution of 2% potassium ferrocyanide in 2% HCl for 20 min and counterstaining with 1% neutral red.

5.2.5 Magnetic cell labeling and quantification

Trypsinized cells were incubated for 4 hr at 37 °C in the labeling buffer (PBS, 1 mM $MgCl_2$) under constant rotating with different concentrations of radiolabeled SPIO, washed and then fixed in 4% paraformaldehyde. Cells were divided into two conditions, half of which were used for radioactivity measurement using scintillation counter (Beckman Coulter LS6500), while the remaining half for MRI scanning and QSM measurement after imbedding in 100 μl 2% agarose block. MR imaging of the magnetically labeled cells were performed on a 3T MRI scanner (Signa, GE, Milwaukee, WI). A 3D multi-echo gradient sequence was used to sample multiple TEs in one TR. Imaging parameters were as follows: TEs 3.696 ms, 4.196 ms, 5.696 ms, 11.696 ms, 35.696 ms; TR 40 ms; flip angle 30°; matrix size

256×64×64; voxel size 500 μm^3 isotropic. A 3D Fourier transform was applied to the raw k-space data to reconstruct T2* weighted images. QSM was obtained through Multiple Orientation Sampling (COSMOS) technique, as previously described (18).

5.2.6 Subcutaneous tumor model

3×10^6 human cervical cancer HeLa cells and human embryonic kidney 293T cells stably expressing GFP mixed in Matrigel (BD) were injected bilaterally into the front lower flank areas of 8-wk-old female nude mice. Mice were used for experiments 16-20 days after injection when tumor size reached about 300 mm^3. All animal experiments were conducted in compliance with the regulations defined by the Institutional Laboratory Animal Use and Care Committee of Cornell University.

5.2.7 Acute LPS-inflammation model

For subcutaneous LPS, 1 mg/ml LPS in 100 µl PBS and 100 µl PBS were injected bilaterally into the lower flank areas of 8-wk-old female BALB/c mice. For systemic LPS, 1 mg/ml LPS in 100 µl PBS were injected into 8-wk-old female BALB/c mice. Prior to imaging hair was removed to reduce background fluorescence.

5.2.8 Near-IR optical imaging of mice

Animals were anesthetized with isoflurane mixed with oxygen at 5% and maintained at 2% isoflurane during whole body imaging (Olympus, OV100). Mice were administered with SPIO coated with AF750-conjugated proteins in 150 µl PBS via retro-orbital injection. 500 and 100 µg of SPIO were used for tumor imaging and acute inflammation models, respectively. Near-IR images were taken at different

time points post-injection of SPIO. Tumor growth was detected by imaging green fluorescence. Image analysis was performed with Matlab R2007a (MathWorks).

5.2.9 MR imaging of mice with acute inflammation

For subcutaneous LPS model, prior to nanoparticle injection mice were exposed to LPS/PBS for 12 hr. At 4 hr after injection of SPIO in 150 µl PBS, mice were euthanized by intraperitoneal injection of 2.5% tribromoethanol (20 µl/g), transcardially perfused with PBS, and fixed in paraformaldehyde. Prepared mice were scanned on a 7T scanner (Bruker BioSpin, Biospec 70/30 USR) with 3D FLASH sequence. Imaging parameters were as follows: TEs (echo time) 5 ms, 6 ms, 30 ms, 35 ms; TR (repetition time) 35 ms; excitation pulse angle 15°; matrix size 150×150×100; voxel size 200 μm^3 isotropic; NEX 1. A 3D Fourier transform was applied to the raw k-space data to reconstruct the images (18). For systemic LPS model, prior to nanoparticle injection mice were exposed to LPS for 12 hr. At 1, 8, and 25 hr post-injection of SPIO coated with proteins in 150 µl PBS, mice were euthanized likewise. Prepared mice were scanned on a 3T scanner (GE Signa Excite) with 3D multi-echo EFGRE sequence (18). Imaging parameters were as follows: TEs 3.696 ms, 4.196 ms, 5.696 ms, 11.696 ms, 35.696 ms; TR 40 ms; flip angle 30°; matrix size 256×64×64; voxel size 500 µm3 isotropic. QSMs were reconstructed using the COSMOS technique, as previously described.

5.2.10 Histology

Tumor and normal tissues were collected from tumor-bearing mice before or at the end of *in vivo* imaging experiments. 10 µm frozen tissue sections were sliced, fixed in paraformaldehyde, and stained with hematoxylin and eosin (H&E) or in Perl's Prussian blue. Images of the tissue sections were acquired by scanscope (Aperio). For immunofluorescence, antibodies used include rat anti-mouse CD31 (BD,

MEC13.3) and goat anti-rat IgG labeled with AF350 (Invitrogen). Six different fields of view containing CD31 staining for each sample were counted using 25 Chalkley's random point method over an area of 0.16 mm^2 for vascularity analysis (Figure 5.3D). To quantify the level of staining, three different regions of interest (ROI) with 0.50 mm^2 area were sampled for each condition in immunofluorescence staining (Figure 5.3C) and four ROI with 0.04 mm^2 area in each Prussian blue staining (Figure 5.4F). Specific colors (blue for endothelium and Prussian blue, red for F265S/F292G) were extracted and intensities were measured using Image-Pro Plus 6.0 (Media Cybernetics) and ImageJ 1.41 (NIH).

5.2.11 Statistical analysis

Data were expressed as mean ± standard deviation of no smaller than triplicates, and analyzed for statistical significance using GraphPad Prism 5 (Graphpad Software). Linear regression was used to examine the correlation between SPIO measurements by radioactivity and QSM (Figure 5.2C). One-way ANOVA was used to compare the staining and vascularity levels between different tissues, followed by Tukey's post-hoc test to determine statistical significance (Figures 5.3C & D). Two-way ANOVA was used to compare the mean responses of different nanoparticles to different time points or to different tumors, followed by Bonferroni post-hoc test to determine statistical significance (Figures 5.4D & F, Figures 5.5B & Figures 5.6C & D).

5.2.12 QSM video of mice with systemic LPS injection

The videos corresponding to the data in Figure 5.6B are uploaded, providing sagittal, coronal, and axial views of the whole body with the accumulation of LMN or NTN into the liver indicated with the same color scheme as in Figure 5.6B. ‘a1.mp4’, ‘a8.mp4’, and ‘a25.mp4’ correspond to the movies of mice at

1, 8, 25 hr post-injection of LMN, respectively. ‘i1.mp4’, ‘i8.mp4’, and ‘i25.mp4’ correspond to 1, 8, 25 hr post-injection of NTN, respectively.

5.3 RESULTS

5.3.1 Synthesis and characterization of leukocyte-mimetic nanoparticles

Selective binding of SPIO nanoparticles to overexpressed ICAM-1 was conferred by surface coating at an optimal density (~100 molecular/particle) with the I domain of LFA-1 integrin, engineered for high affinity by mutations of F265S/F292G (denoted as F265S/F292G, K_D = 6 nM) (118). Among physiological ligands for LFA-1 such as ICAMs and junctional adhesion molecule (JAM)-1 (120), ICAM-1 is most important in the setting of leukocyte adhesion to inflamed endothelium due to its highest affinity to LFA-1 (121), being highly inducible over basal low level expression, and localized expression upon inflammatory signals (116, 122). In order to fine-tune coating density of F265S/F292G and present targeting moiety in a most functional orientation, oleic acid capped SPIO nanocrystals (Ocean Nanotech) were encapsulated with a layer of phospholipid consisting of 80% n-poly(ethylene glycol) phosphatidylethanolamine (DPPE-PEG) and 20% dioleoyl-glycero-succinyl-nitrilotriacetic acid (DOGS-NTA) (Figure 5.1A). DOGS-NTA was used for non-covalent conjugation of targeting moieties with His tag in a robust and reproducible manner via high affinity binding to nickel ions chelated by NTA (Ni-NTA) (117, 123). DPPE-PEG was included to maintain solubility, stability, and for its low immunogenicity and non-specific binding to cells and tissues *in vivo* (124). Transmission electron microscope (TEM) images revealed monodispersed SPIO nanocrystals with an outer layer of micelle-like structure (Figure 5.1B; dark ring density corresponds to uniformly distributed nickel ions (the black arrow in top right) and diffuse dark density to His-tagged proteins attached to Ni-NTA (the white arrow in bottom right)). Hydrodynamic size of SPIO with or without protein conjugation was measured to be 60±10 nm by

dynamic light scattering (DLS), an increase from 15 nm diameter SPIO core mainly due to the addition of phospholipid and PEG.

Prior to detecting ICAM-1 with nanoparticles, we first examined by immunofluorescence flow cytometry (Figure 5.1C) and fluorescence microscopy (Figure 5.1D) soluble I domain (labeled with Alexa Fluor 488 (AF488), Invitrogen) binding to ICAM-1 expressed in monolayer culture of cervical cancer cells (HeLa). Specific binding to ICAM-1 was detected with the F265S/F292G, which was inhibited by unlabeled F265S/F292G. In contrast, no significant binding was observed with the wt I domain (K_D = 1.7 mM) (121) and the I domain containing a mutation of D137A (117), which disrupts the metal-ion dependent adhesion site (MIDAS) and abolishes ICAM-1 binding. The level of nanoparticle binding coated with the I domain variants was overall in good agreement with the soluble I domain binding, which varied in order from highest to lowest, F265S/F292G, wt, and D137A (Figure 5.1E). Markedly, specific binding of SPIO conjugated with F265S/F292G (abbreviated as Leukocyte-Mimetic Nanoparticle or 'LMN') was not inhibited by competition with soluble I domain, presumably due to multivalent interaction between nanoparticles and HeLa cells. Enhanced binding due to avidity effect was also observed in the binding of nanoparticle coated with the wt I domain to HeLa, which resulted in greater binding than with the free wt I domain. ICAM-1-mediated binding of LMN but not with the nanoparticles coated with D137A (abbreviated as Non-Targeted Nanoparticle or 'NTN') led to significant cell surface labeling and internalization into the cells, evidenced by fluorescence microscopy and Perl's Prussian blue staining (Figure 5.1F).

5.3.2 Quantitative measurement of selective binding of LMN by MRI

SPIO nanoparticles are being used in clinics as T2* negative contrast agent for MRI. In order to validate SPIO as MRI contrast agent as well as to test the accuracy of our MRI technique for quantitative mapping

of SPIO (18), ^{3}H-labeled phospholipid was additionally incorporated into the outer phospholipid layer of SPIO. When HeLa cells were incubated with LMN for 4 hr at 37°C, an increase in concentration led to an increase in cellular uptake of nanoparticles, reaching a plateau at 450 ng/10^{6} cells (Figure 5.2A). LMN delivery was specific to ICAM-1 expression, evidenced by little accumulation into HeLa with NTN and much lower delivery with LMN into 293T, a cell line with no or little expression of ICAM-1. HeLa cells with known amount of internalized LMN by ^{3}H-radioisotope decay were then embedded into agarose and scanned with a MRI scanner. As expected, T2* showed a decrease in magnitudes with an increase in the amount of SPIO (Figure 5.2B). With quantitative susceptibility mapping (QSM) algorithm was observed a close agreement with ~30% standard deviation from direct radioactivity measurements of free or intracellular SPIO, highlighting the ability of QSM in detecting as low as 1 μg accumulation into 100 μl in volume (Figure 5.2C).

5.3.3 *Ex vivo* detection of ICAM-1 induction in human tumor xenograft and in inflamed stroma

Not only is ICAM-1 upregulated in several carcinomas compared to respective normal epithelium, implicating active involvement of ICAM-1 in cancer development, its induction has also been observed in tumor vasculature caused by an inflamed network encompassing tumor and tumor microenvironment (125-127). Previously, we have found that human LFA-1 I domain cross-reacted with murine ICAM-1 (117), which was recapitulated by the staining of ICAM-1 induced in murine brain endothelium (b.End3) after lipopolysaccharide (LPS) treatment (Figure 5.3A). When tissue sections of GFP-expressing HeLa xenograft were analyzed for ICAM-1 detection by soluble F265S/F292G labeled with AF594 (Invitrogen), most of the GFP signal was overlapped with red fluorescence (Figure 5.3B). Notably, we found that the majority of endothelial cells (PECAM-1 (CD31) positive) within the tumor were also stained by F265S/F292G. In contrast, the level of ICAM-1 induction and colocalization with CD31 staining in the

vasculature away from the tumor, such as those in the skin, was far lower, amounting to ~15% compared to 70% and 35% of the vasculature within the tumor and its periphery (defined as a region within 300 μm distance from the edge of tumor), respectively (Figures 5.3B-D).

5.3.4 *In vivo* detection of ICAM-1 induction in human tumor xenograft and in inflamed stroma

After confirming specific detection of ICAM-1 in *ex vivo* tumor slice by free F265S/F292G, we then examined if systemically delivered nanoparticles would accumulate to the tumor and inflamed stroma by ICAM-1 targeting. To validate that nanoparticle localization is ICAM-1 specific and not due to an increased permeability of the tumor vasculature, NTN and ICAM-1 negative 293T cell xenograft were used as controls. The growth of HeLa and 293T xenograft in mice was confirmed by whole body imaging of GFP (Figure 5.4A). At 50 hr after intravenous injection of nanoparticles, whole body imaging of near-infrared (near-IR) fluorescence (AF750 attached to the I domains) indicated accumulation of LMN into HeLa but much less into 293T xenograft (Figure 5.4A & B). Subsequent *ex vivo* imaging of the tumor and the major organs harvested from the mice further confirmed a greater level of delivery into HeLa xenograft with LMN (Figure 5.4C). The signal from the kidney was by far greater than those from other organs both for LMN and NTN, indicating ICAM-1 independent clearance through the kidney (Figure 5.4C). Interestingly, higher fluorescence was also detected in the liver with LMN, presumably caused by persistent, low-level inflammation in the liver. Whole body imaging of nanoparticles localized to HeLa and 293T xenograft over the time course of 30 min to 50 hr post-injection showed that the peak accumulation occurred at 1-3 hr post-injection, followed by a gradual decrease over 3 days and a complete clearance by 7 days (Figure 5.4D). The presence of LMN into HeLa was also confirmed by direct staining of iron with Prussian blue (Figure 5.4E & F). To map the distribution of LMN by fluorescence microscopy, SPIO nanoparticles conjugated with AF594-labeled I domains were intravenously injected

into the mice with HeLa/293T xenograft. When the xenograft tissue was examined 4 hr after nanoparticle injection, specific accumulation of LMN into HeLa tumor was observed, judging from colocalization between GFP expression in HeLa and AF594 fluorescence (Figure 5.4G & H). Importantly, consistent with the detection of ICAM-1 in the tumor vasculature by direct staining of the tissue (Figure 5.3B), a high percentage of CD31 positive cells in HeLa as well as in 293T xenografts were also targeted by LMN. The localization of ICAM-1 specific nanoparticles within the tumor-associated vasculature, therefore, was likely responsible for higher signals detected within 293T xenograft at earlier time points (Figure 5.4D), despite the fact that 293T itself exhibited almost no binding of LMN (Figure 5.4E & F). This finding highlights a potential use of LMN for detection of tumor growth by their accumulation into inflamed tumor vasculature, irrespective of the type of tumor surface antigen.

5.3.5 In vivo detection of temporal dynamics of inflammation by optical imaging and MRI

In order to further confirm that our leukocyte-mimetic nanoparticles sensitively detect the induction of ICAM-1 not only due to an inflammatory milieu in the tumor but also by acutely induced inflammation, we imaged mice after subcutaneous (Figure 5.5) or intravenous injection of LPS (Figure 5.6). Temporal mapping of nanoparticle distribution demonstrated a greater localization of LMN into the LPS injection site over PBS injection site as a control, peaking at 12 hr post-injection of LPS and gradually decaying over 72 hr (Figures 5.5A & B). Higher accumulation into the liver was also observed with LMN, attributed to the inflammatory response induced by the leakage of locally injected LPS into circulation. We also observed a rapid increase in fluorescence in the bladder, irrespective of targeting moieties, attributed to renal clearance of some fraction of proteins dissociated from nanoparticles. Interestingly, NTN accumulated more into the LPS site than into the PBS site, presumably due to non-specific phagocytosis of nanoparticles by immune cells. Selected mice treated with systemic delivery of 100 μg LMN were

then subjected to MRI after whole body optical imaging to demonstrate that our nanoparticles could be used for quantitative detection of inflammation by a clinically relevant imaging technique (Figure 5.5C). T2* magnitude images identified the presence of LMN in the LPS injection site as darkness, which could be confused with other dark regions. QSM revealed the accumulation of ~0.3 μg of iron oxide (corresponding to detection of less than 1% of injected dose) into the LPS injection site, colocalized with the site identified by near-IR imaging (Figure 5.5A).

In response to systemic inflammation caused by intravenous injection of LPS for 12 hr prior to nanoparticle (~200 μg) injection, optical mapping of nanoparticle distribution demonstrated greater localization of LMN in the liver compared to that of NTN in mice (Figure 5.6A & C), peaking at 1hr post-injection of nanoparticles and subsequently diminishing at later time points. The level of delivery overall was higher with LPS even with NTN, indicating some of nanoparticles accumulated into the liver was caused by ICAM-1 independent phagocytosis. After optical imaging, mice were transcardially perfused with PBS for MRI, which would have removed nanoparticles retained in the blood pool in the liver. Temporal mapping of SPIO distribution using MRI QSM measured about 20% of the total dose of LMN was specifically uptaken by the liver 1 hr post injection due to LPS-induced inflammation (Figures 5.6B & D and supplementary videos). QSM quantification also demonstrated a similarly greater localization of LMN into the liver under acute inflammation at different time points, exhibiting qualitative agreement with the temporal mapping using optical imaging (Figures 5.6B & D). Discrepancy between optical intensity and QSM was unavoidable as MRI was performed after perfusion of the mice as well as due to the different kinetics of degradation for fluorescence dye (AF750) and SPIO.

5.4 DISCUSSION

Sensitive detection of inflammation will be of high significance for diagnosis of diseases caused directly by host inflammatory response such as sepsis, allograft rejection, lupus, as well as those that are influenced by inflammation such as cardiovascular disease and cancer. In this study, we designed MRI-compatible SPIO nanoparticles, and demonstrated a successful detection of constitutive expression of ICAM-1 in tumor, as well as ICAM-1 induction in tumor-associated vasculature, where tumor growth and angiogenesis are active. Prior approaches to inflammation detection have been largely based on antibodies that are against cell adhesion molecules such as ICAM-1 and VCAM-1 (108-113, 128), lacking in the ability to fine tune affinity and avidity of targeting moieties on nanoparticles that are critical to inflammation-specific targeting. From our previous *in vitro* studies (117, 123), we have demonstrated specific localization into inflamed but not to resting endothelium and immune cells of nanoparticle (50-100 nm in diameter) coated with integrin LFA-1 I domain engineered for high affinity to ICAM-1. Furthermore, combining recently developed quantitative susceptibility mapping technique, we quantified sub-microgram quantity of iron oxide accumulated in both ICAM-1-expressing cell phantom *in vitro* and acute inflammation induced by LPS *in vivo*, corresponding to less than 1% of injected dose.

Despite the fact that ICAM-1 is basally expressed in all endothelium (116, 122) and therefore the notion that ICAM-1 may not be a suitable target for inflammation, our studies emphasize selective delivery by targeting molecules that are induced greatly under inflammation (129, 130). Nanoparticles of ~100 nm will experience hydrodynamic force generated by the blood flow (131, 132), such that there should be sufficient simultaneous molecular interactions with the cells for nanoparticles to remain on cell surface. The number of minimum molecular interactions required for stable adhesion of nanoparticles will also depend on the adhesion strength of each interaction. Therefore, specificity toward high ICAM-1 site will be influenced by the affinity of molecular interaction and the valency between nanoparticles and target cells, where the design of nanoparticles to permit tunable affinity and

avidity of physiological interaction is of significant advantage. Our nanoparticles to a great extent mimic the behavior of activated leukocytes, which would adhere much better to inflamed endothelium.

Increasing number of studies have begun to focus on the crosstalk between the immune activation of vascular niche, angiogenesis, and tumor progression (133, 134). Upregulated levels of ICAM-1 in tumor have been linked to two different contexts, one serving as a marker for the recruitment of effector immune cells and tumor killing (135), while it was also observed in malignant and metastatic tumors with poor prognosis (136). Seemingly contradicting roles of ICAM-1 may be due to the complexity of inflammation in various phases of tumor development, which can be better examined by *in vivo* imaging tools. Our nanoparticles did indeed show the localization into the tumor vasculature, while their localization into the vasculature elsewhere was non-detectable. With human tumor xenograft model, we observed that the majority of tumor mass was comprised of tumor cells with poor vascularity present therein. Higher vascularity was found in the periphery of the tumor, often called the invasive tumor front, where ICAM-1 overexpression associated with higher immune activity has also been reported in many carcinoma cases (126, 137-140). Notably, we have demonstrated that intravenously injected nanoparticles targeting ICAM-1 specifically localized into the vasculature associated with the tumor progression. With further improvement of detection sensitivity in addition to more native tumor models containing not only tumor cells themselves but also fully-developed vasculatures and other stroma cells such as macrophages, our nanoparticles may provide a universal tumor imaging strategy not by tumor surface markers limited to specific cancer types but by the inflamed microenvironment which is associated with almost all cancer development.

Besides sensitive detection of chronic inflammation implicated in cancer, prompt and accurate detection of acute inflammation induced by bacterial or viral infection such as sepsis is also of clinical importance. Acute inflammation dramatically induces ICAM-1 induction not only in endothelium but

also in immune cells, such that both cellular components become the targets by I domain-coated nanoparticle. Using LPS-induced acute inflammation model, we demonstrated optical imaging of the temporal dynamics of inflammation. Specific localization of LMN was also confirmed by QSM technique using MRI. The degree of localization of ICAM-1 targeting nanoparticles into an inflamed site will closely reflect different phases of inflammation, from the onset of inflammation to resolution phase. Therefore, quantitative prediction of spatiotemporal distribution of nanoparticles may provide critical information on diagnosis and the choice of therapy regimen in clinics.

In summary, our ICAM-1 targeting strategy by mimicking the behavior of leukocytes in their ability to localize to the inflamed endothelium was able to detect ICAM-1 overexpression in tumor cells, tumor vascular microenvironment, and acute inflammation. In the design of ICAM-1 targeting nanoparticles by conjugation with LFA-1 I domain, we employed His-tag binding to nickel-NTA, which we previously found (117) to be critical in order to fine-tune the coating density of targeting moieties to be specific to ICAM-1 overexpression but not to basally present ICAM-1. The idea of optimizing molecular interactions by tuning the avidity between ligands and receptors could provide a useful strategy to molecular targeting of some important targets that are basally expressed elsewhere. Inflammation-targeting nanoparticles with the lipid layer shell can also be used to carry small, hydrophobic drugs, achieving simultaneous imaging and targeted drug delivery.

5.5 CONCLUSION

This study presents physiology-inspired design of SPIO nanoparticles for *in vivo* detection by optical imaging and MRI, mimicking activated leukocyte in its ability to recognize inflamed endothelium. Nanoparticles *in vivo* will experience hydrodynamic force induced by the blood flow, requiring simultaneous molecular interactions with sufficient adhesion strength with the cells for nanoparticles to

remain on cell surface. Therefore, the design of nanoparticles with tunable affinity and avidity of physiological interactions would be critical to selectivity and efficiency of leukocyte-mimetic nanoparticles in targeting inflammation. Notably, we observed specific accumulation of systemically-delivered nanoparticles into the vasculature within the tumor and invasive tumor front where the tumor growth and angiogenesis were active, while their localization into the vasculature elsewhere was much lower. The use of two different nanoparticles differed only by the type of I domains (active vs. inactive) as targeting moieties against ICAM-1 enabled us to discriminate inflammation-driven accumulation into the tumor microenvironment from passive distribution, which may result from the leakiness of the vasculature within the tumor. Inflammation-targeting nanoparticles such as SPIO with the layer of phospholipid are also suitable for carrying small molecule drugs, achieving simultaneous imaging and targeted drug delivery.

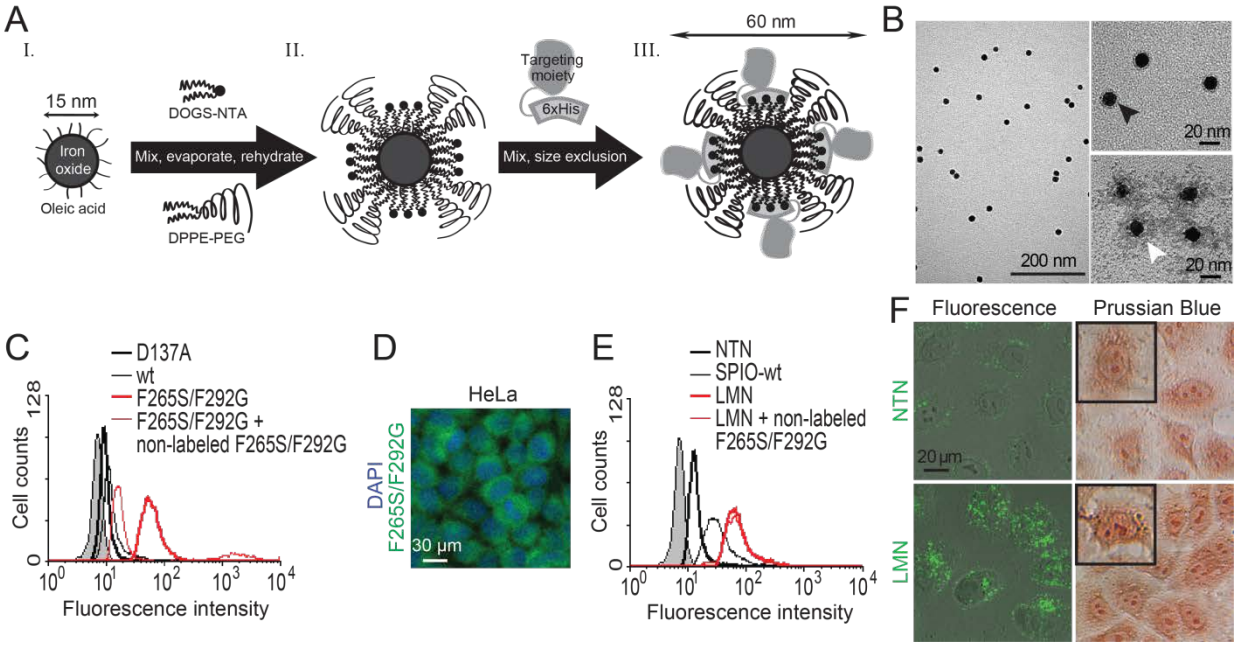
A
I.
II.
III.
15 nm
Iron oxide
Oleic acid
DOGS-NTA
DPPE-PEG
Mix, evaporate, rehydrate
Targeting moiety
6xHis
Mix, size exclusion
60 nm
B
200 nm
20 nm
20 nm
C
D137A
wt
F265S/F292G
F265S/F292G + non-labeled F265S/F292G
Cell counts
Fluorescence intensity
D
HeLa
DAPI
F265S/F292G
30 μm
E
NTN
SPIO-wt
LMN
LMN + non-labeled F265S/F292G
Cell counts
Fluorescence intensity
F
Fluorescence
Prussian Blue
NTN
LMN
20 μm

Figure 5.1. Synthesis, characterization, and *in vitro* delivery of leukocyte-mimetic nanoparticles. (A) A schematic diagram of iron oxide nanocrystals encapsulated into a micelle-like layer composed of amphiphilic phospholipid copolymers (stage I–II) and subsequent protein conjugation for molecular targeting (stage III). (B) Uniformly sized, monodispersed SPIO with 15 nm core revealed by TEM. A close up view on top demonstrates a dark halo corresponding to nickel ions (black arrow) chelated by NTA groups surrounding SPIO. On the bottom is the negative staining of protein-conjugated SPIO with proteins and PEG groups darkly stained (white arrow), in contrast to a brighter phospholipid layer. (C) Flow cytometry measurements of HeLa cells stained with different I domains (10 μg/ml) labeled with AF488. Non-stained HeLa cells are shown in grey shaded histograms. In a competition assay, non-labeled I domains were used at 50 μg/ml. (D) Shown in green is immunofluorescence staining of ICAM-1 in HeLa cells using F265S/F292G labeled with AF488. Nuclei staining by DAPI is shown in blue. (E) Flow cytometry measurements of HeLa cells stained with nanoparticles (25 μg/ml of SPIO and 10 μg/ml of I domains) conjugated with different I domains. Non-labeled I domains as a competitor were used at 50 μg/ml. (F) ICAM-1 dependent internalization of SPIO into HeLa cells was confirmed with confocal fluorescence microscopy and Perl's Prussian blue staining.

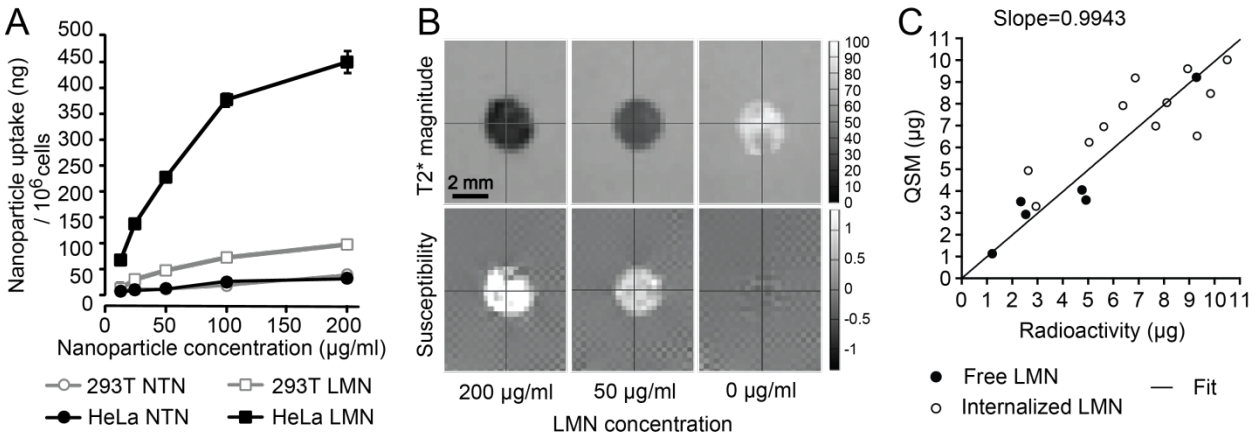

Figure 5.2. Quantitative measurement of selective binding of SPIO to ICAM-1 by MRI. (A) The amount of SPIO internalized into HeLa or 293T was measured by radioisotope measurement of ^{3}H-phospholipid incorporated into SPIO nanoparticles. SPIO nanoparticles were coated with either F265S/F292G (LMN) for ICAM-1 targeting or with D137A (NTN) as a control. (B) T2* and susceptibility images of agarose-embedded HeLa cells that were labeled with 200-0 μg/ml of LMN. (C) A comparison of iron mass estimated by QSM technique and radioisotope measurement. Shown are the measurements of agarose-embedded free LMN (closed circles) and LMN internalized into HeLa cells (closed circles).

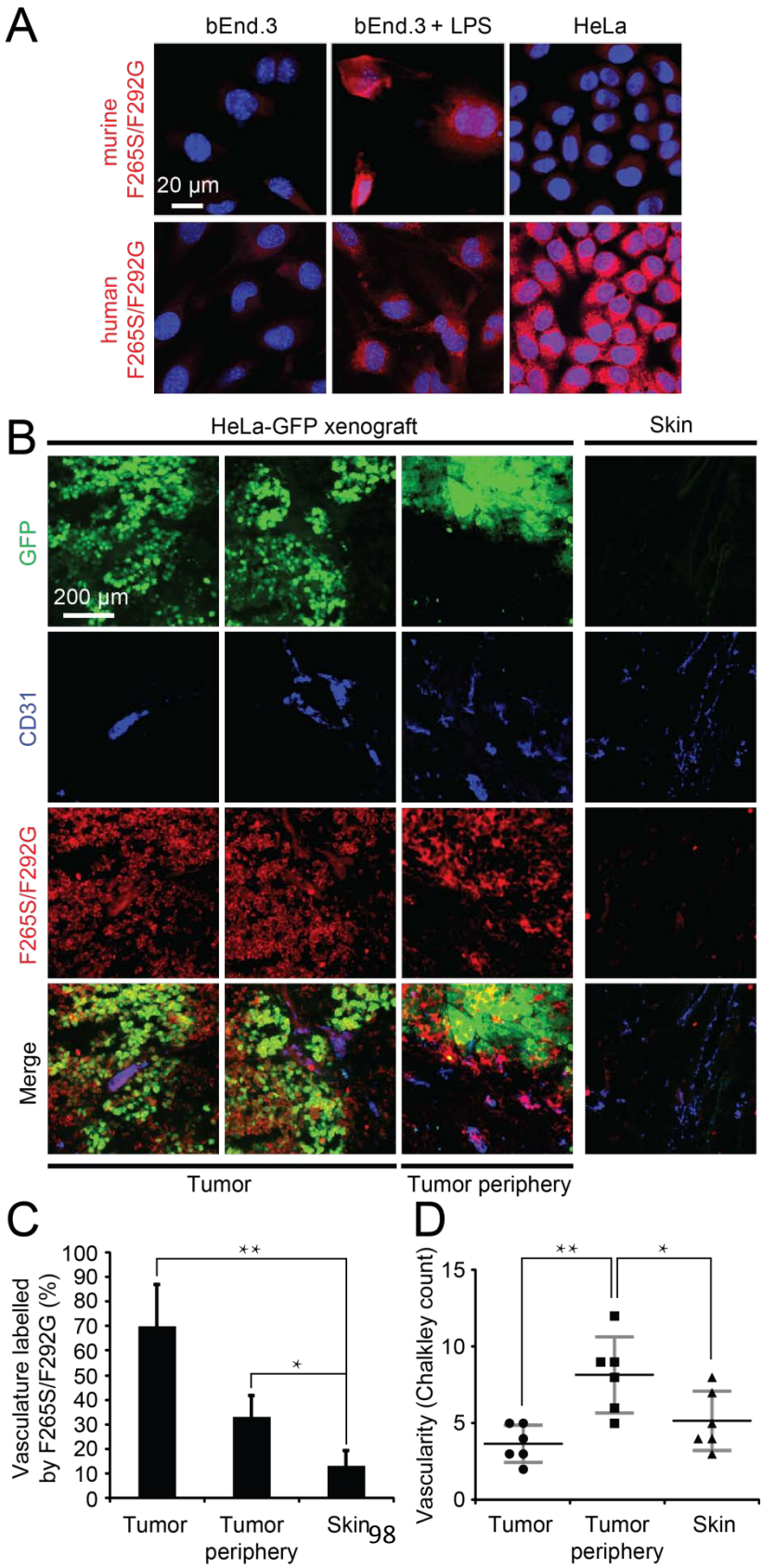
A
bEnd.3
bEnd.3 + LPS
HeLa
murine F265S/F292G
human F265S/F292G
20 μm
B
HeLa-GFP xenograft
Skin
GFP
CD31
F265S/F292G
Merge
200 μm
Tumor
Tumor periphery
C
Vasculature labelled by F265S/F292G (%)
100
90
80
70
60
50
40
30
20
10
0
**
*
Tumor
Tumor periphery
Skin
D
Vascularity (Chalkley count)
15
10
5
0
**
*
Tumor
Tumor periphery
Skin

Figure 5.3. *Ex vivo* molecular imaging of tumor and tumor-associated vasculature. (A) Confocal fluorescence images of murine b.End3 cells before and after LPS treatment and HeLa cells stained with murine (top) and human (bottom) I domains (F265S/F292G) labeled with AF594. Nuclei staining by DAPI is shown in blue. (B) Immunofluorescence images of GFP-expressing HeLa xenograft tumor tissue costained with F265S/F292G-AF594 and anti-murine CD31 antibodies. Skin tissues from non-tumor bearing mice were used as control. (C) The percentages of endothelium costained with CD31 and F265S/F292G within the tumor, in the periphery (300 μm from the tumor), and in the skin were determined from immunohistology (n = 6). (D) Vascularity within the tumor, in the periphery (300 μm from the tumor), and in the skin was quantified using Chalkley's method (25 random points per field of view) (n = 3; *$p < 0.05$, **$p < 0.01$).

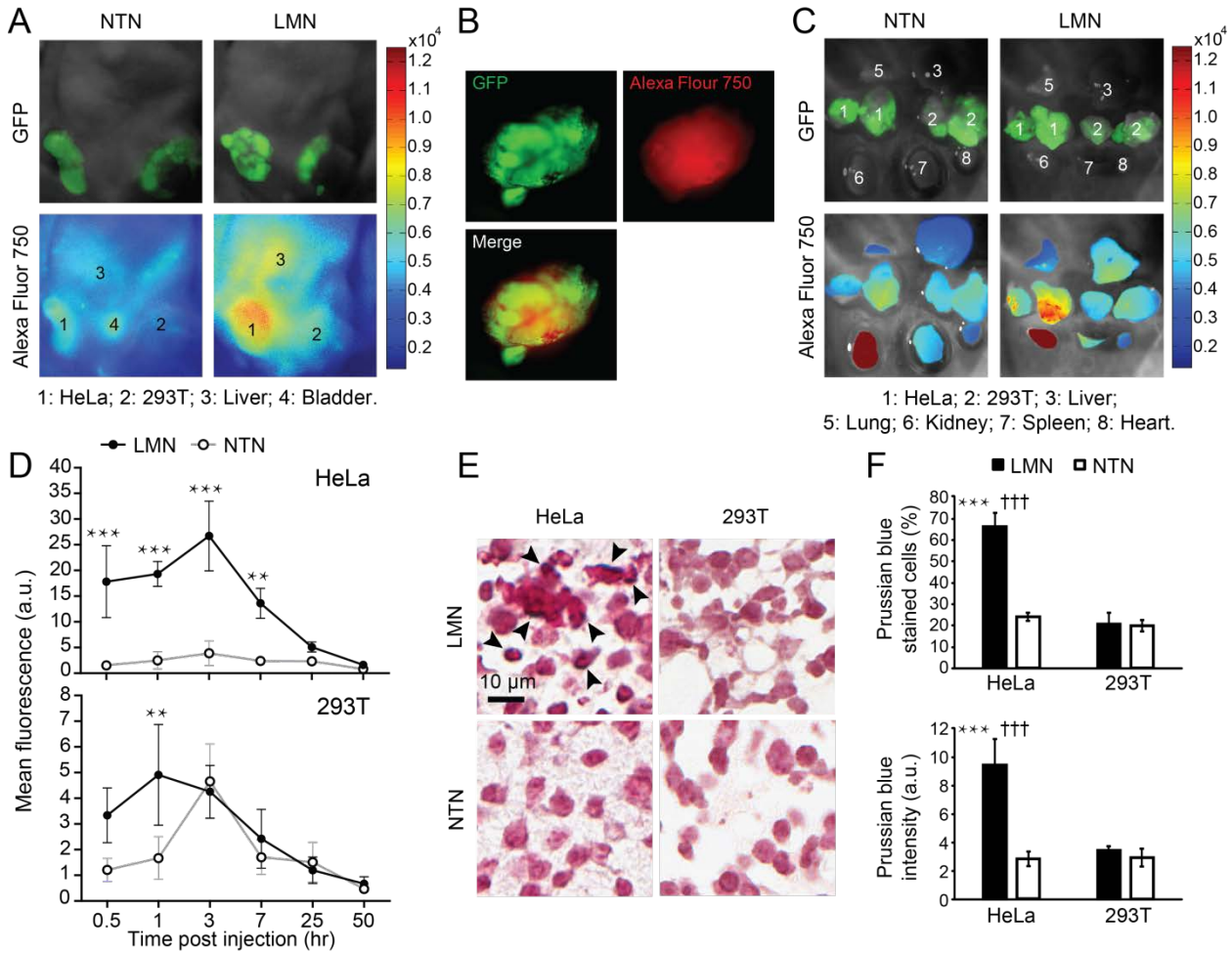
A
NTN
LMN
GFP
Alexa Fluor 750
x10^4
1.2
1.1
1.0
0.9
0.8
0.7
0.6
0.5
0.4
0.3
0.2
1: HeLa; 2: 293T; 3: Liver; 4: Bladder.
B
GFP
Alexa Flour 750
Merge
C
NTN
LMN
GFP
Alexa Fluor 750
1: HeLa; 2: 293T; 3: Liver;
5: Lung; 6: Kidney; 7: Spleen; 8: Heart.
D
LMN
NTN
HeLa
293T
Mean fluorescence (a.u.)
Time post injection (hr)
0.5
1
3
7
25
50
E
HeLa
293T
LMN
NTN
10 μm
F
LMN
NTN
Prussian blue stained cells (%)
Prussian blue intensity (a.u.)
HeLa
293T
G
GFP
LMN
CD31
Merge
293T
HeLa
200 μm
H
GFP/DAPI
NTN
293T
HeLa
200 μm

Figure 5.4. *In vivo* molecular imaging of tumor and tumor-associated vasculature. *In vivo* (A, B) and *ex vivo* (C) near-IR imaging of mice at 50 hr after intravenous injection of NTN vs. LMN. GFP indicates the growth of HeLa ('1') and 293T ('2') tumors. The distribution of nanoparticles into the major organs ('3'-'8') were also examined. (D) Near-IR fluorescence intensities of HeLa and 293T tumors at different time points after intravenous injection of LMN vs. NTN (n = 4; **P < 0.01, ***p < 0.001). (E) Perl's Prussian blue staining of tumor sections collected at 50 hr after the injection of LMN vs. NTN. Stained iron is marked with black arrows. (F) Percentage of cells stained in Prussian blue (top) and the intensity of Prussian blue in the field of view (bottom) within tumor sections (n = 3; ***p < 0.001 between LMN vs. NTN in HeLa tumor. †††p < 0.001 between HeLa and 293T tumor using LMN). (G) Immunofluorescence imaging of tumors at 4 hr post-injection of LMN. Tumor sections were also stained with anti-CD31 antibody for delineating vasculature. LMN localization into the tumor vasculatures was indicated with white arrows. (H) Fluorescence imaging of tumors at 4 hr post-injection of NTN.

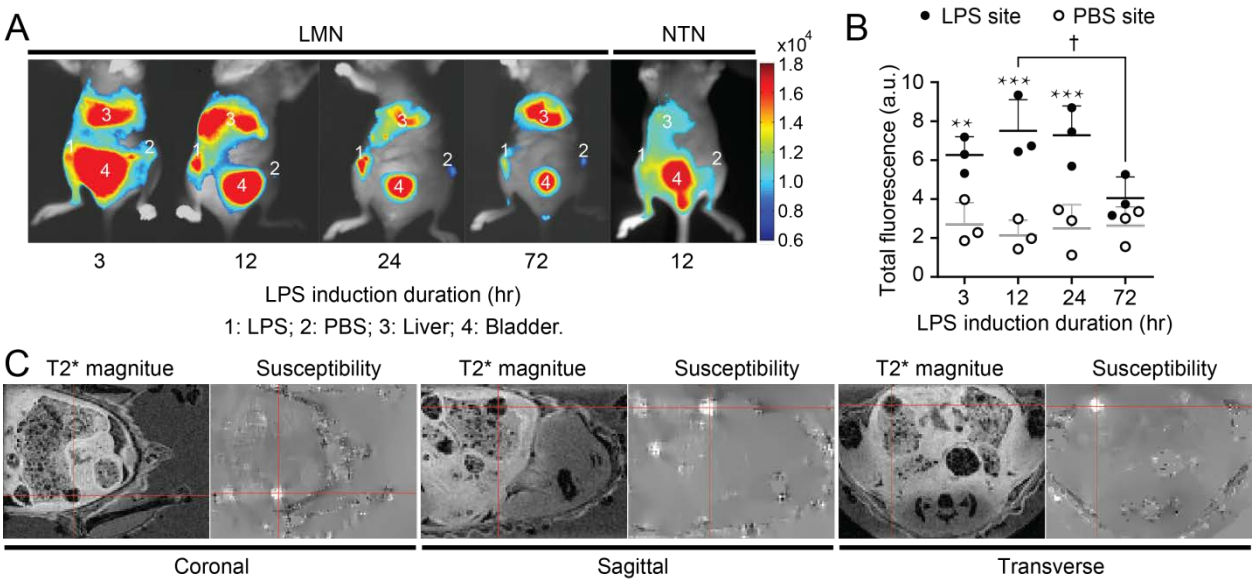

Figure 5.5. *In vivo* molecular imaging of subcutaneous acute inflammation using near-IR camera and MRI. (A) *In vivo* near-IR whole body imaging of LMN vs. NTN distribution in mice 1 hr after nanoparticle injection. Mice were exposed to LPS ('1') and PBS ('2') for 3, 12, 24, or 72 hr at the time of nanoparticle delivery. (B) Fluorescence intensities of LMN at LPS vs. PBS injection sites were shown (n = 3; **$p < 0.01$, ***$p < 0.001$ between LPS and PBS site at specific time points; $^{\dagger}p < 0.05$ between 12 hr and 72 hr at LPS site). (C) T2* magnitude and susceptibility mapping images of nanoparticle distribution in mice at 4 hr after nanoparticle injection. Mice were exposed to LPS/PBS for 12 hr at the time of nanoparticle injection. Bright spot identified by susceptibility mapping as the accumulation of SPIO was indicated with crosshair.

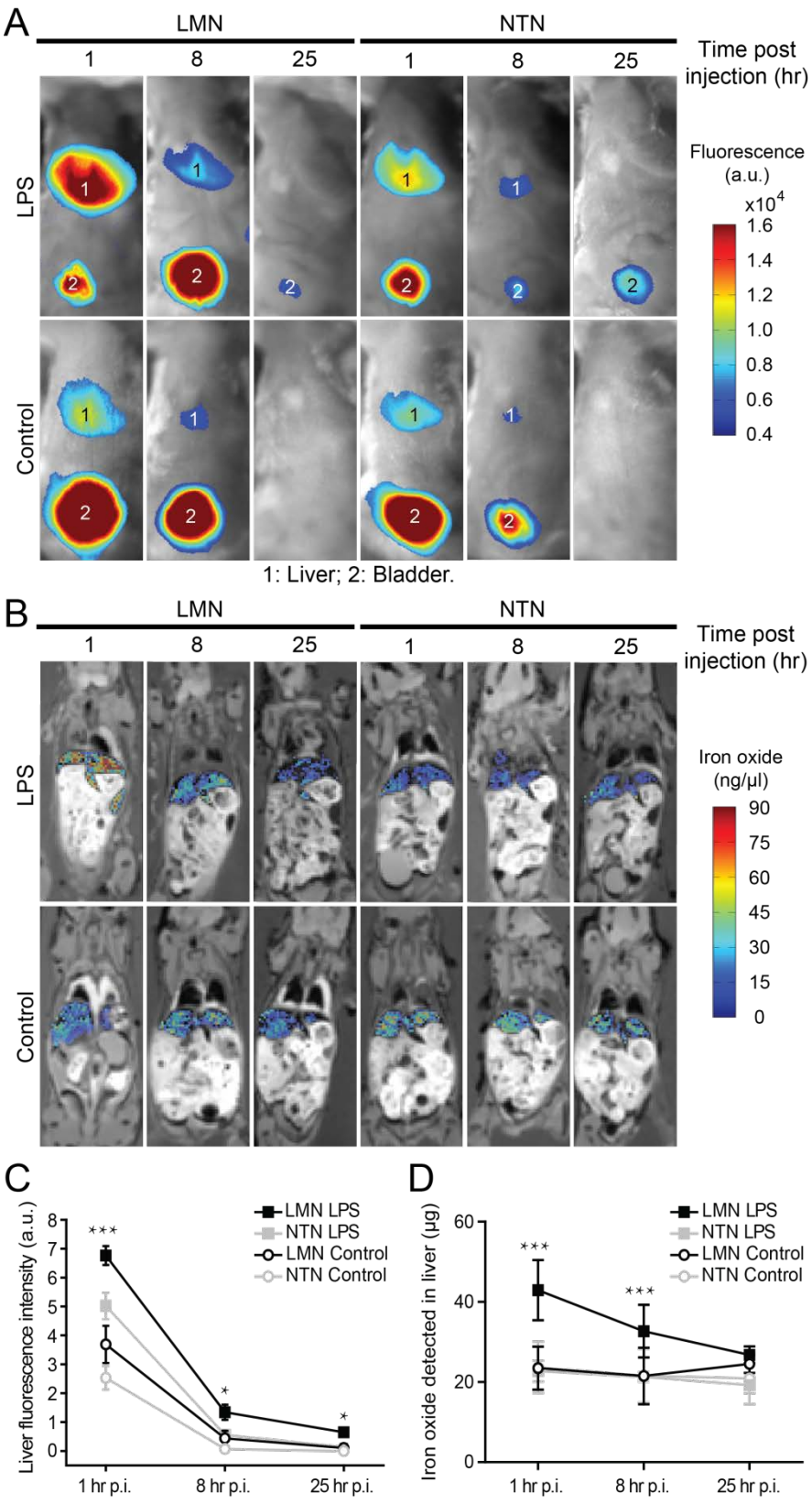
A
LMN
NTN
1
8
25
1
8
25
Time post injection (hr)
LPS
Control
Fluorescence (a.u.)
x10^4
1.6
1.4
1.2
1.0
0.8
0.6
0.4
1: Liver; 2: Bladder.
B
LMN
NTN
1
8
25
1
8
25
Time post injection (hr)
LPS
Control
Iron oxide (ng/µl)
90
75
60
45
30
15
0
C
Liver fluorescence intensity (a.u.)
LMN LPS
NTN LPS
LMN Control
NTN Control
***
*
*
1 hr p.i.
8 hr p.i.
25 hr p.i.
D
Iron oxide detected in liver (µg)
LMN LPS
NTN LPS
LMN Control
NTN Control
***
***
1 hr p.i.
8 hr p.i.
25 hr p.i.

Figure 5.6. *In vivo* molecular imaging of systemic acute inflammation using near-IR camera and MRI. *In vivo* near-IR whole body imaging (A) or MRI (B) of LMN vs. NTN distribution in mice at 1, 8, 25 hr post-injection of nanoparticles in mice exposed to systemic LPS for 12 hr or control mice with no treatment. LMN vs. NTN distributions into the liver were quantified by near-IR optical imaging (C) and MRI (D) (n = 3; *$p < 0.05$, ***$p < 0.001$ between LMN vs. NTN at specific time points).

CHAPTER 6 – TARGETED NANOPARTICLES TO VISUALIZE ACUTE INFLAMMATION: PART II

Includes material previously published in: Wong R, Chen X, Wang Y, Hu X, Jin MM. Visualizing and Quantifying Acute Inflammation Using ICAM-1 Specific Nanoparticles and MRI Quantitative Susceptibility Mapping. Ann Biomed Eng. 2011.(141)

6.1 INTRODUCTION

Nonresolving inflammation contributes significantly to the pathogenesis of a variety of human diseases and represents one of the most significant factors of medical burden worldwide(101). While inflammation is typically initiated in response to harmful stimuli, dysregulation of the inflammation pathways can result in prolonged and excessive inflammation, leading to host damage that can surpass the harm inflicted by the original pathogen(142). Indeed, unresolving chronic inflammation has been linked to atherosclerosis(143), obesity(144), and cancer(106), prolonged acute inflammation has been closely associated with sepsis(145) and local infections(146), and the cyclic coexistence of acute and chronic inflammation has been implicated in rheumatoid arthritis(147), asthma(148), multiple sclerosis, Crohn's disease, and ulcerative colitis(101). Of particular concern of inflammatory dysregulation is the intense localized recruitment of macrophages, lymphocytes, and neutrophils to otherwise healthy tissue, resulting in necrosis of vital tissues and organs, contributing greatly to increased patient morbidity and mortality(149). Thus, identifying localized inflammation in the context of broader inflammation-driven diseases can aid in isolating regions at risk of host-response necrosis and can provide a valuable insight into the progression and severity of the condition.

Current approaches to inflammation detection employ various markers as targets for biospecificity, including soluble extracellular molecules, such as fibrinogen(150), factor XIII(151), and collagen(152), as well as cell surface molecules such as tissue factor(153), chondroitin sulfate proteoglycans(154), vascular adhesion molecule (VCAM-1)(155), and ICAM-1(123, 156, 157). Of particular interest is ICAM-1, a transmembrane molecule that displays a distinct spatiotemporal response to inflammation. While basally expressed at low levels throughout the body under normal conditions, ICAM-1 is highly inducible under inflammatory stimuli(158) and exhibits highly localized cell surface expression on immune and non-immune cells, such as endothelial cells, fibroblasts,

lymphocytes, and myeloid cells(116). Furthermore, cell surface ICAM-1 overexpression has been linked to various diseases and conditions, and correlates well with inflammation-related tissue and organ damage resulting from hepatic ischemia(159, 160), intestinal and colon ischemias(161), hepatitis, cirrhosis, Wilson's disease, transplantation rejection(162), pancreatitis(163), type 1 diabetes(164), and multiple organ dysfunction syndrome in sepsis(145). To target cell surface ICAM-1, we previously employed a high affinity variant of the domain called inserted (I) domain(118), present in the α subunit of the integrin lymphocyte function-associated antigen (LFA)-1 and solely responsible for LFA-1 interaction with ICAM-1(122).

One potential application for specific inflammation imaging is for the detection of sepsis. Sepsis is the leading cause of death in critically ill patients admitted to the medical intensive care unit (ICU) in the United States(27), defined as a systemic inflammatory response to infection manifested by two or more systemic inflammatory response syndrome (SIRS) criteria (such as changes in body temperature, tachycardia, and changes in the number and/or immaturity of white blood cells)(145). Under sepsis, the endothelium experiences sustained and generalized activation, resulting in procoagulant phenotype, increased endothelial cell apoptosis, increased expression of adhesion molecules, and ultimately organ-specific coagulation and dysfunction(145). As ICAM-1 plays a significant role in mediating leukocyte adhesion as a part of inflammatory response and has been linked to organ-specific inflammation-driven necrosis, identifying sites of high ICAM-1 expression may offer detection or even additional insight into the progression of sepsis or other systemic inflammatory response not offered by existing diagnostic techniques.

In this study, we demonstrate that high resolution spatiotemporal imaging of LPS-induced systemic inflammation through the use of inflammation-specific nanoparticles termed leukocyte-mimetic nanoparticles (LMN)(100), a fluorescently tagged ICAM-1 specific nanomicelle encapsulating

superparamagnetic iron oxide nanoparticle as a targeted bimodal near-infrared (IR) optical/magnetic resonance imaging (MRI) contrast agent. Using optical imaging and a novel MRI quantitative susceptibility mapping (QSM) technique(18), and directly corroborated by radiolabeled isotope measurement, we utilize LMN to quantitatively observe the degree of localized acute inflammation as an indicator of sepsis progression. By tracking the biodistribution of nanoparticles using whole body imaging techniques, we have found greater accumulation of LMN than that of non-ICAM-1 specific controls in the liver of septic mice, while this difference in accumulation was absent in the liver of non-septic mice. In contrast, greater accumulation of nanoparticles irrespective of ICAM-1 targeting was observed in the spleen of septic mice than that of non-septic control, suggesting that localization into the spleen was mainly a result of ICAM-1 independent phagocytic activity. Our study demonstrates the utility of quantitative MRI-based detection of ICAM-1 specific nanoparticles in the major organs including the liver and spleen, organs closely associated with systemic inflammatory response, as a diagnosis method for systemic inflammation through the imaging and quantification of localized inflammation.

6.2 MATERIALS AND METHODS

6.2.1 Preparation of ICAM-1 specific nanoparticles (Leukocyte-mimetic nanoparticles (LMN))

Details in the synthesis of LMN were described previously(100). Briefly, oleic acid-capped superparamagnetic iron oxide (SPIO) nanocrystals (15 nm in diameter, Ocean Nanotech, LLC) were additionally coated with an outer layer of phospholipid, consisting of 1,2-dipalmitoyl-snglycero-3-phosphoethanolamine-N-[methoxy(polyethylene glycol)-2000] (DPPE-PEG) and 1,2-dioleoyl-sn-glycero-3-[(N-(5-amino-1-carboxypentyl)iminodiacetic acid)succinyl] nickel salt (DOGS-NTA) (Avanti Polar Lipids, Inc.). Radiolabeled lipid-coated SPIO nanoparticles were synthesized by addition of ^{3}H-DPPC (L-α-

Dipalmitoyl-Phosphatidylcholine) (Perkin Elmer) at less than 5% of the total phospholipid to the mixture of DPPE-PEG and DOGS-NTA. The lipid layer on SPIO nanoparticles was formed by hydration of the mixture of lipid-film and SPIO, and lipid-coated SPIO were then purified by density centrifugation, followed by a gel filtration technique. LFA-1 I domains containing mutations of Asp137->Ala (D137A; non-ICAM-1 specific) and Phe265->Ser/Phe292->Gly (F265S/F292G; ICAM-1 specific) fused to His tag (6 histidine residues) at the N-terminal were produced as previously described(100). Conjugation of lipid-SPIO with His-tagged I domains was obtained by incubation of nanoparticles with I domains at 4°C overnight, forming LMN (with F265S/F292G) and non-targeting nanoparticle (NTN) (with D137A). All fluorescently labeled nanoparticles were prepared by covalently conjugating Alexa Fluor 750 (AF750) (succinimidyl esters (Invitrogen) to the I domains.

6.2.2 Animal Model of Acute Inflammation

All animal experiments were conducted in compliance with the regulations defined by the Institutional Laboratory Animal Use and Care Committee of Cornell University. 1 mg/ml LPS in 100 µl PBS were injected intravenously through retroorbital vein into 8-wk-old female BALB/c mice 12 hr before nanoparticle administration. Prior to imaging hair was removed to reduce background fluorescence. Mice with no treatment were used as negative control. Three mice per group were used for each treatment and imaging regimen.

6.2.3 Near-IR Optical and MR Imaging of Mice

Animals were anesthetized with isoflurane mixed with oxygen at 5% and maintained at 2% isoflurane during whole body imaging (Olympus, OV100). After 12 hour treatment with LPS or no-treatment control, mice were administered with 100 µg of nanoparticles coated with AF750-conjugated I domains

in 150 µl pH 7.4 PBS via retro-orbital injection. Near-IR images of the same mice were taken three times at 1, 8, and 25 hours after nanoparticle injection. Image analysis was performed with Matlab R2007a (MathWorks). Mice were euthanized at 1, 8, or 25 hours after injection of nanoparticles for MRI by intraperitoneal injection of 2.5% tribromoethanol (20 µl/g), transcardially perfused with pH 7.4 PBS, and fixed in 4% paraformaldehyde. Prepared mice were scanned on a 3T scanner (GE Signa Excite) with 3D multi-echo enhanced fast gradient echo (EFGRE) sequence. Imaging parameters were as follows: TEs 3.696 ms, 4.196 ms, 5.696 ms, 11.696 ms, 35.696 ms; TR 40 ms; flip angle 30°; matrix size 256x64x64; voxel size 500 µm isotropic. A 3D Fourier transform was applied to the raw k-space data to reconstruct the images. QSMs were reconstructed using the COSMOS technique, as previously described(100). Regions of interest were segmented for the liver, spleen, and kidneys, and SPIO localization was estimated using QSM, normalized to a calibration standard.

6.2.4 Histological Sections

At 1 hour post nanoparticle injections, mice were euthanized and perfused with PBS transcardially. Liver tissues were then collected from animals. Part of the tissues were fixed in 4% paraformaldehyde, embedded in paraffin, sliced into 4 µm slides, and stained with hematoxylin and eosin (H&E) or with Perl's Prussian blue. The rest of the tissues were frozen in OCT compounds (Sakura Finetek), sectioned to 10 µm slides, and immunostained with rat anti-mouse CD68 (BioLegend) for detection of macrophages.

6.2.5 Quantification of Radiolabeled LMN

Animals were anesthetized with isoflurane and each was administered with 100 µg ^{3}H-labeled SPIO (600 nCi per mouse) in 100 µl PBS via retro-orbital injection. At 1 hour post injection, blood samples were

first collected and mice were perfused with PBS and sacrificed. Major organs were harvested, homogenized, lysed in tissue solubilizer (Fisher), and then mixed with scintillation counter fluid for radioactivity measurement (Beckman Coulter). Percent distribution into the major organs was obtained after normalization to the total counts of radioisotope decay per animal.

6.2.6 Surface Plasmon Resonance (SPR) Analysis

The affinity of human LFA-1 I domains, F265S/F292G and D137A, to murine ICAM-1 was determined by SPR using BIAcore (BIA2000), as previously described(118). In brief, a CM5 sensor chip was prepared using an amine coupling kit (BIAcore) to immobilize recombinant murine ICAM-1fusion with human IgG1 Fc (R & D Systems). Then F265S/F292G and D137A were injected over the chip in injection buffer (20 mM Tris HCl, pH 8.0, 150 mM NaCl, 10 mM $MgCl_2$) at a flow rate of 10 µl/min at RT. In order to examine the specificity of nanoparticle to the level of ICAM-1 expression, CM5 sensor chip was immobilized with three different concentrations of ICAM-1, representing basal to highly induced cell surface density (200, 1000 and 3,250 molecules/μm^2)(165). Nanoparticles were then flowed over the chip at a flow rate of 15 µl/min to approximate the shear force on nanoparticles *in vivo*.

6.2.7 Statistical Analysis

Statistical analysis was performed using two-way analysis of variance and one-way analysis of variance with Tukey's HSD post-hoc test at 95% confidence interval (GraphPad Prism).

6.3 RESULTS

Previously, we validated the suitability of I domain as a targeting moiety for selective binding of nanoparticles to ICAM-1 overexpression(100, 123, 156). In order to design control nanoparticles, termed

non-targeted nanoparticle (NTN), we used the same LFA-1 I domain but containing a mutation of D137A, which abolished a ligand-binding site called a metal-ion adhesion site (MIDAS) and subsequently its binding to ICAM-1 (Figure 6.1A). SPR measurement confirmed our previous observation with cell staining(100) that human I domain cross-reacted with murine ICAM-1 with comparable affinity to human ICAM-1 (K_D = 2 nM to murine ICAM-1 vs. 6 nM to human ICAM-1(118); Figure 6.1B). Subsequent conjugation of F265S/F292G and D137A to prepared lipid-coated SPIO nanoparticles produced LMN and NTN, respectively, through spontaneous assembly from binding of His tag (6 x histidine residues) to Nickel-NTA (Figure 6.1C).

Prior studies demonstrated that the number of targeting moieties on nanoparticles affected selectivity and targeting efficiency of nanoparticles in binding to cells(100, 166). In order to preferentially target ICAM-1 induced under inflammation but not basally expressed ICAM-1, an optimal ratio of I domain to nanoparticle was empirically determined (~100 molecules per nanoparticle(156)). When an SPR chip was prepared with varying ICAM-1 densities representing basal to high levels of ICAM-1 expression (200, 1000 and 3,250 molecules/μm^3), LMN binding was limited to the surface coating with higher than normal ICAM-1 site density, while LMN binding to the basal ICAM-1 surface was the same as the background levels seen with NTN (Figure 6.1D).

To obtain qualitative assessment of nanoparticle biodistribution, we first imaged each mouse using near-IR optical fluorescence camera. Near-IR optical temporal mapping of the nanoparticle distribution demonstrated greater localization of LMN into the liver in mice treated with LPS (Figures 6.2A & 6.3A). Control nanoparticles (NTN) also exhibited slightly higher accumulation into the liver of LPS-treated mice, which might be attributed to increased ICAM-1 independent phagocytic activity of immune cells or increased blood pool retention due to the inflammation in the liver. Higher fluorescence in the bladder was found to be due to some degree of shedding of the I domains from the nanoparticles,

which would be small enough to pass through glomerular capillaries in the kidney and collected into the bladder. After optical imaging, mice were sacrificed, transcardially perfused with PBS to remove nanoparticles in the blood, and subjected to MRI to quantitatively map nanoparticle distribution by QSM. Full body temporal mapping of the SPIO distribution was conducted and individual organs were segmented for analysis (Figures 6.2B & C, Supplemental Figures 6.1A & B). Specific SPIO quantification of each organ revealed a greater localization of LMN in the liver compared to that of NTN in mice with LPS treatments (Figure 6.2B, S6.1A), peaking at one hour and progressively diminishing at each subsequent time point. In contrast to higher accumulation of NTN by optical imaging in the liver of LPS-treated mice (Figure 6.2A), QSM quantification (Figures 6.2B & 6.3B, Supplemental Figures 6.1A & B) and radioisotope measurement (Figure 6.3C) performed after perfusion revealed that NTN accumulation in the liver was not augmented by LPS treatment, indicating that the higher fluorescence with LPS treatment is due to the increase in the blood pool retention of NTN. While the presence of LPS or the type of nanoparticles administered each independently influenced the magnitude of observable nanoparticle accumulation in the liver, the simultaneous interaction of LMN and LPS had a statistically significant effect in all measured time points (Table 5.1). In the spleen, higher amounts of nanoparticle accumulation were detected for LPS treated mice versus untreated controls, regardless of the type of nanoparticles used (Figures 6.2C & 6.3B, Supplemental Figure 6.1B). Therefore, LPS treatment was the predominant differentiating factor in observable nanoparticle accumulation in the spleen, independent of the targeting moiety or the interaction between LPS treatment and type of nanoparticle injected (Table 6.1). Negligible amounts of SPIO were detected in the kidneys, supporting the speculation that nanoparticles of ~60nm in size(100) would be too large for renal filtration.

To further validate MRI quantification of nanoparticles, the values obtained with QSM technique were directly compared to those quantified by measuring radioisotope decay of ^{3}H-labeled

nanoparticles. Mice were treated with LPS for 12 hours and subsequently injected with ^{3}H-labeled LMN or NTN. At 1 hour post nanoparticle injection, blood was collected and after perfusion and sacrifice of the mice, organs were harvested. Radioactivities of the blood and major organs such as liver, kidney, and spleen were measured and normalized to the total radioactivity of each mouse in order to quantify percent nanoparticle biodistribution in the major organs (Figure 6.3C). Highest radioactivity, irrespective of LMN vs. NTN and LPS vs. no treatment, was observed in the blood with a mean radioactivity of ~40%, followed by the levels in the liver with significantly higher radioactivity detected in LPS/LMN-treated mice (31.3 ± 6.7%) than those in non-LPS/LMN-treated (14.8 ± 9.9%), LPS/NTN-treated (13.6 ± 6.6%), or non-LPS/NTN-treated controls (17.2 ± 5.7%). Significantly lower amounts (less than 10% of the total) were detected in the lung, kidney, and spleen (Figure 6.3C and not shown). Consistent with the QSM measurement of nanoparticle distribution in the spleen, slightly higher amounts of radioactivity were observed in the spleen of LPS-treated (2.7 ± 0.7%) than non-treated (1.5 ± 0.5%) mice. Values obtained by radioisotope measurement and by QSM showed overall an excellent linear relationship ($s_{y.x}$ = 1.60 %), with QSM overestimating radioisotope measurements by approximately 25% (Figure 6.3D).

In order to examine cellular basis for the increase in LMN accumulation into the liver in LPS-treated mice, selected liver tissues were stained for identification of different types of cells (hepatocyte, endothelium, and Kupffer cells) and localization of nanoparticles (Figure 6.4). Vasculature dilatation was apparent in LPS-treated liver tissue (Figure 6.4A) with LMN deposited primarily on endothelial cells and Kupffer cells (Figure 6.4B). Simultaneous detection of Kupffer cells (CD68) and nanoparticles by Prussian Blue staining revealed that most large deposits of LMN were accumulated into Kupffer cells, implying that higher accumulation of LMN over NTN in the liver of LPS-treated mice is mainly due to ICAM-1 induction and uptake by Kupffer cells.

6.4 DISCUSSION

With developments in quantitative MRI techniques, this study presents a clinically adaptable method for organ-level mapping of inflammation by quantifying the susceptibility of SPIO-based contrast agents, a measure directly proportional to SPIO concentration. While existing methods for detecting inflammation exist in the context of sepsis diagnosis, such detection methods typically rely on bulk measurements of the presence of pathogens, blood-borne cytokines, and other inflammatory markers, lacking in the spatiotemporal progression and detection of inflammation locally in the body. Central to inflammation is the adhesion of leukocytes to vascular endothelium, a process mediated by molecular interactions between cell adhesion molecules such as integrins and ICAM-1. Toward a sensitive molecular imaging of inflammation, we designed nanoparticles to mimic the ability of leukocyte to preferentially adhere to inflamed vasculature, which was achieved by attaching the high affinity I domain of LFA-1 to nanoparticles. Despite the fact that ICAM-1 is basally expressed in many different types of cells including endothelium and immune cells, our nanoparticles were shown to be selective to vasculature under inflammation with upregulated ICAM-1 expression(100). Capable of *in vivo* detection by optical imaging and MRI techniques, leukocyte-mimetic nanoparticle has previously been shown to specifically localize to the areas of acutely induced local inflammation and to the vasculature within and in the vicinity of the tumor growth, providing spatial and temporal insight into various inflammation-related diseases and conditions. In this study, we demonstrated the potential use of LMN as a bimodal diagnostic agent for the early detection of sepsis or systemic inflammatory response using quantitative MRI techniques.

Previously, we have described a tunable approach to creating nanoparticles that mimic an intrinsic behavior of leukocytes that bind selectively to inflammatory sites(156). By modulating the affinity and avidity of surface-bound I domains for targeting inflammation, we were able to construct nanoparticles that can resist thermal diffusion and detachment forces exerted by fluid-induced shear

stress, while allowing little binding to cells with only basal levels of ICAM-1 expression. Approximately 100 I domains were conjugated to the surface of each LMN, roughly comparable to that of a surface density-optimized approach to ICAM-1 specific nanoparticle design(156, 166). While prior approaches have demonstrated the appeal of employing both selectin ligands and anti-ICAM-1 antibodies to more accurately mimic the rolling and adhesion characteristics of leukocytes(167, 168), we chose to utilize as the targeting moiety for LMN the I domain of LFA-1 integrin, which has been engineered to engage with ICAM-1 with high affinity without prior dependence on interaction with selectins. We found that a targeting moiety derived from physiological molecules, optimized for affinity and avidity, gave superior selectivity and targeting efficiency to inflamed cells in *in vitro* and *in vivo* settings(100, 156).

In treating mice with ICAM-1-specific LMN, we were able to readily differentiate between mice, either pre-treated with LPS or left untreated, by quantitatively measuring nanoparticle localization in various abdominal organs in each of the subjects. This differential effect is most apparent when measuring nanoparticle localization in the liver; a temporal mapping of nanoparticle distribution through MRI QSM demonstrated significantly greater localization of LMN into the liver of sepsis-induced mice compared to that of non-septic subjects, or of those treated with ICAM-1 independent NTN. The observed differences by QSM, corroborated qualitatively by near-IR optometry, were most pronounced one hour after the treatment of nanoparticles, gradually decaying over time while persisting through at least 24 hours after nanoparticle injection. While particles of ~100 nm in diameter in systemic circulation may accumulate in the liver regardless of targeting moiety due to phagocytic activity of immune cells within the liver, the ICAM-1 specificity conferred by the surface conjugation of high affinity I domain (F265S/F292G) of LFA-1 on LMN led to a close to a 2-fold increase in the accumulation in the liver to enable quantitative differentiation. NTN nanoparticles, conjugated with the same LFA-1 I domain but with an inactivating mutation, D137A, did not exhibit higher accumulation into the inflamed liver.

This observation was corroborated through histology using iron stating of tissue sections of the liver, revealing a greater degree of nanoparticle accumulation in LPS-treated LMN cases with specific staining observed in both endothelial cells and Kupffer cells with the most significant nanoparticle accumulations co-localized in the Kupffer cells. Thus, while ICAM-1 is basally expressed in all endothelium and utilizing it as a molecular target for inflammation and sepsis imaging techniques may lead to a background signal, it was found that this background binding was negligible, judging from no difference between LMN and NTN accumulations into the liver by radioactivity measurement and QSM. The relationship between LMN biodistribution independent of ICAM-1 expression can be further characterized through the use of ICAM-1 knockout mice or through the use of blocking antibodies to systemically eliminate available ICAM-1 binding sites.

A high degree of nanoparticle localization was also observed in the spleen of LPS-treated mice through optical imaging and QSM. However, unlike the observations in the liver, increases in nanoparticle accumulations to the spleen were observed in all LPS-treated subjects, regardless of the targeting moiety employed, suggesting that localization is a result of phagocytic activity rather than ICAM-1 biospecificity. Severe and pervasive inflammation, such as that prompted by LPS-induced systemic endotoxic shock, may result in increased phagocytic uptake of nanoparticles in areas in the immediate proximity of major monocyte sources in the spleen, an organ that functions as a major reservoir for undifferentiated monocytes before inflammation-initiated recruitment(169), and is responsible for the release of splenic lymphokines necessary for the increase of phagocytic activity of macrophages cells in response to inflammatory stimuli(170-172). While studies have indicated high ICAM-1 expression in the epithelial cells of the lungs due to endotoxin-induced inflammation(173, 174), MRI-based techniques such as QSM cannot quantitatively differentiate between signal voids resulting from SPIO-based spin dephasing and signal voids created by air. This difficulty with reliably

differentiating QSM-based quantification of SPIO deposits and air may be overcome by multiple data acquisition at differing magnetic field strengths (175).

Using radiolabeled SPIO nanoparticles, we were able to provide a quantitative mapping of nanoparticle distribution by the measurement of radioactivity and at the same time clinically relevant QSM technique based on MRI. At one hour post nanoparticle injection, QSM determined that ~39% of injected nanoparticles were localized into the liver of LPS/LMN mice, a value 70% greater than that of negative controls. In comparison, radioisotope quantification found ~31% of the total body radioactivity was located in the liver of LPS/LMN treated mice, a value 81% greater than that of negative controls. However, some difference in QSM quantification vs. radioactivity measurement of nanoparticles was unavoidable as it was found that the lipid layer outside of SPIO was subject to some degree of shedding during circulation. This may explain, in the course of optical imaging, varying degrees of fluorescence (conjugated to the I domains) observed in the bladder of each subject, regardless of the nanoparticle targeting moiety. The decoupling of the fluorescence or protein from nanoparticles was found to be caused by shedding of the phospholipid lipid layer from SPIO or lipid degradation by phospholipase activity in the plasma, but not due to dissociation between His tag and Ni-NTA, judging from a dramatic decrease in decoupling when crosslinkable fatty acids were used to cage SPIO (data not shown).

Sepsis represents a continuum in clinical-pathologic severity with definable phases that characterize patients at risk for increased mortality. Current diagnosis techniques have limited windows of detection and may rely on transient biology and physiological conditions that may not persist across all phases of sepsis progression. Moreover, the onset of sepsis can be linked to a widely heterogeneous set of initial risk factors, further complicating diagnosis and delaying treatment. In particular, the endothelium is crucial in regulating a local balance between pro-inflammatory and anti-inflammatory mediators; under sepsis, endothelium undergoes excessive, sustained, and generalized activation,

resulting in unregulated expression of inflammation-associated products. Among these, adhesion molecule ICAM-1 has been implicated as a highly localized biomarker for inflammation induced under organ damage(160-162), one of the most significant mortality risks in septic patients(145). By specifically targeting ICAM-1 using bimodal LMN, we were able to readily differentiate septic and non-septic mice using optical imaging and quantitative MRI techniques, both non-invasive modalities. Most significantly, the observed differences were pronounced as soon as one hour after the treatment of the nanoparticle, and persist through at least 25 hours after injection. In this study, our temporal mapping of inflammation was focused on following nanoparticle distribution over 25 hours in mice exposed to LPS for 12 hours. However, as surface-expressed ICAM-1 is induced rapidly under inflammation, with some studies observing peak expression as quickly as 1-2 hours after the introduction of stimuli(158), additional information on spatiotemporal dynamics of inflammation can be obtained by subjecting mice to different durations of LPS while maintaining similar post-treatment imaging protocols. Such information on spatiotemporal dynamics of inflammation would be necessary to better understand the distinct yet common processes of inflammation in reticuloendothelial systems such as the liver and spleen.

This study also reveals the strength of MRI QSM in quantitatively measuring contrast agent localization into specific structures within the body. While optical imaging provides a gross view of the overall biodistribution of a fluorescent marker, the results are coarse, qualitative in nature, and prone to confounding effects due to the relatively shallow penetration depth of common fluorescent wavelengths, and the technique is not ideal for most clinical applications. Alternatively, traditional MRI techniques, such as typical T2* weighted imaging, provide significantly greater spatial resolution, but visualization is hindered by large obscuring signal voids resulting from SPIO use, and the resulting images are largely qualitative in nature, making it difficult to precisely estimate SPIO localization. In contrast,

QSM technique offers a quantitative, high resolution method of tracking the biodistribution of paramagnetic contrast agents to specific organs and structures through mapping of magnetic susceptibility, a physical property of paramagnetic materials that relates linearly to its concentration, allowing for direct determination of the amount and spatial location of contrast agent accumulation. Moreover, while SPIO-based contrast agents may result in signal voids in traditional T2* imaging and obscured underlying structure, QSM reconstruction techniques enable unimpeded analysis of the distribution of contrast agent and spatiotemporal mapping of inflammation. Given the speed and robustness by which these differences can be observed after administration of LMN, this technique offers temporal flexibility ideal for clinical applications, while granting dramatically increased spatial fidelity not offered by existing bulk measurement diagnostic techniques.

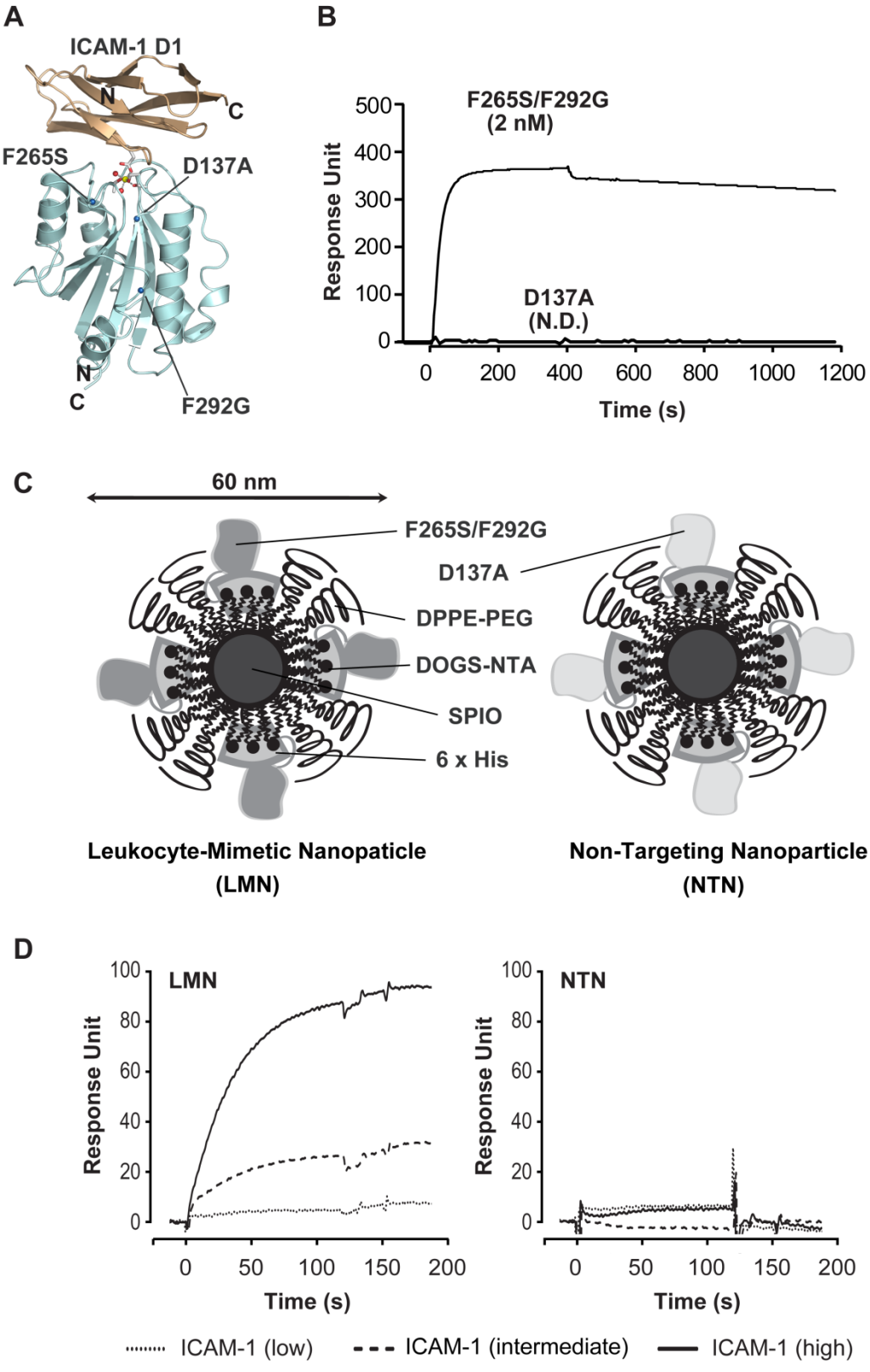
A
ICAM-1 D1
N
C
F265S
D137A
N
C
F292G
B
F265S/F292G
(2 nM)
Response Unit
500
400
300
200
100
0
D137A
(N.D.)
0
200
400
600
800
1000
1200
Time (s)
C
60 nm
F265S/F292G
D137A
DPPE-PEG
DOGS-NTA
SPIO
6 x His
Leukocyte-Mimetic Nanopaticle
(LMN)
Non-Targeting Nanoparticle
(NTN)
D
LMN
NTN
Response Unit
100
80
60
40
20
0
0
50
100
150
200
Time (s)
ICAM-1 (low)
ICAM-1 (intermediate)
ICAM-1 (high)

Figure 6.1. Construction of ICAM-1 specific leukocyte-mimetic nanoparticles. (A) Structural model of the complex of ICAM-1 domain 1 and LFA-1 I domain. White spheres depict allosteric activation sites along the peptide backbone. Metal ion and two oxygen atoms of water molecules are depicted as colored spheres. Residues that coordinate to the metal ion are shown as sticks. Mutations of Phe265->Ser (F265S), Phe292->Gly (F292G), and Asp137->Ala (D137A), and N and C termini are indicated. Figure adapted from Figure 5 of Hu et al(176). (B) SPR measurement of the binding kinetics of I domain variants F265S/F292G and D137A to immobilized murine ICAM-1. F265S/F292G exhibits high ICAM-1 binding affinity (K_D = 2 nM), while variant D137A indicates no (not determinable) binding affinity. (C) Schematic diagram of LMN and NTN. LMN (ICAM-1 specific) and NTN (non-ICAM-1 specific) differ only in surface-conjugated targeting moiety. (D) SPR measurement of the binding kinetics of LMN and NTN to varying concentrations of immobilized ICAM-1 (low, intermediate, and high correspond to approximately 200, 1000 and 3,250 molecules/μm^2, respectively). LMN binding was limited to the surface coating with higher than normal ICAM-1 site density, while LMN binding to the basal ICAM-1 surface was the same as the background levels seen with NTN.

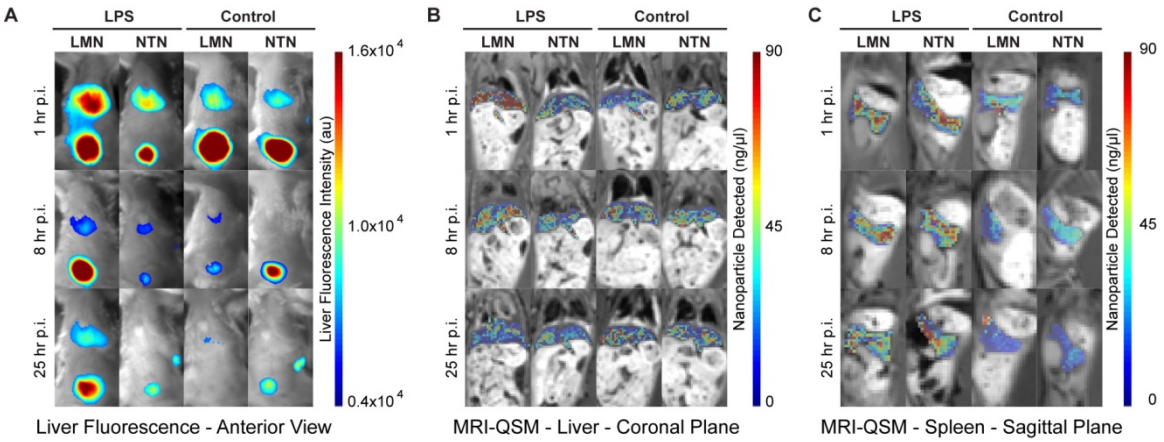

Figure 6.2. Representative images for each treatment regimen obtained using near-IR optical imaging and MRI QSM. (A) Fluorescent heat maps (color) are superimposed over brightfield images (grey scale), indicating greater nanoparticle localization in the liver in LPS/LMN-treated mice compared to that of negative controls, with observable localization diminishing over time. (B-C) MRI-QSM reconstructions of the (B) liver and (C) spleen. QSM technique reveals greater nanoparticle localization in the liver of LMN/LPS-treated mice compared to that of negative controls, while greater nanoparticle localization is observed in the spleen in LPS-treated mice, regardless of injected nanoparticle. Portions of these results were previously described in Chen et al(100), and reproduced here. Representative QSM maps at each time point post-injection (p.i.) of nanoparticles are shown: organ-specific QSM heat maps (color) are superimposed over MRI T2* weighted EFGRE scans used for navigational reference (gray).

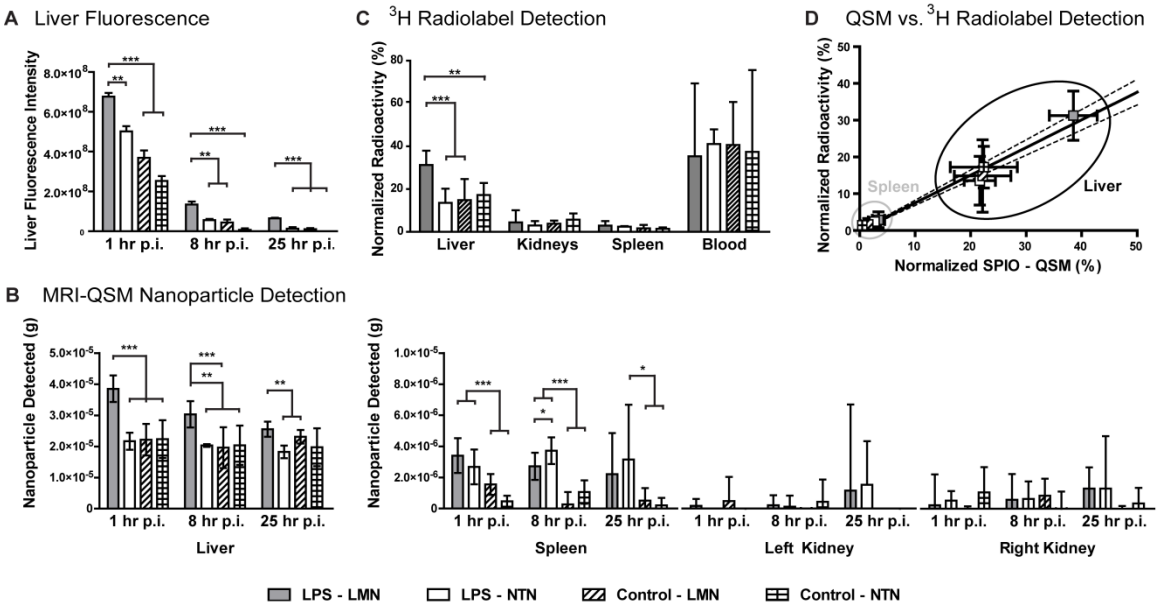
A Liver Fluorescence
Liver Fluorescence Intensity
1 hr p.i.
8 hr p.i.
25 hr p.i.
C 3H Radiolabel Detection
Normalized Radioactivity (%)
Liver
Kidneys
Spleen
Blood
D QSM vs. 3H Radiolabel Detection
Normalized Radioactivity (%)
Normalized SPIO - QSM (%)
Spleen
Liver
B MRI-QSM Nanoparticle Detection
Nanoparticle Detected (g)
Liver
Spleen
Left Kidney
Right Kidney
LPS - LMN
LPS - NTN
Control - LMN
Control - NTN

Figure 6.3. Multi-modal quantification of organ-specific nanoparticle localization. (A) Fluorescence detected in the liver region of mice analyzed using near-IR optical imaging at 1, 8, and 25 hours post nanoparticle injection. (B) Measurement of nanoparticle accumulation in the liver, spleen, and kidneys from MRI-QSM analysis. (C) Radioactivity measurement of ^{3}H labeled nanoparticles from the liver, kidney, spleen, and blood 1 hour post-nanoparticle injection, normalized to the total counts of radioisotope decay per mouse. All modalities measured high liver-specific nanoparticle localization in LPS/LMN-treated mice 1 hour post nanoparticle injection over controls. QSM measured high spleen-specific nanoparticle localization in LPS-treated mice, regardless of nanoparticle injected. Trends persist through 25 hours post nanoparticle injection. Portions of these results were previously described in Chen et al(100), and reproduced here. One-way analysis of variance with Tukey HSD post-test at 95% confidence interval are summarized in each figure (*** $p < 0.001$, ** $0.001 < p < 0.01$, * $0.01 < p < 0.05$). (D) Measurements of nanoparticles in the spleen and liver obtained from by radioisotope measurement and by QSM are linearly related. Error bars indicate 95% confidence interval. Dotted line indicates 95% confidence interval for linear regression fitting. n = 3 for each treatment and imaging regimen.

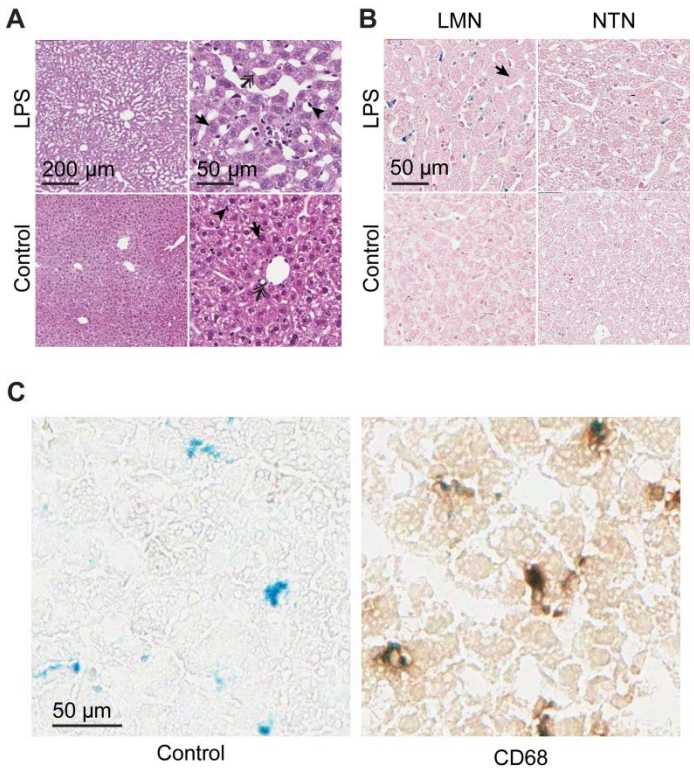

Figure 6.4. Histological sections of liver tissue. (A) H&E stain of liver tissue sections show distinct dilation of liver tissue, characteristic of sepsis. (B) Prussian Blue staining of liver tissue sections shows SPIO accumulation primarily in the endothelial cells and Kupffer cells, with markedly more staining in LPS treated subjects with injected LMN. (C) CD68 (brown) and Prussian Blue (blue) staining indicates primary localization of iron deposition in Kupffer cells. Examples of hepatocytes (arrow), endothelium (double headed arrow), and Kupffer cells (arrowhead) are marked.

Table 6.1. Two-way analysis of variance of organ-specific nanoparticle accumulation resulting from the treatment of LPS, the type of nanoparticle administered, or due to the interaction between both factors, quantified by QSM technique.

	Liver			Spleen			Right Kidney			Left Kidney		
Factors	1 hr	8 hr	25 hr	1 hr	8 hr	25 hr	1 hr	8 hr	25 hr	1 hr	8 hr	25 hr
LPS	***	**	ns	***	***	**	ns	ns	*	ns	ns	*
Nanoparticle	***	**	***	**	**	ns	ns	ns	ns	*	*	ns
Interaction	***	**	*	ns	ns	ns	ns	ns	ns	ns	*	ns

*** $p < 0.001$, ** $0.001 < p < 0.01$, * $0.01 < p < 0.05$, n.s. no significance.

A

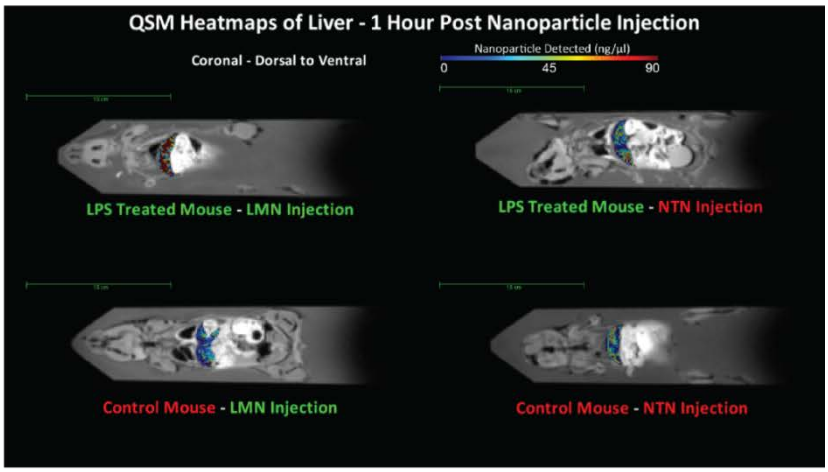
QSM Heatmaps of Liver - 1 Hour Post Nanoparticle Injection
Coronal - Dorsal to Ventral
Nanoparticle Detected (ng/µl)
0
45
90
LPS Treated Mouse - LMN Injection
LPS Treated Mouse - NTN Injection
Control Mouse - LMN Injection
Control Mouse - NTN Injection

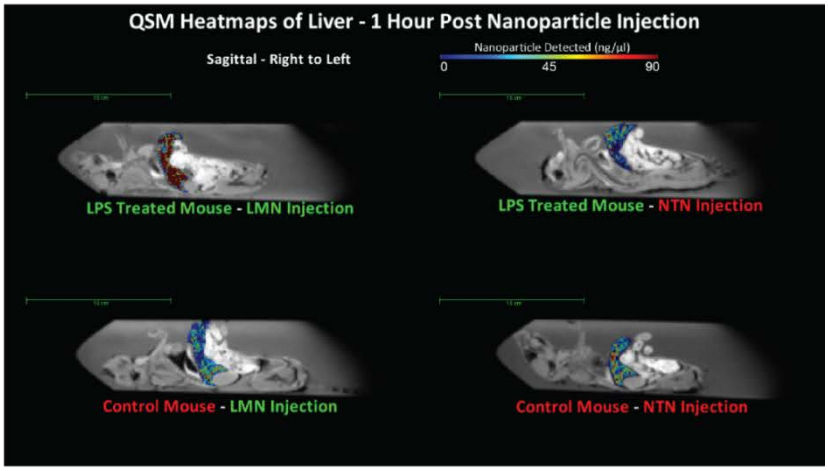
QSM Heatmaps of Liver - 1 Hour Post Nanoparticle Injection
Sagittal - Right to Left
Nanoparticle Detected (ng/µl)
0
45
90
LPS Treated Mouse - LMN Injection
LPS Treated Mouse - NTN Injection
Control Mouse - LMN Injection
Control Mouse - NTN Injection

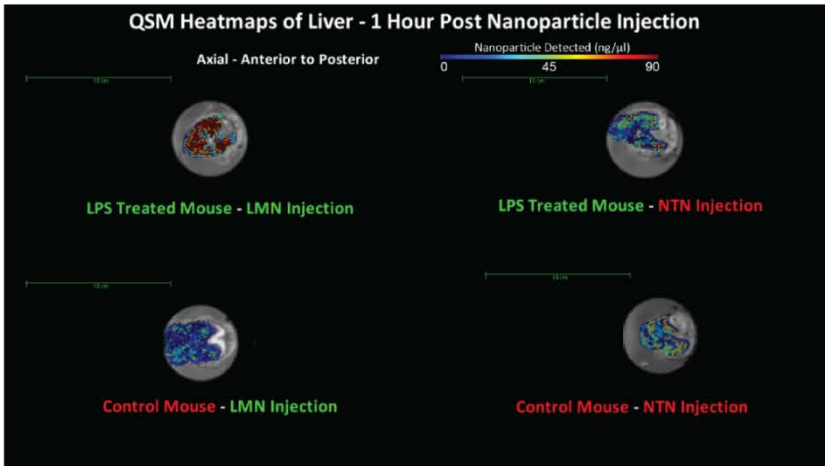
QSM Heatmaps of Liver - 1 Hour Post Nanoparticle Injection
Axial - Anterior to Posterior
Nanoparticle Detected (ng/µl)
0
45
90
LPS Treated Mouse - LMN Injection
LPS Treated Mouse - NTN Injection
Control Mouse - LMN Injection
Control Mouse - NTN Injection

Supplemental Figure 6.1 (continued)

B

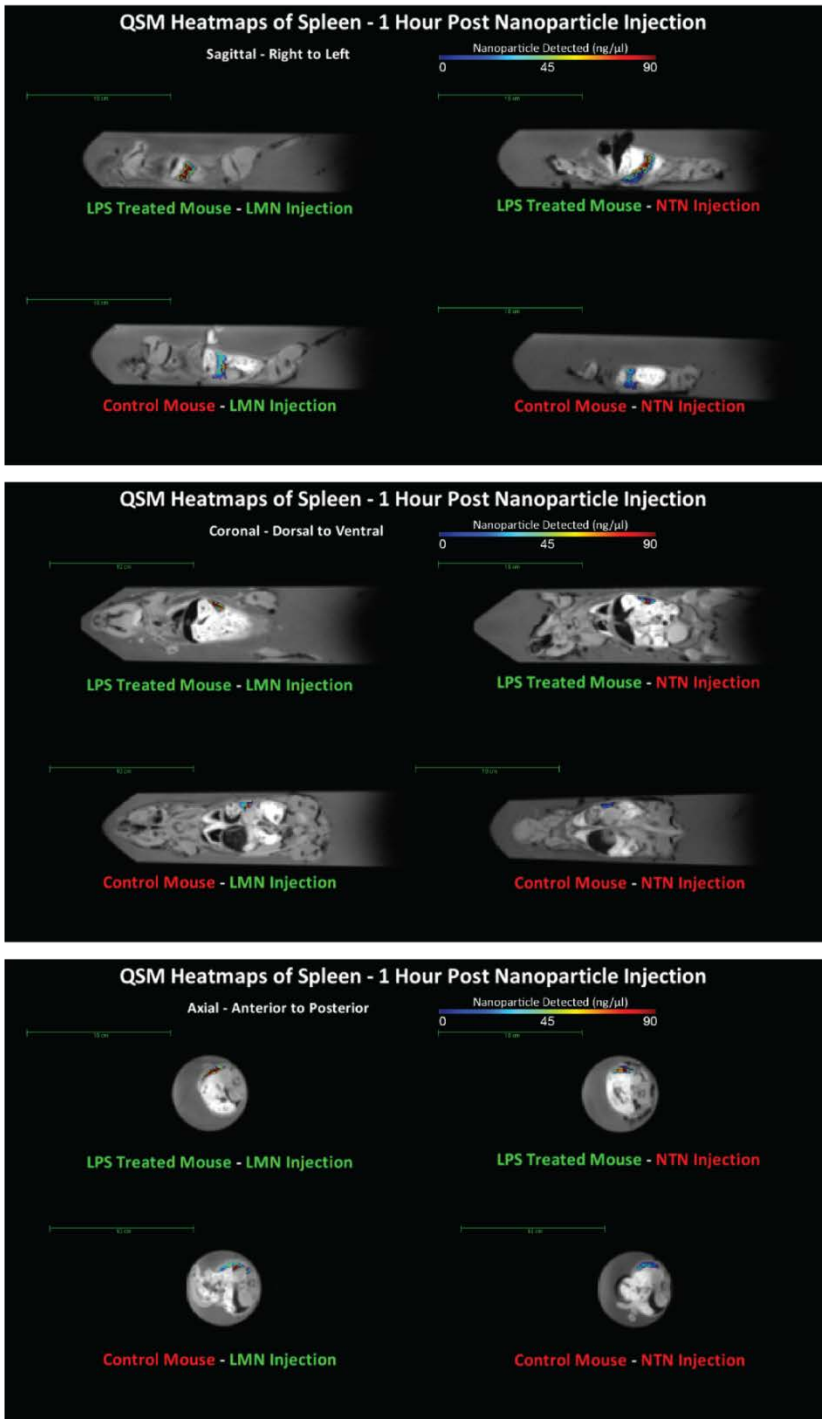

Supplemental Figure 6.1. Representative MRI and MRI QSM imaging slices of each treatment regime. Figure originally published as an electronic video and has been adapted to static formatting. The videos were constructed from representative images of each treatment regimen obtained using MRI QSM – (A) liver and (B) spleen. Representative QSM maps at 1 hour post-injection of nanoparticles are shown: organ-specific QSM heat maps (color) are superimposed onto MRI T2* weighted EFGRE scans used for navigational reference (gray).

CHAPTER 7 – GRADUATE STEM FELLOWS IN K-12 EDUCATION (GK-12) PROGRAM

7.1 INTRODUCTION

During the 2010-2011 academic year, I was a participant in Cornell's Learning Initiative in Medicine and Bioengineering (CLIMB) GK-12 program, an NSF funded program that partners graduate fellows in the field of Biomedical Engineering with science teachers in middle and high schools in districts around Ithaca. The aims of CLIMB are two-fold. First, graduate fellows provide teachers with in-class scientific support. By coordinating hands-on demonstrations, interactive labs, and inquiry-based lesson plan design, graduate fellows are able to provide students with a greatly enhanced learning experience through the introduction of modern scientific principles, applied in the classroom in a through a contextually relevant curriculum. By bridging the gap between academic research and classroom studies in an engaging, relevant, and approachable manner, CLIMB aims to give students a greater understanding of key scientific topics and instills a greater appreciation for science, mathematics, and engineering that will persist well after the lessons are complete. Second, CLIMB provides an opportunity for graduate fellows to improve upon personal communication skills necessary to convey scientific concepts to vastly differing demographics that are otherwise not accustomed to interacting with scientists and researchers on a regular basis.

7.2 CLASSROOM BACKGROUND

My work with the CLIMB program was conducted in partnership with Sydney Mendez, an educator from Nottingham High School in Syracuse, New York. During the 2010-2011 academic year, Sydney Mendez taught Syracuse University Project Advance (SUPA) Forensic Science. SUPA, a cooperative partnership between Syracuse University and local high schools, gives qualified high school students the opportunity to study college-level material while earning college course credit in a variety of disciplines. SUPA Forensic Science specifically focuses upon the application of scientific methods and techniques in the

context of criminal investigation and its implications on the criminal justice system. Students are provided with an introduction to the scientific principles between crime detection and analysis with an emphasis on topics such as organic and inorganic material analysis, fingerprinting, ballistic analysis, and blood typing. Conceptual lessons are supplemented with hands-on demonstrations, allowing students to experience first-hand the essential techniques used to process a crime scene. Student enrollment was approximately 60 students spread over two individual classes.

Nottingham High School is a public school in the Syracuse City School District. Enrollment totaled approximately 1300 students in grades 9-12 during the 2009-2010 academic year. (177) Four-year graduation rate was 51% among students who began high school in 2006, compared to the New York State average of 74%, and the Syracuse city average of 46%.(178) In 2009-2010, 59% of students scored at or above Level 3 on the State assessments in English Language Arts (ELA) and 59% in State assessments in mathematics at the secondary level; Level 3 is defined as performance demonstrating an understanding of the content expected in the subject and grade level. (177)

7.3 CURRICULUM DESIGN

The lesson plan (reproduced in Appendix) was used as a capstone laboratory demonstration and was designed to supplement the standard SUPA curriculum regarding blood analysis. This lab allows students to conduct blood analysis first hand in small groups, an opportunity that is typically not available in a high school environment.

This lesson plan was constructed using elements of inquiry-based learning. Students were allowed to conduct the experiment with fairly limited guidance and while a detailed list of procedures were given to the students to accurately run the experiment for themselves, very little information was on the interpretation of the result. Students were required to consider the results in the context of

what they had previously learned, as well as diagnose problems that they encountered, based on their understanding of the lab. Students were also asked to think about how the principles behind the laboratory demonstration can be translated from the classroom into the field of forensics, including any potential problems that could arise.

Each group of students was provided with a synthetically produced DNA "sample" obtained from a fictitious crime scene, as well as DNA samples from each of four "suspects." For the sake of simplicity, the DNA samples had been preamplified using PCR, leaving the students to digest each of the samples with a provided set of enzymes. The resulting digested samples were loaded into an electrophoresis gel and are allowed to separate by size. By comparing the sample bands to a standardized DNA ladder, students were able to visually assess the results of their work.

In addition to learning the physical technique involved in blood analysis during the course of a criminal investigation, students were asked to draw conclusion about the "guilt" of each suspect based on the results of the test. This was done without prior instruction on how to interpret the results, and required that the students come to a determination through an intuitive understanding of the assay. Students were also asked to identify weaknesses in the assay in its current implementation and suggest improvements to eliminate or mitigate these problems.

7.4 DISCUSSION

7.4.1 Planned Curriculum

The vast majority of students began the lesson with only a very basic conceptual understanding of DNA fingerprinting, and all lacked hands-on experience. Through an informal classroom discussion, it was found that while PCR and DNA fingerprinting had been discussed multiple times in the past in SUPA Forensic Science as well as Biology and Chemistry, students drew much of their knowledge of DNA

fingerprinting from popular media, most predominantly police procedural television dramas, such as *Law and Order* and *CSI*. Students readily understood DNA fingerprinting to be a powerful investigative tool, appreciated its relatively high accuracy at determining matching donors, and could identify potential weaknesses, such as "contamination," often used in popular media as plot devices. However, few students understood the scientific principles behind the technique and could not easily articulate why DNA fingerprinting was highly accurate, nor why contamination could affect the results of the analysis.

Without prior experience with items such as micropipettes and microcentrifuge tubes, students needed time to adapt to their usage. While instruction was given on general usage of the equipment and on the proper safety precautions, relatively little direction was given regarding minimization of cross-contamination. Instructors stressed the importance of using sterile, unused tips and tubes, but did not explain why this procedure was necessary.

Most groups successfully completed the lab and were able to determine the "guilty" suspect based on the unknown sample. Students were able to conceptually understand the process of DNA fingerprinting from the crime scene to the conclusion, most notably that enzymes could cleave DNA into fragments, but only at sequences specifically recognized by the enzyme. Students independently established that because each of the samples was potentially different from the rest, the enzymes would cut each DNA sample into different sized fragments. After realizing that an electrophoresis is capable of separating DNA fragments by size, students could very readily identify identical fragments and could easily match up the unknown DNA with one of the donors, thereby incriminating one of the "suspects."

Some groups were unable to find a match between the unknown and donor samples. Students were asked to consider why this could be the case, and came up with several possibilities: the criminal

was not among the suspects, the kit was defective, the enzymes were not working properly, the samples were mixed up with another group's samples, or the samples were contaminated with something else. When asked to elaborate on possible sources of contamination, many realized that if the samples were not properly isolated from each other, the results of the test were meaningless, even if all other procedures were performed correctly. Students were then able to trace by the cross-contamination to their pipette and sample separation technique, and were able to point out specific problems in their handling procedure. Ultimately, it was concluded that while the "criminal" was among the suspects, it was impossible to identify him using the results of the analysis. In a true criminal investigation, more evidence would have to be sought to order to draw an accurate conclusion.

After the completion of the lab, students were asked to share their thoughts on the accuracy of the test. Students quickly pointed out that contamination was a very serious issue that can seriously affect the results, and that contamination could occur at any point, from the crime scene to the testing lab. To ensure that the samples are properly obtained so that an accurate result can be determined, they concluded that it was essential that all people associated with the sample be properly trained, and that a clear chain of custody needed to be established so that the samples would not be tampered with, either accidentally or intentionally.

Students also pointed out that while the DNA fingerprinting technique was exceptionally good at finding matching samples, the presence of a matching sample at a crime scene does not necessarily indicate guilt. As there may be many reasons why a DNA sample was at the scene, they acknowledged that the results of DNA analysis need to be considered in conjunction with other evidence at the scene. Ultimately, students concluded that DNA fingerprinting, like older forms of investigative techniques, such as fingerprinting, were simply tools for the investigator and were not meant to be construed as absolute evidence of innocence or guilt.

7.4.2 Inquiry-Based Teaching

Inquiry-based learning requires that the students be given adequate background on a topic so that they can largely self-direct their own lines of inquiry, while being given freedom to fully pursue these avenues of exploration. (179) Teaching science as inquiry begins by giving students the knowledge base and the freedom necessary to explore the underlying mechanisms of scientific phenomena. It allows students to actively direct their own research in a meaningful manner and allows for students to self-discover possible solutions to organically identified problems. This laboratory demonstration was designed with these goals in mind. Students were given the tools and sufficient background information to become immersed in the presented scenario, and were tasked with not only solving the immediately obvious problem of identifying the guilty subject, but were also encouraged to find limitations and potential pitfalls during the entire process. This constant reflection and self-assessment is paramount in teaching critical thinking skills that are necessary for criminal investigators, as well as in any other field that stresses analytical thinking and problem solving.

While this approach certainly has benefits that cannot be easily paralleled by traditional, lecture-based teaching methods, there are also several major limitations that preclude its exclusive use in a classroom environment. Most prominent is the modern school system's reliance on standardized tests for the broad evaluation of student, teacher, and school system performance. In New York State, a series of such tests is administered to students from grades 3-8 in the subjects of Mathematics, English, and Science, and in grades 9-12 in the subjects of English, Mathematics, Science, and Social Studies, known as the Regents Exams. (180) These exams stress the fundamentals of each discipline and aim to assess a student's mastery against specific learning standards established by the New York State Education Department (NYSED). As students are required to demonstrate sufficient mastery of a

minimum number of subjects, quantifiably measured by a passing a specified number of Regents exams, successful completion of high school must, in part, consist of satisfactory performance on these standardized tests. In turn, the professional performance of teachers, education administrators, and school districts, of which graduate rate is a major metric, is likewise highly dependent on the results of the Reagents exam. Conceived as both a tool for political and educational accountability, as well as a measuring stick by which individual students can quantitatively assess their own understanding of core disciplines, the Regents Exam has become central to the education process, and directly influences matters of funding, policy, and rhetoric. (181)

A typical Regents Exam in science consists of a multiple choice section and a short answer section that highly emphasizes the core knowledge-based principles of the subject. In chemistry, for example, students are asked to be familiar with atomic concepts, the periodic table, stoichiometry, chemical bonding, kinetics, equilibrium, organic chemistry, oxidation-reduction, acids/bases/salts, as well as nuclear chemistry.(182) While testing these topics is critical in fully assessing students' understanding of chemistry, the topics and the test format do not lend themselves easily to assessing the free-form problem solving ability essential to becoming a successful researcher, and cultivated by many inquiry-based teaching techniques. In fact, given the composition of the exam, consisting highly directed prompts with unequivocally correct solutions meant to provide graders with an objective means of evaluation, students are better served avoiding much of the techniques learned through inquiry-based teaching in favor of rote memory or highly drilled procedural techniques.(183) Unfortunately, due to the dominance of standardized test-driven school systems and the direct monetary incentive for succeeding in quantifiable measures, inquiry based learning may often have a tangible detrimental effect if applied too liberally, both on the students as well as the teachers.

Likewise, it is realistically not sustainable to apply inquiry-based techniques wholesale in every lesson plan, as inquiry based techniques must be implemented in moderation to maintain direction, organization, and continuity in a practical classroom setting. Inquiry-based teaching, by design, encourages organic problem discovery and problem solving by each student with relatively little direction. The success of this technique relies heavily on a carefully constructed curriculum, but is also greatly affected by the often-tangential "brainstorming" nature of free-form discovery. Students must be reined in by their instructors in order to achieve certain goals, while doing so under time restrictions imposed by daily and annual class schedules. Moreover, students' progress is also affected by their interest level, which can fluctuate quickly depending on the perceived success or failure of their current path of reasoning. To mitigate all of these potential factors, there is little alternative for an instructor but to step in and provide guidance, at the expense of student-driven self-discovery. In practice, I have found that frequent "interventions" are paramount in ensuring that the students derive anything of value from each lesson plan.

Ultimately, inquiry-based teaching is a powerful technique that encourages students to engage activity in their learning, as well as fosters many important problem solving skills that can be translated into a wide variety of research and non-academic career paths, but must be used in the moderation in the modern school system in which standardized accountability and metrics-based evaluation is predominant.

CHAPTER 8 – CONCLUSIONS AND FUTURE DIRECTION

8.1 FUTURE DIRECTION

8.1.1 Targeted Contrast Agents *In Vivo*

While exploring new uses and indications for already-existing, clinically approved contrast agents is undoubtedly the quickest path to translate bench research to the clinic, approaches using surface-bound ligands to create novel targeted contrast agents are potentially more powerful in expanding the capabilities of contrast agents in visualizing a wide variety of disease states. In this thesis, two such constructs were described. An anti-p53 SPIO was tested against *in vitro* cancer cell models, and a leukocyte mimetic nanoparticle was tested against *in vivo* mouse models and imaged post mortem. In both cases, the targeted contrast agent was capable of readily differentiating between the disease state of interest and a healthy control. Thus, the next steps would be to expand the scope of these studies to *in vivo* mouse models with live mouse imaging using MRI. This presents many challenges, particularly with imaging. Thus far, *in vivo* imaging was performed post mortem, and concerns such as time constraints and motion due to breathing or heart beat could be disregarded. Likewise, as the mice were preserved and imaged post mortem, the analysis was that of a static subject that was no longer undergoing active change. For live animal imaging, all of these new concerns must be addressed such that sufficient signal can be obtained from the subject, at a temporal resolution relevant for visualizing an actively changing phenomenon, while minimizing the deleterious imaging effects inherent with imaging living and involuntarily moving subjects.

Preliminary studies were conducted concerning the feasibility of live mouse imaging in conjunction with the administration of targeted nanoparticles. Initial results suggest that areas of the body not highly susceptible to involuntary motion, notably the brain, can be effectively imaged and analyzed using MRI-QSM techniques, suggesting that it is possible to quantitatively track nanoparticles delivered to areas of acute inflammation in the brain. Imaging inflammation in the brain has particular

clinical significance, such as for the diagnosis of multiple sclerosis. Multiple sclerosis is a disease of the central nervous system that is characterized by multifocal white matter lesions. (184) Current methods of diagnoses rely on the detection of the lesions using traditional MRI techniques, and utilize non-specific gadolinium-based contrast agents to differentiate lesions from surrounding healthy tissue. (185) However, such an approach images only downstream injuries, indicated of advanced pathology, and cannot accurately assess disease activity. (186) While typically not present to a large degree in the tissue of the CNS, ICAM-1 plays a key role in lymphocytic infiltration and interactions during tissue inflammation and is expressed at significantly higher levels in multiple sclerosis lesions of all ages and degree advancement. (187) Thus, a method of non-invasively visualizing areas of high ICAM-1 expression in the brain could prove valuable in the early and accurate diagnosis of multiple sclerosis.

8.1.2 Constructing and Tracking Theranostic Nanoparticle

As a long term goal, the studies described in this thesis suggest that MRI-QSM can be used to track and quantify the distribution of theranostic nanoparticles, complexes that contain a combination of components suitable as a contrast agent and components suitable as a therapeutic agent. In doing so, it would be feasible to non-invasively quantitate the amount of therapeutic agents delivered to specific areas of the body with high spatiotemporal resolution. Such an application has far reaching implications for both investigational research, as well as clinical treatment, and would allow investigators and clinicians to more accurately understand the spatiotemporal distribution of therapeutic agents. Likewise, this would vastly improve the ability to titrate therapeutic doses on a per patient basis, thereby improving treatment effectiveness while reducing side effects from over-administration. Ultimately, such a technique would pave way to “concierge” medicine, allowing clinicians to accurately tailor treatment protocols to the unique needs of each patient.

8.2 CONCLUSIONS

In this thesis, two distinct strategies were described to deliver and quantifiably track contrast agents in MRI for the purposes of visualizing underlying disease states. First, clinically approved non-biospecific nanoparticles were used to probe the onset and progression of induced systemic inflammation in *in vivo* mouse models, allowing for clinically relevant rapid differentiation of inflamed mice from healthy controls based on the rate of nanoparticle uptake by activated immune cells. Second, targeted nanoparticles were constructed to specifically deliver contrast agents to sites with cellular targets closed associated with acute inflammation, sepsis, or cancer. A first approach employed the development of a bivalent protein scaffold platform, resulting in increased effective binding affinity of targeting ligands through an increase in avidity or a broadened spectrum of recognition through the formation of heterogeneous dimers. This platform was utilized in the formation of mutated p53-specific contrast agents, resulting in a generalized cancer-specific contrast agent suitable for selective enhancement of a wide variety of tumor cell lines. A second approach resulted in the formation of ICAM-1-specific contrast agents, resulting in a contrast agent suitable for selective imaging enhancement of regions of acute inflammation. In both strategies, contrast agents were tracked using MRI-QSM, a relatively new technique that allows for accurate and quantitative spatiotemporal analysis not feasible with traditional MRI-based imaging and analysis.

MRI is a powerful technique that is commonly used in clinical settings. It is non-invasive, does not employ ionizing radiation, and is capable of high spatial and temporal resolution, making it ideal for a wide variety of imaging applications, both for active diagnostic applications and preventative medicine. The strategies described in this thesis further increase the diagnostic ability of MRI by selectively delivering contrast enhancing nanoparticles to areas of interest, either through changes in

cellular, organ, and systemic behavior as a result of disease states, or through biospecificity conferred by surface-bound targeting ligands. In doing so, this allows MRI to accurately probe systemic processes or cellular targets previously not available as diagnostic indicators, and has the potential to dramatically expand the spectrum of biological characteristics that can be visualized and quantified using MRI. The work in this study represents a step towards the creation of specialized, use-specific diagnostic agents that have the potential to improve the accuracy and speed of clinical diagnoses.

APPENDIX

GK-12 LESSON PLAN

DNA Fingerprinting in the Context of Criminal Forensics

Author(s):	Richard Wong
Date Created:	2011
Subject:	Forensics
Grade Level:	High School
Standards:	Standard 1: Inquiry and Design Standard 4.2.1: Genetics
Schedule:	3 Days (1 Day Overview, 2 Day Lab, 45 minutes per day)

Description:

Students will learn about DNA fingerprinting and its usefulness in the context of criminal forensics. Students will use basic DNA fingerprinting techniques to solve a "crime" in which DNA evidence is present.

Objectives:

- Understand basic scientific concepts of DNA fingerprinting
- Understand basic protocol for DNA fingerprinting
- Understand proper handling techniques to avoid contamination
- Interpret results in the context of criminal investigations

Vocabulary:

- DNA Fingerprinting
- PCR
- Electrophoresis
- Restriction Enzymes

Materials:

- Biorad Biotechnology Explorer – Forensic DNA Fingerprinting Kit Cat #166-0007EDU (one kit supplies about 15 groups)
- Micropipetters (20uL and 200uL)
- Gel Electrophoresis Chambers
- Gel Electrophoresis Power Supplies
- Microwave
- Gloves
- Goggles
- Heat protective gloves
- Lab coats
- Beakers – 500ml
- Bucket with Ice

Safety:

Student should use gloves. Goggles and heat-protective gloves should be used when preparing agarose gels. Lab coats should be worn at all times.

Science Content for the Teacher:

DNA fingerprinting is a common technique used for linking genetic material found at crime scenes with genetic material obtained from suspects. While DNA fingerprinting techniques have existing in some form since the 1980s, current techniques utilize polymerase chain reaction (PCR) amplification to rapidly and accurately analyze small amounts of DNA material.

PCR: Polymerase chain reaction amplification is a technique that amplifies a single or few copies of DNA across several orders of magnitude, allowing for small quantities of DNA found at a crime scene to be analyzed easily. Conceptually, PCR replies on thermal cycling of DNA in which cycles of heating and cooling allow for phased DNA melting and subsequent enzymatic replication. The first step, the denaturation phase, consists of heating the reaction to 94-98C for 20-30 seconds, causing DNA melting through the disruption of hydrogen bonds between complementary bases, resulting in single stranded DNA. The second step, the annealing phase consists of cooling the temperature to 50-65C for 20-40, allowing for DNA to anneal to **primers**. The polymerase binds to the primer-DNA and begins synthesis. The third step, the extension phase, consists of raising the temperature to the **DNA polymerases'** optimal temperature, and DNA is synthesized complementary to the DNA template. The steps can be repeated to increase the number of DNA twofold for each cycle. During this process, DNA can be "cut" and specific sequences can be selectively amplified through the use of **restriction enzymes.**

Primers: Because DNA polymerases can only add new nucleotides to an existing strand of DNA, a "primer" must be used as a starting point for DNA synthesis. A primer consists of a short strand of nucleic acids that is complementary to a sequence of DNA. As DNA synthesis progresses, the primer is elongated into a full strand.

DNA Polymerase: DNA polymerase is an enzyme that helps catalyze the polymerization of deoxyribonucleotides into a DNA strand. Conceptually, DNA polymerases "read" a complete DNA strand

and append the complementary bases onto a partner strand, creating a full double-stranded DNA strand with complementary base pairs.

Restriction Enzymes: Restriction enzymes are enzymes that cuts double or single stranded DNA at specific recognition nucleotide sequences, known as the restriction sites. By using restriction enzymes, it becomes possible to selectively "cut" DNA, resulting in multiple fragments of varying sizes. If restriction enzymes are carefully chosen, the differences in DNA fragments resulting from the cuts can give information that can be used to differentiate between multiple unknown samples. Identical DNA fragments may indicate that the DNA samples may have originated from the same source.

Electrophoresis: Electrophoresis is a common laboratory technique by which DNA fragments are separated by size. DNA fragments are loaded into an agarose gel slab and placed into a chamber with a conductive buffer solution. A current is passed between electrodes at each end of the chamber. Since DNA is negatively charged, DNA will migrate towards the positive electrode, through the agarose. The agarose impedes the progression of DNA, acting as a sieve, and allowing small fragments to travel faster. Over time, smaller DNA fragments will be closer to the positive electrode, and larger fragments will be closer to the negative electrode.

DNA Fingerprinting: DNA fingerprinting uses the combination PCR, carefully chosen restriction enzymes, and electrophoresis, to determine the similarities and differences between DNA strands. In the context of criminal forensics, a small amount of DNA is obtained at a crime scene and is amplified dramatically using PCR. The resulting DNA is also cut using restriction enzymes aimed at differentially cutting DNA sequences into fragments of various sizes, and the results are analyzed using electrophoresis. If differences in DNA fragment sizes are detected using electrophoresis, one can conclude that the samples are dissimilar, and may suggest that they are from different sources. If there are no differences in DNA fragment sizes, this may suggest that they are from the same source, or that

the restriction enzymes did not cut the sequence in a manner that differentiates between the two sources.

Classroom Procedure:

Overview

The teacher provides an overview of DNA fingerprinting in the context of criminal forensics. Topics should include DNA and its makeup, PCR, restriction enzymes, and electrophoresis. The above material can be used as a starting point for an overview lecture.

Preparation (Before Students Arrive): 30 minutes

Rehydrate DNA samples, enzymes, and mixes included in kit, according to directions listed in the kit.

Day One: 45 minute class session – Restriction Digestion

For the sake of simplicity in a high school laboratory environment, the samples in the included kit have already been pre-amplified using PCR. It may be beneficial for the instructor to explain the significance of the pre-amplification in order for students to understand the procedural chain between obtaining a DNA sample from a crime scene and analyzing the sample using the amplified materials.

1. The students are given 10uL of each of the suspects' DNA in individual microcentrifuge tubes. They are also given a tube containing 10uL of an unknown DNA sequence from a fictitious crime scene, which must be matched to one of the five suspect's samples. 10uL of a restriction enzyme mix is also given to each in separate tube.

2. The students will add 10uL of the enzyme mix to each of the sample tubes, mixing well by pipetting up and down.
3. The caps for each sample are closed and the contexts are mixed by flicking the tubes gently with a finger.
4. Tubes are incubated overnight at room temperature.
5. Gels are prepared for the following day.
    a. Create a 1% agarose solution using 1 gram of agarose for each 100mL of 1X TAE electrophoresis buffer. Add beaker.
    b. Boil agarose in a microwave. Time varies, but should be roughly 3 minutes at medium power, depending on the amount of agarose used. **Caution must be used, as agarose is very hot.**
    c. Seal ends of electrophoresis chamber and pour gel into mold to create agarose slabs. Insert a comb to create a parallel row of sample wells.
    d. Allow to cool. Gels will be kept until the following day in a refrigerator.

Day Two: 45 minute class session – Electrophoresis

1. Tap DNA tubes (with added enzymes) on table to bring all liquid to the bottom of the tubes.
2. Using a separate tip, add 5uL of loading dye into each tube. Close tubes and mix gently.
3. Place prepared agarose gels in electrophoresis chamber and all 1X TAE buffer to over the gel. Ensure that the top of the gel (with the wells) is by the negative electrode, and that the bottom of the gel is by the positive electrode.
4. Using a separate tip for each sample, load the indicated volume of each sample into the wells in the following order:

a. Lane 1: DNA size standard (include) – 10uL
b. Lane 2: Unknown Crime Scene sample – 20uL
c. Lane 3: Suspect Sample 1 – 20uL
d. Lane 4: Suspect Sample 2 – 20uL
e. Lane 5: Suspect Sample 3 – 20uL
f. Lane 6: Suspect Sample 4 – 20uL
g. Lane 7: Suspect Sample 5 – 20uL

5. Plug power supply leads electrophoresis chamber and run power supply at 100V for about 30 minutes.
6. Stain DNA using Fast Blast DNA
    a. Add 120mL of 100x Fast Blast DNA stain into staining tray
    b. Stain the gels for 2 minutes with gentle agitation. Stain can be reused.
    c. Transfer gels to large washing container and rinse with warm (40-55C) tap water for 10 seconds.
    d. Destain by washing twice in warm tap water for 5 minutes with gentle shaking
7. Observe results and discuss. Which suspect's sample matches that found at the crime scene?

Assessment:

While the primary focus of this lab is to provide a basic overview of a simple DNA fingerprinting protocol and to give the student hands-on interaction with the process of cutting and analyzing DNA samples, it also encourages students to think about DNA fingerprinting as an evidence processing technique in the context of a criminal investigation. In particular, while the successful completion of this

lab results in a visual separation of DNA and allows for an unknown sample to be matched with one of an array of suspect samples, it is important for students to understand the implications of this match.

Useful questions to ask:

- Which samples matches the one found at the crime scene? What would this mean in a criminal investigation?
- What if none of the samples matched the one at the crime scene? What would this mean in a criminal investigation?
- What if two or more samples matched the one at the crime scene? What would this mean in a criminal investigation?
- What would happen if the samples were contaminated? What would the results of electrophoresis show? What would this mean in a criminal investigation?
- What are some of the limitations of this technique?
    - Can a crime scene sample be matched to any unknown person?
    - Is one restriction enzyme enough to differentiate between every suspect?
    - Is it possible for more than one person have similar electrophoresis results? Why?

Acknowledgements:

Lesson adapted from BioRad's Biotechnology Explorer Forensic DNA Fingerprinting Kit.

REFERENCES

1. Lanza GM, Abendschein DR, Yu X, Winter PM, Karukstis KK, Scott MJ, et al. Molecular imaging and targeted drug delivery with a novel, ligand-directed paramagnetic nanoparticle technology. Academic radiology. 2002;9 Suppl 2:S330-1.

2. Winter PM, Caruthers SD, Yu X, Song SK, Chen J, Miller B, et al. Improved molecular imaging contrast agent for detection of human thrombus. Magn Reson Med. 2003;50(2):411-6.

3. Amirbekian V, Lipinski MJ, Briley-Saebo KC, Amirbekian S, Aguinaldo JG, Weinreb DB, et al. Detecting and assessing macrophages in vivo to evaluate atherosclerosis noninvasively using molecular MRI. Proceedings of the National Academy of Sciences of the United States of America. 2007;104(3):961-6.

4. Lipinski MJ, Amirbekian V, Frias JC, Aguinaldo JG, Mani V, Briley-Saebo KC, et al. MRI to detect atherosclerosis with gadolinium-containing immunomicelles targeting the macrophage scavenger receptor. Magn Reson Med. 2006;56(3):601-10.

5. Frias JC, Williams KJ, Fisher EA, Fayad ZA. Recombinant HDL-like nanoparticles: a specific contrast agent for MRI of atherosclerotic plaques. Journal of the American Chemical Society. 2004;126(50):16316-7.

6. Shen T, Weissleder R, Papisov M, Bogdanov A, Jr., Brady TJ. Monocrystalline iron oxide nanocompounds (MION): physicochemical properties. Magn Reson Med. 1993;29(5):599-604.

7. Wunderbaldinger P, Josephson L, Weissleder R. Crosslinked iron oxides (CLIO): a new platform for the development of targeted MR contrast agents. Academic radiology. 2002;9 Suppl 2:S304-6.

8. Harisinghani MG, Jhaveri KS, Weissleder R, Schima W, Saini S, Hahn PF, et al. MRI contrast agents for evaluating focal hepatic lesions. Clinical radiology. 2001;56(9):714-25.

9. Harisinghani MG, Barentsz J, Hahn PF, Deserno WM, Tabatabaei S, van de Kaa CH, et al. Noninvasive detection of clinically occult lymph-node metastases in prostate cancer. The New England journal of medicine. 2003;348(25):2491-9.

10. Dunn EA, Weaver LC, Dekaban GA, Foster PJ. Cellular imaging of inflammation after experimental spinal cord injury. Mol Imaging. 2005;4(1):53-62.

11. Turvey SE, Swart E, Denis MC, Mahmood U, Benoist C, Weissleder R, et al. Noninvasive imaging of pancreatic inflammation and its reversal in type 1 diabetes. The Journal of clinical investigation. 2005;115(9):2454-61.

12. Kraitchman DL, Heldman AW, Atalar E, Amado LC, Martin BJ, Pittenger MF, et al. In vivo magnetic resonance imaging of mesenchymal stem cells in myocardial infarction. Circulation. 2003;107(18):2290-3.

13. Lewin M, Carlesso N, Tung CH, Tang XW, Cory D, Scadden DT, et al. Tat peptide-derivatized magnetic nanoparticles allow in vivo tracking and recovery of progenitor cells. Nature biotechnology. 2000;18(4):410-4.

14. Hill JM, Dick AJ, Raman VK, Thompson RB, Yu ZX, Hinds KA, et al. Serial cardiac magnetic resonance imaging of injected mesenchymal stem cells. Circulation. 2003;108(8):1009-14.

15. Frank JA, Zywicke H, Jordan EK, Mitchell J, Lewis BK, Miller B, et al. Magnetic intracellular labeling of mammalian cells by combining (FDA-approved) superparamagnetic iron oxide MR contrast agents and commonly used transfection agents. Academic radiology. 2002;9 Suppl 2:S484-7.

16. Arbab AS, Yocum GT, Kalish H, Jordan EK, Anderson SA, Khakoo AY, et al. Efficient magnetic cell labeling with protamine sulfate complexed to ferumoxides for cellular MRI. Blood. 2004;104(4):1217-23.

17. SH Gregory EW. Neutrophil-Kupffer cell interaction: a critical component of host defenses to systemic bacterial infections. J Leukoc Biol. 2002;72:239-48.

18. Liu T, Spincemaille P, de Rochefort L, Kressler B, Wang Y. Calculation of susceptibility through multiple orientation sampling (COSMOS): a method for conditioning the inverse problem from measured magnetic field map to susceptibility source image in MRI. Magn Reson Med. 2009;61(1):196-204.

19. Demmel JW. The Smallest Perturbation of a Submatrix Which Lowers the Rank and Constrained Total Least-Squares Problems. Siam J Numer Anal. 1987;24(1):199-206.

20. Liu T, Liu J, de Rochefort L, Spincemaille P, Khalidov I, Ledoux JR, et al. Morphology enabled dipole inversion (MEDI) from a single-angle acquisition: comparison with COSMOS in human brain imaging. Magn Reson Med. 2011;66(3):777-83.

21. Wong R, Shou J, Wang Y. Probing sepsis and sepsis-like conditions using untargeted SPIO nanoparticles. Conf Proc IEEE Eng Med Biol Soc. 2010;2010:3053-6.

22. Angus DC L-ZW, LidickerJ, et al. Epidemiology of severe sepsis in the United States: analysis of incidence, outcome, and associated cost of care. Critical Care Med. 2001;29:1303-10.

23. Ware LB, Matthay MA. The acute respiratory distress syndrome. The New England journal of medicine. 2000;342(18):1334-49.

24. Esper AM, Martin GS. Evolution of treatments for patients with acute lung injury. Expert Opin Investig Drugs. 2005;14(5):633-45.

25. Ventilation with lower tidal volumes as compared with traditional tidal volumes for acute lung injury and the acute respiratory distress syndrome. The Acute Respiratory Distress Syndrome Network. The New England journal of medicine. 2000;342(18):1301-8.

26. Stapleton RD, Wang BM, Hudson LD, Rubenfeld GD, Caldwell ES, Steinberg KP. Causes and timing of death in patients with ARDS. Chest. 2005;128(2):525-32.

27. Angus DC, Linde-Zwirble WT, Lidicker J, Clermont G, Carcillo J, Pinsky MR. Epidemiology of severe sepsis in the United States: analysis of incidence, outcome, and associated costs of care. Crit Care Med. 2001;29(7):1303-10.

28. Bernard AWaG. Treating Patients with Severe Sepsis. The New England journal of medicine. 1999;340(3):207-14.

29. K Hoshino OT, T Kawai, H Sanjo, T Ogawa, Y Takeda, K Takeda, and S Akira. Cutting Edge: Toll-Like Receptor 4 (TLR4)-Deficient Mice Are Hyporesponsive to Lipopolysaccharide: Evidence for TLR4 as the Lps Gene Product. The Journal of Immunology. 1999;162:3749-52.

30. Fujii H, Yoshikawa K, Berliner LJ. In vivo fate of superparamagnetic iron oxides during sepsis. Magn Reson Imaging. 2002;20(3):271-6.

31. Raynal I, Prigent P, Peyramaure S, Najid A, Rebuzzi C, Corot C. Macrophage endocytosis of superparamagnetic iron oxide nanoparticles: mechanisms and comparison of ferumoxides and ferumoxtran-10. Invest Radiol. 2004;39(1):56-63.

32. Schmidt HH, Warner TD, Nakane M, Forstermann U, Murad F. Regulation and subcellular location of nitrogen oxide synthases in RAW264.7 macrophages. Mol Pharmacol. 1992;41(4):615-24.

33. Wong RL, Liu B, Zhu X, You L, Kong L, Han KP, et al. Interleukin-15:Interleukin-15 receptor alpha scaffold for creation of multivalent targeted immune molecules. Protein Eng Des Sel. 2011;24(4):373-83. PMCID: 3049345.

34. Kouzarides T, Ziff E. The role of the leucine zipper in the fos-jun interaction. Nature. 1988;336(6200):646-51.

35. Rieker JD, Hu JC. Molecular applications of fusions to leucine zippers. Methods Enzymol. 2000;328:282-96.

36. Stern LJ, Wiley DC. The human class II MHC protein HLA-DR1 assembles as empty alpha beta heterodimers in the absence of antigenic peptide. Cell. 1992;68(3):465-77.

37. Sloan VS, Cameron P, Porter G, Gammon M, Amaya M, Mellins E, et al. Mediation by HLA-DM of dissociation of peptides from HLA-DR. Nature. 1995;375(6534):802-6.

38. de Kruif J, Logtenberg T. Leucine Zipper Dimerized Bivalent and Bispecific scFv Antibodies from a Semi-synthetic Antibody Phage Display Library. Journal of Biological Chemistry. 1996;271(13):7630-4.

39. Kostelny S, Cole M, Tso J. Formation of a bispecific antibody by the use of leucine zippers. J Immunol. 1992;148(5):1547-53.

40. Holliger P, Hudson PJ. Engineered antibody fragments and the rise of single domains. Nature biotechnology. 2005;23(9):1126-36.

41. Hayden-Ledbetter MS, Cerveny CG, Espling E, Brady WA, Grosmaire LS, Tan P, et al. CD20-Directed Small Modular Immunopharmaceutical, TRU-015, Depletes Normal and Malignant B Cells. Clinical Cancer Research. 2009;15(8):2739-46.

42. Kubetzko S, Balic E, Waibel R, Zangemeister-Wittke U, Pluckthun A. PEGylation and multimerization of the anti-p185HER-2 single chain Fv fragment 4D5: effects on tumor targeting. J Biol Chem. 2006;281(46):35186-201.

43. Cuesta AM, Sanchez-Martin D, Sanz L, Bonet J, Compte M, Kremer L, et al. In vivo tumor targeting and imaging with engineered trivalent antibody fragments containing collagen-derived sequences. PLoS One. 2009;4(4):e5381.

44. Mohler K, Torrance D, Smith C, Goodwin R, Stremler K, Fung V, et al. Soluble tumor necrosis factor (TNF) receptors are effective therapeutic agents in lethal endotoxemia and function simultaneously as both TNF carriers and TNF antagonists. J Immunol. 1993;151(3):1548-61.

45. Nimmerjahn F, Ravetch JV. Fcgamma receptors as regulators of immune responses. Nat Rev Immunol. 2008;8(1):34-47.

46. Weiner LM. Building better magic bullets--improving unconjugated monoclonal antibody therapy for cancer. Nat Rev Cancer. 2007;7(9):701-6.

47. Shen J, Vil MD, Jimenez X, Iacolina M, Zhang H, Zhu Z. Single variable domain-IgG fusion. A novel recombinant approach to Fc domain-containing bispecific antibodies. J Biol Chem. 2006;281(16):10706-14.

48. Lu D, Zhu Z. Construction and production of an IgG-like tetravalent bispecific antibody for enhanced therapeutic efficacy. Methods Mol Biol. 2009;525:377-404, xiv.

49. Baeuerle PA, Kufer P, Bargou R. BiTE: Teaching antibodies to engage T-cells for cancer therapy. Curr Opin Mol Ther. 2009;11(1):22-30.

50. Mortier E, Quemener A, Vusio P, Lorenzen I, Boublik Y, Grotzinger J, et al. Soluble interleukin-15 receptor alpha (IL-15R alpha)-sushi as a selective and potent agonist of IL-15 action through IL-15R beta/gamma. Hyperagonist IL-15 x IL-15R alpha fusion proteins. J Biol Chem. 2006;281(3):1612-9.

51. Waldmann TA. The biology of interleukin-2 and interleukin-15: implications for cancer therapy and vaccine design. Nat Rev Immunol. 2006;6(8):595-601.

52. Bergamaschi C, Rosati M, Jalah R, Valentin A, Kulkarni V, Alicea C, et al. Intracellular interaction of interleukin-15 with its receptor alpha during production leads to mutual stabilization and increased bioactivity. J Biol Chem. 2008;283(7):4189-99.

53. Mosquera LA, Card KF, Price-Schiavi SA, Belmont HJ, Liu B, Builes J, et al. In vitro and in vivo characterization of a novel antibody-like single-chain TCR human IgG1 fusion protein. J Immunol. 2005;174(7):4381-8.

54. Wen J, Zhu X, Liu B, You L, Kong L, Lee HI, et al. Targeting activity of a TCR/IL-2 fusion protein against established tumors. Cancer Immunol Immunother. 2008;57(12):1781-94.

55. Theobald M, Biggs J, Dittmer D, Levine AJ, Sherman LA. Targeting p53 as a general tumor antigen. Proceedings of the National Academy of Sciences of the United States of America. 1995;92(26):11993-7.

56. Zhu X, Marcus WD, Xu W, Lee HI, Han K, Egan JO, et al. Novel human interleukin-15 agonists. J Immunol. 2009;183(6):3598-607.

57. Deer JR, Allison DS. High-Level Expression of Proteins in Mammalian Cells Using Transcription Regulatory Sequences from the Chinese Hamster EF-1alpha Gene. Biotechnology Progress. 2004;20(3):880-9.

58. Zhao Y, Bennett AD, Zheng Z, Wang QJ, Robbins PF, Yu LYL, et al. High-Affinity TCRs Generated by Phage Display Provide CD4+ T Cells with the Ability to Recognize and Kill Tumor Cell Lines. J Immunol. 2007;179(9):5845-54.

59. Belmont HJ, Price-Schiavi S, Liu B, Card KF, Lee HI, Han KP, et al. Potent antitumor activity of a tumor-specific soluble TCR/IL-2 fusion protein. Clin Immunol. 2006;121(1):29-39.

60. Yang S, Rosenberg SA, Morgan RA. Clinical-scale lentiviral vector transduction of PBL for TCR gene therapy and potential for expression in less-differentiated cells. J Immunother. 2008;31(9):830-9.

61. Card KF, Price-Schiavi SA, Liu B, Thomson E, Nieves E, Belmont H, et al. A soluble single-chain T-cell receptor IL-2 fusion protein retains MHC-restricted peptide specificity and IL-2 bioactivity. Cancer Immunol Immunother. 2004;53(4):345-57.

62. Garboczi DN, Hung DT, Wiley DC. HLA-A2-peptide complexes: refolding and crystallization of molecules expressed in Escherichia coli and complexed with single antigenic peptides. PNAS. 1992;89(8):3429-33.

63. Wei X-q, Orchardson M, Gracie JA, Leung BP, Gao B-m, Guan H, et al. The Sushi Domain of Soluble IL-15 Receptor {{alpha}} Is Essential for Binding IL-15 and Inhibiting Inflammatory and Allogenic Responses In Vitro and In Vivo. J Immunol. 2001;167(1):277-82.

64. Zhu X, Belmont HJ, Price-Schiavi S, Liu B, Lee HI, Fernandez M, et al. Visualization of p53(264-272)/HLA-A*0201 complexes naturally presented on tumor cell surface by a multimeric soluble single-chain T cell receptor. J Immunol. 2006;176(5):3223-32.

65. Chirifu M, Hayashi C, Nakamura T, Toma S, Shuto T, Kai H, et al. Crystal structure of the IL-15-IL-15Ralpha complex, a cytokine-receptor unit presented in trans. Nat Immunol. 2007;8(9):1001-7.

66. Hogquist KA, Jameson SC, Heath WR, Howard JL, Bevan MJ, Carbone FR. T cell receptor antagonist peptides induce positive selection. Cell. 1994;76(1):17-27.

67. Schott E, Ploegh HL. Mouse MHC class I tetramers that are unable to bind to CD8 reveal the need for CD8 engagement in order to activate naive CD8 T cells. Eur J Immunol. 2002;32(12):3425-34.

68. Neveu B, Echasserieau K, Hill T, Kuus-Reichel K, Houssaint E, Bonneville M, et al. Impact of CD8-MHC class I interaction in detection and sorting efficiencies of antigen-specific T cells using MHC class I/peptide multimers: contribution of pMHC valency. Int Immunol. 2006;18(7):1139-45.

69. Kern P, Hussey RE, Spoerl R, Reinherz EL, Chang H-C. Expression, Purification, and Functional Analysis of Murine Ectodomain Fragments of CD8alpha/alpha and CD8alpha/beta Dimers. Journal of Biological Chemistry. 1999;274(38):27237-43.

70. Arcaro A, Gregoire C, Bakker TR, Baldi L, Jordan M, Goffin L, et al. CD8beta endows CD8 with efficient coreceptor function by coupling T cell receptor/CD3 to raft-associated CD8/p56(lck) complexes. J Exp Med. 2001;194(10):1485-95.

71. Garboczi DN, Ghosh P, Utz U, Fan QR, Biddison WE, Wiley DC. Structure of the complex between human T-cell receptor, viral peptide and HLA-A2. Nature. 1996;384(6605):134-41.

72. Lin A, Devaux B, Green A, Sagerstrom C, Elliott J, Davis M. Expression of T cell antigen receptor heterodimers in a lipid-linked form. Science. 1990;249(4969):677-9.

73. Traunecker A, Dolder B, Oliveri F, Karjalainen K. Solubilizing the T-cell receptor--problems in solution. Immunol Today. 1989;10(1):29-32.

74. Cheever MA. Twelve immunotherapy drugs that could cure cancers. Immunol Rev. 2008;222:357-68.

75. Kaspar M, Trachsel E, Neri D. The antibody-mediated targeted delivery of interleukin-15 and GM-CSF to the tumor neovasculature inhibits tumor growth and metastasis. Cancer Res. 2007;67(10):4940-8.

76. Ferrari-Lacraz S, Zanelli E, Neuberg M, Donskoy E, Kim YS, Zheng XX, et al. Targeting IL-15 Receptor-Bearing Cells with an Antagonist Mutant IL-15/Fc Protein Prevents Disease Development and Progression in Murine Collagen-Induced Arthritis. J Immunol. 2004;173(9):5818-26.

77. Zheng XX, Gao W, Donskoy E, Neuberg M, Ruediger M, Strom TB, et al., editors. An Antagonist Mutant IL-15/Fc Promotes Transplant Tolerance. Transplantation; 2006.

78. Laugel B, van den Berg HA, Gostick E, Cole DK, Wooldridge L, Boulter J, et al. Different T cell receptor affinity thresholds and CD8 coreceptor dependence govern cytotoxic T lymphocyte activation and tetramer binding properties. J Biol Chem. 2007;282(33):23799-810.

79. Gakamsky DM, Luescher IF, Pramanik A, Kopito RB, Lemonnier F, Vogel H, et al. CD8 kinetically promotes ligand binding to the T-cell antigen receptor. Biophys J. 2005;89(3):2121-33.

80. Cole DK, Dunn SM, Sami M, Boulter JM, Jakobsen BK, Sewell AK. T cell receptor engagement of peptide-major histocompatibility complex class I does not modify CD8 binding. Mol Immunol. 2008;45(9):2700-9.

81. Alam SM, Davies GM, Lin CM, Zal T, Nasholds W, Jameson SC, et al. Qualitative and quantitative differences in T cell receptor binding of agonist and antagonist ligands. Immunity. 1999;10(2):227-37.

82. Ward A, Anderson M, Craggs RI, Maltby J, Grahames C, Davies RA, et al. E. coli expression and purification of human and cynomolgus IL-15. Protein Expr Purif. 2009;68(1):42-8.

83. Stoklasek TA, Schluns KS, Lefrancois L. Combined IL-15/IL-15Ralpha immunotherapy maximizes IL-15 activity in vivo. J Immunol. 2006;177(9):6072-80.

84. Rubinstein MP, Kovar M, Purton JF, Cho JH, Boyman O, Surh CD, et al. Converting IL-15 to a superagonist by binding to soluble IL-15R{alpha}. Proceedings of the National Academy of Sciences of the United States of America. 2006;103(24):9166-71.

85. Epardaud M, Elpek KG, Rubinstein MP, Yonekura AR, Bellemare-Pelletier A, Bronson R, et al. Interleukin-15/interleukin-15R alpha complexes promote destruction of established tumors by reviving tumor-resident CD8+ T cells. Cancer Res. 2008;68(8):2972-83.

86. Dubois S, Patel HJ, Zhang M, Waldmann TA, Muller JR. Preassociation of IL-15 with IL-15R alpha-IgG1-Fc enhances its activity on proliferation of NK and CD8+/CD44high T cells and its antitumor action. J Immunol. 2008;180(4):2099-106.

87. TJ Chen TC, CY Chen, SCN Hsu, TL Cheng, GC Liu, and YM Wang. Targeted Herceptin–dextran iron oxide nanoparticles for noninvasive imaging of HER2/neu receptors using MRI. Journal of Biological Inorganic Chemistry. 2008;14(2):253-60.

88. T Cyrus PW, SD Caruthers, SA Wickline, GM Lanza, M Gregory. Magnetic resonance nanoparticles for cardiovascular molecular imaging and therapy. Expert Review of Cardiovascular Therapy. 2005;3(4):705-15.

89. D Josephs JS, M O'Doherty. Molecular imaging in clinical trials. Targeted Oncology. 2009:1776-2596.

90. T Kanderi WM, JA Wendt. Molecular imaging in transplantation: basic concepts and strategies for potential application. Nuclear Medicine Communications. 2005;26(11):947-55.

91. KB Hartman LW, MG Rosenblum. Detecting and Treating Cancer with Nanotechnology. Molecular Diagnosis & Therapy. 2008;12(1):1-14.

92. Yang L. Development of tumor-targeted nanoparticles for in vivo tumor imaging and drug delivery. Nanomedicine: Nanotechnology, Biology and Medicine. 2006;2(4):293.

93. HB Na JL, K An, YI Park, M Park, IS Lee, DH Nam, ST Kim, SH Kim, SW Kim, KH Lim, KS Kim, SO Kim, T Hyeon. Development of a T1 contrast agent for magnetic resonance imaging using MnO nanoparticles. Angew Chem Int Ed Engl. 2007;46(28):5397-401.

94. Vogelstein B, Lane D, Levine AJ. Surfing the p53 network. Nature. 2000;408(6810):307-10.

95. Olivier M, Eeles R, Hollstein M, Khan MA, Harris CC, Hainaut P. The IARC TP53 database: new online mutation analysis and recommendations to users. Hum Mutat. 2002;19(6):607-14.

96. McLaughlin R, O'Hanlon D, McHale T, Connolly CE, Given HF. Prognostic implications of p53 and bcl-2 expression in 108 women with stage two breast cancer. Ir J Med Sci. 2001;170(1):11-3.

97. Temmim L, Baker H, Sinowatz F. Immunohistochemical detection of p53 protein expression in breast cancer in young Kuwaiti women. Anticancer Res. 2001;21(1B):743-8.

98. Soussi T. p53 mutations and resistance to chemotherapy: A stab in the back for p73. Cancer Cell. 2003;3(4):303-5.

99. Matoba S, Kang JG, Patino WD, Wragg A, Boehm M, Gavrilova O, et al. p53 regulates mitochondrial respiration. Science. 2006;312(5780):1650-3.

100. Chen X, Wong R, Khalidov I, Wang AY, Leelawattanachai J, Wang Y, et al. Inflamed luekocyte-mimetic nanoparticles for molecule imaging of inflammation. Biomaterials. 2011;32(30):7651-61. PMCID: 3156267.

101. Nathan C, Ding A. Nonresolving inflammation. Cell. 2010;140(6):871-82.

102. Cohen J. The immunopathogenesis of sepsis. Nature. 2002;420(6917):885-91.

103. Glass CK, Saijo K, Winner B, Marchetto MC, Gage FH. Mechanisms underlying inflammation in neurodegeneration. Cell. 2010;140(6):918-34.

104. Libby P. Inflammation in atherosclerosis. Nature. 2002;420(6917):868-74.

105. Hotamisligil GS. Inflammation and metabolic disorders. Nature. 2006;444(7121):860-7.

106. Coussens LM, Werb Z. Inflammation and cancer. Nature. 2002;420(6917):860-7. PMCID: 2803035.

107. Mantovani A, Allavena P, Sica A, Balkwill F. Cancer-related inflammation. Nature. 2008;454(7203):436-44.

108. Sipkins DA, Gijbels K, Tropper FD, Bednarski M, Li KC, Steinman L. ICAM-1 expression in autoimmune encephalitis visualized using magnetic resonance imaging. Journal of neuroimmunology. 2000;104(1):1-9.

109. Weller GE, Lu E, Csikari MM, Klibanov AL, Fischer D, Wagner WR, et al. Ultrasound imaging of acute cardiac transplant rejection with microbubbles targeted to intercellular adhesion molecule-1. Circulation. 2003;108(2):218-24.

110. Zhang N, Chittasupho C, Duangrat C, Siahaan TJ, Berkland C. PLGA nanoparticle--peptide conjugate effectively targets intercellular cell-adhesion molecule-1. Bioconjugate chemistry. 2008;19(1):145-52.

111. Kelly KA, Allport JR, Tsourkas A, Shinde-Patil VR, Josephson L, Weissleder R. Detection of vascular adhesion molecule-1 expression using a novel multimodal nanoparticle. Circulation research. 2005;96(3):327-36.

112. Voinea M, Manduteanu I, Dragomir E, Capraru M, Simionescu M. Immunoliposomes directed toward VCAM-1 interact specifically with activated endothelial cells--a potential tool for specific drug delivery. Pharmaceutical research. 2005;22(11):1906-17.

113. Nahrendorf M, Keliher E, Panizzi P, Zhang H, Hembrador S, Figueiredo JL, et al. 18F-4V for PET-CT imaging of VCAM-1 expression in atherosclerosis. Jacc. 2009;2(10):1213-22.

114. Ehrhardt C, Kneuer C, Bakowsky U. Selectins-an emerging target for drug delivery. Advanced drug delivery reviews. 2004;56(4):527-49.

115. Chan JM, Zhang L, Tong R, Ghosh D, Gao W, Liao G, et al. Spatiotemporal controlled delivery of nanoparticles to injured vasculature. Proceedings of the National Academy of Sciences of the United States of America. 2010;107(5):2213-8. PMCID: 2836709.

116. Dustin ML, Rothlein R, Bhan AK, Dinarello CA, Springer TA. Induction by IL 1 and interferon-gamma: tissue distribution, biochemistry, and function of a natural adherence molecule (ICAM-1). J Immunol. 1986;137(1):245-54.

117. Kang S, Park T, Chen X, Dickens G, Lee B, Lu K, et al. Tunable physiologic interactions of adhesion molecules for inflamed cell-selective drug delivery. Biomaterials. 2011.

118. Jin M, Song G, Carman CV, Kim YS, Astrof NS, Shimaoka M, et al. Directed evolution to probe protein allostery and integrin I domains of 200,000-fold higher affinity. Proceedings of the National Academy of Sciences of the United States of America. 2006;103(15):5758-63. PMCID: 1458646.

119. Wharton S, Schafer A, Bowtell R. Susceptibility mapping in the human brain using threshold-based k-space division. Magn Reson Med. 2010;63(5):1292-304.

120. Weber C, Fraemohs L, Dejana E. The role of junctional adhesion molecules in vascular inflammation. Nat Rev Immunol. 2007;7(6):467-77.

121. Shimaoka M, Lu C, Palframan RT, von Andrian UH, McCormack A, Takagi J, et al. Reversibly locking a protein fold in an active conformation with a disulfide bond: integrin alphaL I domains with high affinity and antagonist activity in vivo. Proceedings of the National Academy of Sciences of the United States of America. 2001;98(11):6009-14.

122. Marlin SD, Springer TA. Purified intercellular adhesion molecule-1 (ICAM-1) is a ligand for lymphocyte function-associated antigen 1 (LFA-1). Cell. 1987;51(5):813-9.

123. Park S, Kang S, Veach AJ, Vedvyas Y, Zarnegar R, Kim JY, et al. Self-assembled nanoplatform for targeted delivery of chemotherapy agents via affinity-regulated molecular interactions. Biomaterials. 2010;31(30):7766-75. PMCID: 2925180.

124. Dubertret B, Skourides P, Norris DJ, Noireaux V, Brivanlou AH, Libchaber A. In vivo imaging of quantum dots encapsulated in phospholipid micelles. Science. 2002;298(5599):1759-62.

125. Kelly CP, O'Keane JC, Orellana J, Schroy PC, 3rd, Yang S, LaMont JT, et al. Human colon cancer cells express ICAM-1 in vivo and support LFA-1-dependent lymphocyte adhesion in vitro. Am J Physiol. 1992;263(6 Pt 1):G864-70.

126. Maurer CA, Friess H, Kretschmann B, Wildi S, Muller C, Graber H, et al. Over-expression of ICAM-1, VCAM-1 and ELAM-1 might influence tumor progression in colorectal cancer. International journal of cancer. 1998;79(1):76-81.

127. Hayes SH, Seigel GM. Immunoreactivity of ICAM-1 in human tumors, metastases and normal tissues. Int J Clin Exp Pathol. 2009;2(6):553-60. PMCID: 2713456.

128. Reinhardt M, Hauff P, Linker RA, Briel A, Gold R, Rieckmann P, et al. Ultrasound derived imaging and quantification of cell adhesion molecules in experimental autoimmune encephalomyelitis (EAE) by Sensitive Particle Acoustic Quantification (SPAQ). Neuroimage. 2005;27(2):267-78.

129. Osborn L. Leukocyte adhesion to endothelium in inflammation. Cell. 1990;62(1):3-6.

130. Springer TA. Adhesion receptors of the immune system. Nature. 1990;346(6283):425-34.

131. Shi W, Wang J, Fan X, Gao H. Size and shape effects on diffusion and absorption of colloidal particles near a partially absorbing sphere: implications for uptake of nanoparticles in animal cells. Physical review. 2008;78(6 Pt 1):061914.

132. Mailander V, Landfester K. Interaction of nanoparticles with cells. Biomacromolecules. 2009;10(9):2379-400.

133. Rajashekhar G, Willuweit A, Patterson CE, Sun P, Hilbig A, Breier G, et al. Continuous endothelial cell activation increases angiogenesis: evidence for the direct role of endothelium linking angiogenesis and inflammation. Journal of vascular research. 2006;43(2):193-204.

134. Franses JW, Baker AB, Chitalia VC, Edelman ER. Stromal endothelial cells directly influence cancer progression. Science translational medicine. 2011;3(66):66ra5.

135. Pandolfi F, Trentin L, Boyle LA, Stamenkovic I, Byers HR, Colvin RB, et al. Expression of cell adhesion molecules in human melanoma cell lines and their role in cytotoxicity mediated by tumor-infiltrating lymphocytes. Cancer. 1992;69(5):1165-73.

136. Kobayashi H, Boelte KC, Lin PC. Endothelial cell adhesion molecules and cancer progression. Current medicinal chemistry. 2007;14(4):377-86.

137. Nelson H, Ramsey PS, Donohue JH, Wold LE. Cell adhesion molecule expression within the microvasculature of human colorectal malignancies. Clinical immunology and immunopathology. 1994;72(1):129-36.

138. Fox SB, Turner GD, Leek RD, Whitehouse RM, Gatter KC, Harris AL. The prognostic value of quantitative angiogenesis in breast cancer and role of adhesion molecule expression in tumor endothelium. Breast cancer research and treatment. 1995;36(2):219-26.

139. Suzuki Y, Ohtani H, Mizoi T, Takeha S, Shiiba K, Matsuno S, et al. Cell adhesion molecule expression by vascular endothelial cells as an immune/inflammatory reaction in human colon carcinoma. Jpn J Cancer Res. 1995;86(6):585-93.

140. Cianchi F, Cuzzocrea S, Vinci MC, Messerini L, Comin CE, Navarra G, et al. Heterogeneous expression of cyclooxygenase-2 and inducible nitric oxide synthase within colorectal tumors: correlation with tumor angiogenesis. Dig Liver Dis. 2010;42(1):20-7.

141. Wong R, Chen X, Wang Y, Hu X, Jin MM. Visualizing and Quantifying Acute Inflammation Using ICAM-1 Specific Nanoparticles and MRI Quantitative Susceptibility Mapping. Ann Biomed Eng. 2011.

142. Nathan C. Points of control in inflammation. Nature. 2002;420(6917):846-52.

143. Corti R, Hutter R, Badimon JJ, Fuster V. Evolving concepts in the triad of atherosclerosis, inflammation and thrombosis. J Thromb Thrombolysis. 2004;17(1):35-44.

144. Wellen KE, Hotamisligil GS. Obesity-induced inflammatory changes in adipose tissue. The Journal of clinical investigation. 2003;112(12):1785-8. PMCID: 297006.

145. Aird WC. The role of the endothelium in severe sepsis and multiple organ dysfunction syndrome. Blood. 2003;101(10):3765-77.

146. Nathan C, Sporn M. Cytokines in context. J Cell Biol. 1991;113(5):981-6. PMCID: 2289009.

147. Buckley CD, Pilling D, Lord JM, Akbar AN, Scheel-Toellner D, Salmon M. Fibroblasts regulate the switch from acute resolving to chronic persistent inflammation. Trends Immunol. 2001;22(4):199-204.

148. Barnes PJ. Immunology of asthma and chronic obstructive pulmonary disease. Nat Rev Immunol. 2008;8(3):183-92.

149. Deitch EA. Multiple organ failure. Pathophysiology and potential future therapy. Ann Surg. 1992;216(2):117-34. PMCID: 1242583.

150. McAteer MA, Akhtar AM, von Zur Muhlen C, Choudhury RP. An approach to molecular imaging of atherosclerosis, thrombosis, and vascular inflammation using microparticles of iron oxide. Atherosclerosis. 2010;209(1):18-27. PMCID: 2839076.

151. Jaffer FA, Tung CH, Wykrzykowska JJ, Ho NH, Houng AK, Reed GL, et al. Molecular imaging of factor XIIIa activity in thrombosis using a novel, near-infrared fluorescent contrast agent that covalently links to thrombi. Circulation. 2004;110(2):170-6.

152. Wilson MS, Wynn TA. Pulmonary fibrosis: pathogenesis, etiology and regulation. Mucosal Immunol. 2009;2(2):103-21. PMCID: 2675823.

153. Lanza GM, Yu X, Winter PM, Abendschein DR, Karukstis KK, Scott MJ, et al. Targeted antiproliferative drug delivery to vascular smooth muscle cells with a magnetic resonance imaging nanoparticle contrast agent: implications for rational therapy of restenosis. Circulation. 2002;106(22):2842-7.

154. Massey JM, Amps J, Viapiano MS, Matthews RT, Wagoner MR, Whitaker CM, et al. Increased chondroitin sulfate proteoglycan expression in denervated brainstem targets following spinal cord injury creates a barrier to axonal regeneration overcome by chondroitinase ABC and neurotrophin-3. Exp Neurol. 2008;209(2):426-45. PMCID: 2270474.

155. Nahrendorf M, Jaffer FA, Kelly KA, Sosnovik DE, Aikawa E, Libby P, et al. Noninvasive vascular cell adhesion molecule-1 imaging identifies inflammatory activation of cells in atherosclerosis. Circulation. 2006;114(14):1504-11.

156. Kang S, Park T, Chen X, Dickens G, Lee B, Lu K, et al. Tunable physiologic interactions of adhesion molecules for inflamed cell-selective drug delivery. Biomaterials. 2011;32(13):3487-98.

157. Muro S, Gajewski C, Koval M, Muzykantov VR. ICAM-1 recycling in endothelial cells: a novel pathway for sustained intracellular delivery and prolonged effects of drugs. Blood. 2005;105(2):650-8.

158. Almenar-Queralt A, Duperray A, Miles LA, Felez J, Altieri DC. Apical topography and modulation of ICAM-1 expression on activated endothelium. Am J Pathol. 1995;147(5):1278-88. PMCID: 1869507.

159. Essani NA, Fisher MA, Farhood A, Manning AM, Smith CW, Jaeschke H. Cytokine-induced upregulation of hepatic intercellular adhesion molecule-1 messenger RNA expression and its role in the pathophysiology of murine endotoxin shock and acute liver failure. Hepatology. 1995;21(6):1632-9.

160. Farhood A, McGuire GM, Manning AM, Miyasaka M, Smith CW, Jaeschke H. Intercellular adhesion molecule 1 (ICAM-1) expression and its role in neutrophil-induced ischemia-reperfusion injury in rat liver. Journal of leukocyte biology. 1995;57(3):368-74.

161. Olanders K, Sun Z, Borjesson A, Dib M, Andersson E, Lasson A, et al. The effect of intestinal ischemia and reperfusion injury on ICAM-1 expression, endothelial barrier function, neutrophil tissue influx, and protease inhibitor levels in rats. Shock. 2002;18(1):86-92.

162. Volpes R, van den Oord JJ, Desmet VJ. Immunohistochemical study of adhesion molecules in liver inflammation. Hepatology. 1990;12(1):59-65.

163. Werner J, Z'Graggen K, Fernandez-del Castillo C, Lewandrowski KB, Compton CC, Warshaw AL. Specific therapy for local and systemic complications of acute pancreatitis with monoclonal antibodies against ICAM-1. Ann Surg. 1999;229(6):834-40; discussion 41-2. PMCID: 1420830.

164. Denis MC, Mahmood U, Benoist C, Mathis D, Weissleder R. Imaging inflammation of the pancreatic islets in type 1 diabetes. Proceedings of the National Academy of Sciences of the United States of America. 2004;101(34):12634-9. PMCID: 515109.

165. Eniola AO, Willcox PJ, Hammer DA. Interplay between rolling and firm adhesion elucidated with a cell-free system engineered with two distinct receptor-ligand pairs. Biophys J. 2003;85(4):2720-31. PMCID: 1303496.

166. Haun JB, Hammer DA. Quantifying nanoparticle adhesion mediated by specific molecular interactions. Langmuir. 2008;24(16):8821-32.

167. Eniola AO, Hammer DA. Characterization of biodegradable drug delivery vehicles with the adhesive properties of leukocytes II: effect of degradation on targeting activity. Biomaterials. 2005;26(6):661-70.

168. Omolola Eniola A, Hammer DA. In vitro characterization of leukocyte mimetic for targeting therapeutics to the endothelium using two receptors. Biomaterials. 2005;26(34):7136-44.

169. Swirski FK, Nahrendorf M, Etzrodt M, Wildgruber M, Cortez-Retamozo V, Panizzi P, et al. Identification of splenic reservoir monocytes and their deployment to inflammatory sites. Science. 2009;325(5940):612-6. PMCID: 2803111.

170. Billiar TR, West MA, Hyland BJ, Simmons RL. Splenectomy alters Kupffer cell response to endotoxin. Arch Surg. 1988;123(3):327-32.

171. Nogueira N, Cohn ZA. Trypanosoma cruzi: in vitro induction of macrophage microbicidal activity. J Exp Med. 1978;148(1):288-300. PMCID: 2184909.

172. Van Snick J. Interleukin-6: an overview. Annu Rev Immunol. 1990;8:253-78.

173. Panes J, Perry MA, Anderson DC, Manning A, Leone B, Cepinskas G, et al. Regional differences in constitutive and induced ICAM-1 expression in vivo. Am J Physiol. 1995;269(6 Pt 2):H1955-64.

174. Burns AR, Takei F, Doerschuk CM. Quantitation of ICAM-1 expression in mouse lung during pneumonia. J Immunol. 1994;153(7):3189-98.

175. Liu T, Spincemaille P, de Rochefort L, Wong R, Prince M, Wang Y. Unambiguous identification of superparamagnetic iron oxide particles through quantitative susceptibility mapping of the nonlinear response to magnetic fields. Magn Reson Imaging. 2010;28(9):1383-9. PMCID: 2963706.

176. Hu X, Kang S, Chen X, Shoemaker CB, Jin MM. Yeast surface two-hybrid for quantitative in vivo detection of protein-protein interactions via the secretory pathway. J Biol Chem. 2009;284(24):16369-76. PMCID: 2713516.

177. Regents NYSBo. Public School Total Cohort Graduation Rate and Enrollment Outcome Summary - 2009-10 School Year All Students [Press Release]2011: Available from: http://www.p12.nysed.gov/irs/press.html.

178. Regents NYSBo. Education Department Releases High School Graduation Rates [Press Release]2011: Available from: http://www.p12.nysed.gov/irs/press.html.

179. Keys CW, Bryan LA. Co-constructing inquiry-based science with teachers: Essential research for lasting reform. J Res Sci Teach. 2001;38(6):631-45.

180. Department NYSE. Past Examinations2011: Available from: http://www.nysedregents.org/.

181. Grant SG. An uncertain lever: Exploring the influence of state-level testing in New York State on teaching social studies. Teach Coll Rec. 2001;103(3):398-426.

182. Regents NYSBo. New York State Regents Exams2011: Available from: http://www.nysl.nysed.gov/regentsexams.htm.

183. Schoenfeld AH. When Good Teaching Leads to Bad Results - the Disasters of Well-Taught Mathematics Courses. Educ Psychol. 1988;23(2):145-66.

184. Compston A, Coles A. Multiple sclerosis. Lancet. 2002;359(9313):1221-31.

185. McDonald WI, Compston A, Edan G, Goodkin D, Hartung HP, Lublin FD, et al. Recommended diagnostic criteria for multiple sclerosis: guidelines from the International Panel on the diagnosis of multiple sclerosis. Ann Neurol. 2001;50(1):121-7.

186. Guttmann CRG, Meier DS, Holland CM. Can MRI reveal phenotypes of multiple sclerosis? Magnetic Resonance Imaging. 2006;24(4):475-81.

187. Cannella B, Raine CS. The adhesion molecule and cytokine profile of multiple sclerosis lesions. Ann Neurol. 1995;37(4):424-35.